SUPERHYDROPHILIC AND SUPEROLEOPHOBIC MESHES FOR ON-SITE OIL-WATER SEPARATION

By

© Elaheh Vaziri

A thesis submitted to the School of Graduate Studies in partial fulfillment of the requirements for the degree of

MASTER OF ENGINEERING

Faculty of Engineering and Applied Science
Memorial University of Newfoundland

February 2023

St. John's, Newfoundland and Labrador, Canada

*"Dedicated to my best friend, **Hanif**, my parents and my brother"*

ABSTRACT

Oil spills are becoming a major cause of environmental damage on a worldwide scale. Effective ways to separate oil from water are needed to solve this issue. Meshes and membranes that are superhydrophilic/superoleophobic are promising materials for oil-water separation, but their actual utilisation still confronts several obstacles. In this work, we made oleophobic TiO_2 and SiO_2 nanoparticle-coated superhydrophilic stainless steel meshes. The coating was made by electrophoretically depositing positively charged nanoparticles of TiO_2 and SiO_2 on stainless steel meshes after treating of TiO_2 and SiO_2 with iodine in acetyl acetone solutions. To increase stability and oil-water separation performance, four different mesh counts (80, 120, 200, and 400) were created and put through sintering operations at various temperatures. X-ray diffraction (XRD), scanning electron microscopy (SEM), and contact angle (CA) measurements were used to explore the specific microscopic structural characteristics of these meshes. These meshes were evaluated for their ability to separate oil from water using gas florescence and ultraviolet-visible (UV-vis) spectroscopic methods. Our research has shown that the mesh created with 1% concentration of SiO_2 (SiO_2/TiO_2 = 0.01), mesh spacing 400, and sintering temperature 800 °C had the optimal oil-water separation performance. It is important to note that for hexane and Terra-Nova oil, this mesh exhibits outstanding surface hydrophilicity/oleophobicity with static contact angles greater than 170°. In this experiment Terranova oil used in prepared emulsion for oil-water separation tests and the efficiency calculated was 91%. Also, these coated meshes can be reused for at least five cycles, according to durability testing, which also minimises the cost of treating oily wastewater.

ACKNOWLEDGEMENTS

I would like to express my sincere gratitude to my late supervisor, Dr. Tahir Husain for his invaluable advice and continuous support and patience during my research.

I also want to convey my appreciation to my supervisor, Dr. Xili Duan, for his helpful guidance and encouragement throughout the entire research project.

Many thanks to my colleagues and friends for their wonderful collaboration, feedback, and bright ideas. Without your help, I could not have achieved such a remarkable result.

This project would not have been possible without the financial support from Fisheries and Ocean Canada (DFO) and Memorial University of Newfoundland (MUN).

TABLE OF CONTENTS:

LIST OF FIGURES

LIST OF TABLES

LIST OF ABBREVIATIONS

AFM	Atomic Force Microscopy
ATR-FTIR	Attenuated Total Reflection- Fourier Transform Infrared Spectroscopy
BE	Binding Energy
BSE	Back Scattered electrons
CA	Contact Angle
CB	Cassie and Baxter
CFD	Computational Flow Dynamics
CVD	Chemical vapor deposition
DCM	Dichloromethane
DI	Deionized Water
DRIFT	Diffuse Reflection Infrared Fourier Transform
DSC	Differential scanning calorimetry
EDX	Energy Dispersive X-ray
EPD	Electrophoretic Deposition
FTIR	Fourier Transform Infrared Spectroscopy
GC-MS	Gas Chromatography Mass Spectrometry
HR TEM	High-Resolution
IR	Infrared
LDR	Linear Dynamic Rang
MW	Molecular Weight
OCA	Molecular Weight
OD	Oil Dispersed
OC	Oil Concentration
OWRK	Neumann and Owen, Wendt, Rabel and Kaelble models
PDA	Polydopamine
PES	Polyethersulfone
PIT	Photon Technology International
PVDF	Polyvinylidene Difluoride
SEM	Scanning Electron Microscopy
SiO_2	Silica
SNP	Silver Nanoparticles
SS	Stainless Steel
TEM	Transmission Electron Microscopy

TiO_2	Titanium Oxide
UHV	Ultra-High Vacuum
UV	Ultraviolet
UV-Vis	Ultraviolet-Visible Spectroscopic
WCA	Water Contact Angle
XPS	X-ray Photoelectron Spectroscopy
XRD	X-ray Diffraction
YAG	Yttrium Aluminum Garnet
YCA	Young Contact Angle

NOMENCLATURE

Δt	time	s
ΔV	volume of filtrate collected in the beaker	L
Abs	uv wavelengths absorbances	nm
d_{hlk}	diffraction	-
F	permeating flow	$L/s.m^2$
f_l	fraction of wet solid surface	-
g	gravitational acceleration constant	m/s^2
h_{oil}	the maximum height of oil	m
n	Integer number	-
OD	oil dispersed	g
OC	oil concentration	ppm
P	pressure	$kg/m.s^2$
r	surface roughness	-
r_f	roughness ratio of the wet area	-
V_{DCM}	volume of DCM extract	L
V_{ew}	total volume of seawater extracted	L
V_{oil}	volume	L
V_{tw}	total volume of seawater in the flask	L
γ^D	dispersive components of surface tensions	-
γ_{lv}	interfacial tensions of liquid–fluid	-
γ^P	polar components of surface tensions	-
γ_{sl}	interfacial tensions of solid-liquid	-
γ_{sv}	interfacial tensions of solid-fluid	-
θ_{App}	apparent contact angle	°
θ_{CB}	Cassie and Baxter contact angle	°
θ_i	x-ray incident angle	°
θ_Y	Young contact angle	°
ρ	density	kg/m^3
ρ_{oil}	density of the specific test oil	g/L

CHAPTER ONE

1 Introduction and Overview

1.1 Background

Oil spill has tremendous negative impacts on the ecological system and environment that can last for a long time. Frequent oil spill incidents are a big problem because they can cause significant energy loss in addition to serious environmental damage. Additionally, since even a little amount of water in fuel oil could jeopardise transportation safety, the expulsion of water from fuel oil is essential in the vehicle, ship, and aviation industries. In response to these enormous obstacles, scientists have consistently focused their efforts on creating new methods and materials for oil/water separation. Traditional techniques like centrifugation, air flotation, ultrasonic separation, electric fields, coagulation, and biological treatment are all widely used as separation technologies and can handle the majority of separation needs by thoroughly integrating physical, chemical, and biological approaches [1].

It is helpful to clarify what we are going to separate before we talk about separation technique and apparatus. It consists primarily of an oily phase and water. Free water and emulsified water are the two different types of water. When spilt at sea, the majority of crude oils and intermediate to heavy products will emulsify, generating water-in-oil-emulsions (w/o), sometimes known as "chocolate mousse." The natural emulsifiers found in the oil, colloidal particles in the sea, or oil biodegradation by-products can all be used to stabilise the w/o emulsions. The weathering process is extremely difficult and poorly understood. In the open water, agitation from turbulent surface conditions is what causes the initial intrusion of surface

oil into the water column. The majority of the energy needed for the operation is mostly contributed by breaking waves. The passage of small craft through surface oil and ship traffic are two other minor contributory variables.

Oil/water separation technologies play an essential role in treating oil spill field[2,3]. The development of novel functional materials with selective wetting behavior toward oil and water is a promising way for oil/water separation[4–6]. In this field, studies mainly focus on surface superwettabilities, such as superhydrophobicity, superhydrophilicity, superoleophobicity, and superoleophilicity [7].

Superhydrophobic and superoleophilic materials (with a water contact angle >150° and an oil contact angle <10°), can absorb or filtrate oil[5,8,9]. These oil-loving materials are subject to some major disadvantages; for example, they are not suitable for gravity-driven separation. They are easily foul or even blocked up by oil and affect the oil-water separation. Also, these types of materials are hard to clean and recycle [4,10–13]. On the other side, superhydrophilic and underwater superoleophobic materials (with an oil contact angle >150° and a water contact angle <10°), effectively prevent oil fouling and cause constant water permeation [5,7]. In addition, these materials are highly reported for their excellent separation efficiency, high filtration flux, and easy recycling for oil/water separation [7,11,14].

There are some attempts to fabricate materials having superoleophobic and superhydrophilic characteristics. Due to perceived dominance in anti-oil contamination, the potential application of superoleophobic/superhydrophilic materials in treating liquid mixtures has not been well-proven. Immiscible mixes and emulsions, for example, are two forms of oil-water mixtures based on the mix type. In immiscible mixes, oil and water are stratified by

densities. In contrast, emulsions are a more sophisticated mix type in which microdroplets of oil or water (diameter <20 um) are spread in the other [5]. The majority of available superoleophobic/superhydrophilic materials have been dedicated to achieving immiscible oil-water separation, and their use in emulsion separation has been proved very occasionally. Furthermore, the most prevalent forms of emulsions are oil-in-water and water-in-oil emulsions. Superhydrophilic materials, which have been produced in continued research, have shown to be a viable option for separating any type of emulsion. However, there is no evidence that superoleophobic/superhydrophilic material can be used to separate both forms of emulsions [15].

So far, various materials have been explored for underwater superoleophobicity, including TiO_2 [5], palygorskite [16], $Cu(OH)_2$ [17], ZnO [18,19], Silica [20] and hydrogels [21,22]. However, a high separation efficiency technology for separating oil from oily saltwater or wastewater has yet to be discovered. To promote practical applications, separation efficiency and stability in the complicated oily seawater or wastewater environment should be assessed [12,23,24].

Titanium oxide TiO_2, because of a large amount of hydroxyl groups on its surface, is often hydrophilic. Its photoinduced self-cleaning capability is widely used in oil/water separation studies [4,11,25]. Titanium dioxide (TiO_2) nanomaterials naturally appear in several phases; thermodynamically stable rutile and metastable highly crystallized anatase are two familiar sources of TiO_2. The hydrophilicity of TiO_2 closely depends on the formation of these two phases [11,26]. Also, Silica (SiO_2) has a hydrophilic feature and, due to its low price, is another material that gets attention for prevalent industrial submissions use [24].

Among diverse surface modification technologies, superhydrophilic/superoleophobic meshes and membranes due to superwettability feature, higher permeability, mechanical

strength, simplicity, and low cost, are promising for oil-water separation; but their practical application still faces many challenges [10,27,28]. Therefore, this thesis is aimed to fabricate superhydrophilic (θ_{water} <5°) stainless steel meshes that exhibit underwater superoleophobicity (θ_{oil}>170°) which will be coated with oleophobic TiO_2 and SiO_2 nanoparticles.

1.2 Research Objectives

It is helpful to clarify what we are going to separate before we talk about separation technique and apparatus. It consists primarily of an oily phase and water. Free water and emulsified water are the two different types of water. When spilt at sea, the majority of crude oils and intermediate to heavy products will emulsify, generating water-in-oil-emulsions (w/o), sometimes known as "chocolate mousse." The natural emulsifiers found in the oil, colloidal particles in the sea, or oil biodegradation byproducts can all be used to stabilise the w/o emulsions. The weathering process is extremely difficult and poorly understood.

Fabrication of surfaces with superhydrophilic and underwater superoleophobicity properties has attracted extensive attention as a solution to oil spills to the increase in industrial oily wastewater volume and frequency of accidental oil spills. Before being released into the water sources, the associated oil-water systems should be treated appropriately. To date, several techniques have been used to separate oil from water mixtures, including gravity separation, centrifugation, air flotation, electric field, coagulation, and adsorption [29,30]. Since these systems have traditionally been challenging to employ due to their low separation efficiency, secondary pollution production, and big size, more effective techniques were created. In order to achieve deep water purification, membrane filtration technology has advanced recently. Size exclusion and reverse osmosis techniques have been used to separate stable emulsions, dissolved oil, and

even chemical molecules. However, their range of applications is constrained by the stringent criteria for oil/water mixes, issues with membrane fouling, and high cost. Additionally, porous polymers and inorganic materials are frequently employed to absorb oils from water in order to meet the emergency response needs of oil spills. A well-known separation technique, has been widely used for oil-water separation applications because of its durability, economic and ease of use features [29,30].

This thesis presents a detailed study into the development and experimental characterization of surfaces with superhydrophilic and underwater superoleophobicity properties. This research investigates the electrodeposition of TiO_2 and SiO_2 nanoparticles onto stainless steel meshes (80, 120, 200, and 400 pore size) to produce superhydrophilic (water<0^o) surfaces with underwater superoleophobicity (oil>170^o). The TiO_2-coated mesh in its natural state has high water affinity and oil repellency underwater. Oils (n-hexane and ethanol) were separated from oily water using a superhydrophilic/ superoleophobic TiO_2/SiO_2-coated mesh.

Previous studies have assessed the superhydrophilic and superoleophobic mesh and membrane performance for use in oil-water separation applications. However, more experimental work is still needed in this area to lower fabrication costs, increase the stability under various harsh conditions, adapt to more industrial applications, and learn more about the mechanism of oil-water separation. We investigate a unique and affordable technology for fabricating stainless steel mesh for an efficient and dynamic oil-water separation to close the present knowledge gap in this field.

1.3 Organization of the Thesis

In chapter 2, a summary of the fundamental understanding of hydrophobic surfaces, wetting properties, and corrosion behavior is provided. Second, a review is conducted on related research in the fabrication of superhydrophilic stainless steel surfaces through different surface treatment methods. Then we discuss the methods to characterize the superhydrophilic and superoleophobic surfaces.

Chapter 3 introduces the experimental approaches and characterization methods. The general processes for achieving various levels of surface roughness and electrodeposition are detailed. Also, we discuss materials and techniques for fabricating and characterizing the superhydrophilic and superoleophobic SS mesh.

In Chapter 4, the results and discussions are provided; success in each fabrication step was ascertained by underwater oil contact angle measurements, surface energy, scanning electron microscopy (SEM), X-ray diffraction (XRD) and separation efficiency analyses are presented.

In Chapter 5, an overall conclusion of the whole research effort is provided, and some future work is suggested.

CHAPTER TWO

2 Literature Review

2.1 Surface Wettability and Contact Angle

Wetting phenomena can be observed every day around us. Examples are raindrops on a window or the spreading of ink on paper. In many industrial processes, such as oil recovery, lubrication, liquid coating, printing, and spray quenching, wetting plays a critical role, defined as the tendency of one fluid to spread on or adhere to a solid surface [31–33]. Wetting usually involves the measurement of contact angles and in general, includes all phenomena involving contacts between three phases, of which at least two are fluid (liquid or gaseous), and it indicates the degree of wetting when a solid and liquid interact [31]. As shown in Figure 1, Small contact angles (<90°) correspond to high wettability and the fluid will spread over a large area on the surface; while large contact angles (>90°) refer to low wettability and generally means that wetting of the surface is unfavorable so the fluid will minimize its contact with the surface and form a compact liquid droplet [34].

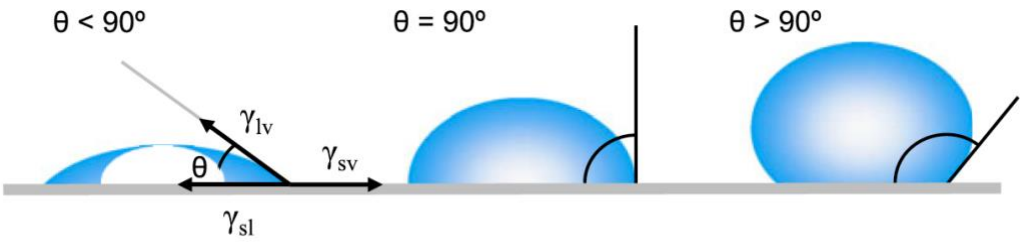

***Figure 1**: Illustration of contact angles formed by sessile drops on a smooth homogeneous solid surface [24].*

When a liquid droplet is placed onto an ideal solid surface, which is defined as smooth, rigid, chemically homogeneous, insoluble, and nonreactive, the droplet's shape in equilibrium is determined by the surface tensions of each phase. Young's equation quantifies the pioneering correlation between the contact angle and the interfacial tensions:

$$\cos\theta_Y = \frac{\gamma_{sv}-\gamma_{sl}}{\gamma_{lv}} \quad (1)$$

where the subscript Y indicates the Young contact angle (YCA), and three interfacial tensions characterize the three-phase wetting system: liquid–fluid, γ_{lv}, solid-liquid, γ_{sl}, and solid-fluid, γ_{sv} [35].

Wenzel accounted for the effect of surface roughness on contact angle. In the Wenzel model, the solid surface is chemically homogeneous, and the liquid completely penetrates the grooves of a rough surface [36].

$$cos\theta_{App} = rcos\theta_Y \quad (2)$$

In (2, θ_{App} represents the apparent contact angle, and r denotes the surface roughness parameter (r = 1 for a smooth surface and >1 for a rough one).

Under some roughness conditions, especially when roughness is high, air bubbles may be trapped in the roughness grooves underneath the liquid; in this case, the Wenzel equation is not a suitable case [35]. The solid surface may be considered chemically heterogeneous, and the Cassie and Baxter (CB) (3, can be applied in the following form:

$$\cos\theta_{CB} = fr_f\cos\theta_Y - (1-f) \quad (3)$$

where θ_{CB} is the CB apparent contact angle and f_1 is the fraction of the projected area of the solid surface wet by the liquid, and r_f is the roughness ratio of the wet spot. When f =1, r_f = r, the CB equation turns into the Wenzel equation [35]. Figure 2 shows the three contact angle stages based on the Young's, Wenzel, and Cassie-Baxter states.

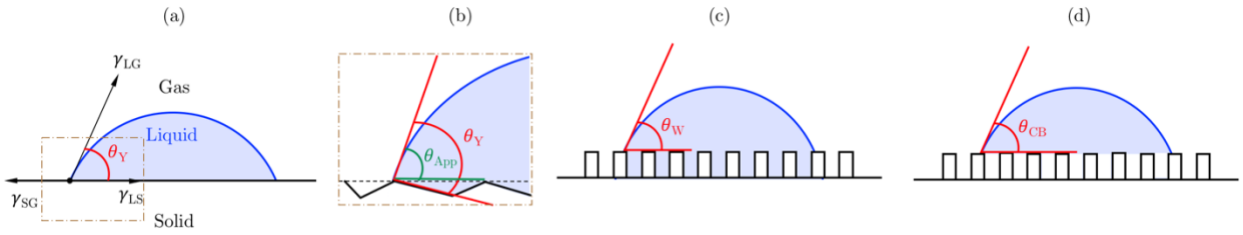

***Figure 2**: Three different contact conditions between surface and liquids based on (a) Young's state, (b) Wenzel state, and (c) Cassie-Baxter state [36].*

2.2 Surface Treatments

Solid materials are classified into two categories based on their interaction behavior with water; Depending on the water droplet contact angle, the material is classified as either: hydrophilic with an affinity for water absorption ($\theta_e < 90°$), hydrophobic with little or no tendency to absorb water ($90° < \theta_e < 150°$) [11,37,38].

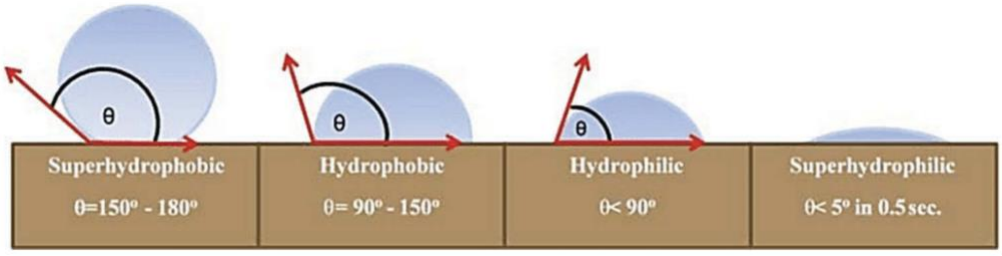

***Figure 3**: Schematic of water droplet's contact angle with different surface wettability [36].*

If the contact angle between the water droplet and the solid surface reaches less than 5° in less than 0.5 seconds ($\theta e < 5°$), the surface is superhydrophilic and for a contact angle higher than 150° ($\theta e > 150°$) the surface is superhydrophobic [28] (Figure 3).

We can find examples in nature. Plant leaves found in living nature are either water repellant or have an affinity to water. The lotus leaf is known to be super water repellent and is a model surface for superhydrophobicity. Water droplets falling on the leaf exhibit high contact angles and a low contact angle hysteresis or tilt angle due to forming air pockets (referred to as the Cassie-Baxter state of wetting). Therefore, droplets roll off the surface, moving quickly across the leaf, collecting debris as they go and keeping the leaf clean for photosynthesis [34].

Oil and water are not soluble or miscible in water contaminated with oil. Oil-water mixtures present can be divided into immiscible mixtures and emulsions. Oleophilic and superoleophilic states are used for a solid surface wetted by the oil (organic) phase; oleophobic and superoleophobic terms are used for solid surfaces not wetted by oil [39–41].

2.3 Characteristics of Superhydrophilic and Superoleophobic Materials

The wettability of the surface is controlled at the molecular level by the functional groups. For instance, the molecules -OH, -COO, -COOH, -NH2, -NH3+, -OSO3 and -OSO3H can form hydrogen bonds with water molecules and have hydrophilic properties, whereas silicone, fluorocarbon, and hydrocarbon-based polymers have lower surface energies and are more hydrophobic. Polar molecules will be able to dissolve in other polar liquids, such as water. This also applies to liquids spreading on surfaces with an electric dipole or multipole moment. This is a qualitative method to define a hydrophilic surface or ‘‘polar spreads on polar’’.

However, for metal surfaces, the hydrophilicity of the surface is a result of the dispersion forces, and these are adequate to induce water spreading on clean surfaces of noble metals [37].

In the solid–water–air system, the contact angle of a water droplet on a hydrophilic surface is less than 90°. Contact angles less than 5° make the surface superhydrophilic [36,42,43]. The difference between the advancing and retreating contact angles is called contact angle hysteresis. Its value is determined by whether the measurements are made in static or dynamic environments. Contact angle hysteresis is also affected by the rate of liquid flow [34].

In the process of oil-water separation, the superhydrophilic and superoleophobic surfaces have extremely high surface energy. So, the polar molecules of water spread rapidly on the surface. It happens because of the high surface tension of water compared to oil, which results in higher surface energy on the superhydrophilic surfaces than the hydrophobic surfaces. The superhydrophilic oil-water separation material can prevent the material from being contaminated by oil effectively to realize oil-water separation and material recycling. Under gravity, these materials can realize the selective separation of water in an oil-water mixture. This type of surface can be obtained by designing hydrophilic chemical composition and microscale or nanoscale layered structure [44]. This asset of the superhydophilic and superoleophobic materials makes it possible to create surfaces that repel oil while it tends to absorb water. So, water will pass through the porous structure of a coated surface, while oil will concentrate on the top surface, facilitating oil-water separation. [34].

Because of these qualities, superhydrophilic and underwater superoleophobic materials can be employed for oil-water separation. However, synthesis of this unique surface is very difficult. The surface tension of the liquid typically determines wettability for a specific surface.

Hexadecane, for example, has lower surface energy than water. As a result, hexadecane will always have a smaller contact angle than water for similar homogeneous substrates [45]. The hydrophilic and oleophobic components' positions are intercalated with one another. The interface is filled by the low-surface-energy component in the presence of oil droplets, resulting in oleophobicity. Water molecules are able to enter these surfaces when water droplets are present due to the presence of hydrophilic moieties and water-driven molecular rearrangement showing hydrophilicity [44–47].

The hydrophilic surface must be kept free of pollutants such as airborne organics, moisture, and dust particles to maintain the wetting properties. When exposed to the laboratory environment, a freshly produced hydrophilic surface tends to acquire its lowest energy (most stable state) by rapid changes at the surface, such as the adsorption of water molecules or organic pollutants. In this case, many materials naturally experience contamination of their hydrophilic surfaces and, resulting in a decrease in surface energy [48].

2.4 Fabrication of Superhydrophilic and Superoleophobic Surfaces

Surfaces can be modified to be more hydrophilic in one of two directions: by depositing a molecular layer of a new material that is more hydrophilic than the substrate or by changing the surface chemistry of the substrate. The most typical way for inorganic substrates is to apply coatings on the surface. In the case of polymeric materials, however, alteration of surface chemistry is involved. In this part, we'll go over some of the most prevalent ways for making surfaces hydrophilic [37,49].

2.4.1 Deposited Molecular Structures

Organic molecules that adsorb onto the solid surface can form monolayers. These molecules can come from either a solution or a vapor phase. The end of the deposited organic layers must be polar to produce a hydrophilic surface. Water will not be drawn to the surface if a saturated hydrocarbon-based group or a fluorinated group is near the end of the layer, resulting in hydrophobic circumstances. If the surface has chemical groups such as –OH, COOH, or POOH, water molecules will be attracted to it by hydrogen bonding [49]. Dip-coating and Spray methods are two common methods in this category [44].

Dip Coating: The dip-coating process is quick to prepare, simple to use, and ubiquitous. The metal mesh components are submerged in the prepared solution during the dip-coating procedure. The solution's components are then loosely and irregularly disseminated across the substrate surface, resulting in rough surface morphology and no interaction between the solvent and the substrate mesh throughout the coating process[44]. By depositing a plant tannin coating over the membrane surface, a hydrophilization modified PVDF membrane was created by Zhang et al. in 2016. The quantity of tannin coating that impacts the hydrophilicity and filtering performance is investigated by adjusting the modifying time. Zhang's team reported that all the modified membranes have a flux recovery ratio greater than 95%. Also, during the extended rinse procedure, the underwater oil contact angle reportedly stabilized at roughly 156° [50].

Spray method: Spraying functional materials directly on the surface of a material to provide a unique wettability surface is known as the spray technique. Nanoparticles made from low-surface-energy materials are manufactured, sprayed on the material's surface, and dried. After multiple rounds of spraying and drying, a surface with exceptional wettability was

achieved. The spraying approach is simple to use, uses little energy, and works well with metal matrix materials that are chemically stable [44].

Li et al. (2016) team designed an underwater superoleophobic TiO_2 coated mesh by spraying TiO_2 nanoparticles and polyurethane mixtures onto a stainless steel mesh, the separation efficiency of the coated mesh is as high as 99.0%, and the CA higher than 150° has reported [51].

The naturally and hydrothermally treated mica particles are used to create a unique superhydrophilic (underwater superoleophobic) filter by Gunatilake and Bandara (2017). Hydrothermally treated mica particles were first electrodeposited on a stainless steel mesh. Then natural mica particles were sprayed on top of the first hydrothermally deposited mica layer to create a double-layered filter. In air and underwater, the double-layered mica-coated membrane exhibited superamphiphilic and superhydrophilic/superoleophobic (contact angle >159) properties. With an oil/water separation effectiveness of over 99%, the membrane can separate a wide spectrum of oil-water combinations [9].

2.4.2 Modification of Surface Chemistry

Many advancements have been made in the recent few decades in producing surface treatments, such as using plasma, corona, flame, photons, electrons, ions, X-rays, g-rays, and ozone, to modify the chemistry of polymer surfaces without changing their bulk characteristics.

In-situ growth method: Recent research has focused on employing in-situ synthesis to produce composite materials. The changed material reacts with the substrate material in the in-situ chemical reaction, generating a unique structure on the substrate surface. This approach, which is simple and does not require a sophisticated retreatment process, dramatically enhances

the adhesion between the changed material and the substrate . Zhu et al., in their paper, reported that the in-situ synthesis of SNPs (Silver nanoparticles) in generating PES (polyethersulfone) casting solution was a unique way of constructing composite membranes. The surface hydrophilicity and charge density of composite membranes containing hydrophilic SNPs were significantly increased, aiding the antifouling characteristic of hybrid membranes. At 0.6 MPa, the water flux of composite membranes has reached 75.37 $L.m^{-2}.S^{-1}$ [52].

Electrochemical method: In the electrochemical method, the electrode of the substrate material undergoes an oxidation process under the influence of an external electric field, resulting in a dense rough structure on the surface [44]. Yuan et al. in 2017 used nanostructured TiO_2/CuO dual coatings to fabricate the copper mesh by a combination of electrochemical anodization and layer-by-layer self-assembly deposition and reached a contact angle of 154° for crude oil [25]. In a paper published by You et al. (2018), an alternate method for fabricating a unique all-inorganic membrane with superhydrophilicity and underwater superoleophobicity for successful separation of oil/water mixtures was presented. A simple, quick, and low-energy-consuming one-step electrodeposition approach created a Zn-ZnO electrodeposited copper mesh. All measured oil/water combination separation efficiencies are more significant than 99.0 percent, and incursion pressures for all tested oils that the mesh can tolerate are more significant than 1.5 kPa [53].

Sol-gel method: The sol-gel approach involves first preparing a low viscosity solution and then coating the material's surface with a sol-gel membrane. This approach can accomplish even doping at the molecular scale with a lower synthesis temperature [44].

Jiang et al., in their paper, reported that combining a polydopamine (PDA) adhesive layer between the TiO_2 layer and the glass, the substrate has improved the wettability and wear resistance of titanium dioxide (TiO_2) thin films. Sol-gel dip-coating method was used to deposit coating layers of TiO_2 thin film generated from sol-gel precursor on PDA precoated glass substrate. Creating a mixed layer between the TiO_2 and PDA layers, which strengthens the adherence of the TiO_2 layer to the substrate and hence the wear resistance of TiO_2/PDA thin films, is credited with the enhanced wear resistance [16]. In Huang et al. literature, a one-step sol-gel technique was used to create a non-laminated graphene oxide membrane crosslinked by polyethyleneimine. Due to the report used the superhydrophilic membrane to separate a series of oil-in-water emulsions that were both surfactant-free and surfactant-stabilized. With only gravity and no added power, a high separation efficiency (>99 percent) and flux were attained, substantially bigger than commercial filtering membranes with similar permeability characteristics [21]. Figure 4 is a schematic sample of the sol-gel process.

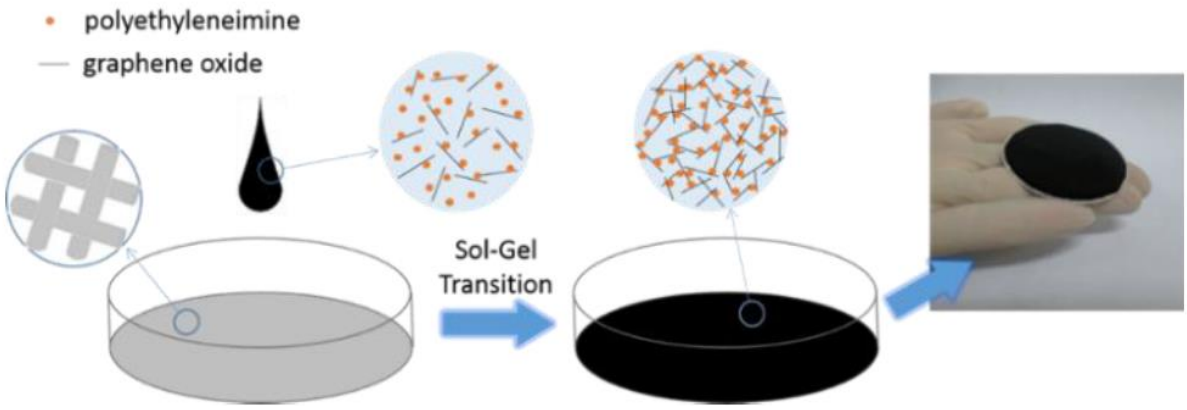

Figure 4: *Schematic illustration of the formation of a polyethyleneimine via the sol-gel process*[21].

Chemical etching: Etching is an easy and low-cost way to make rough structures, and it's commonly used to make superoleophobic surfaces. Depending on whether solutions are

employed, it may be divided into wet and dry etching. In items with basic electronics, wet etching is used. Surface topography, on the other hand, is challenging to manage, especially for smaller materials. Dry etching is more accessible to regulate than wet etching and produces no waste liquors. However, the necessary equipment is more complicated and costly.

Furthermore, because the material is removed from the original surfaces, the surfaces formed by both wet and dry etching are brittle [54]. The chemical etching process involves corroding the surface of materials with a strong acid or alkali solution, resulting in a micro-nano rough texture on the surface. The initial corroded area on the metal mesh's surface will form a pit, and then a rough surface structure will emerge [44]. To better understand wetting behavior, Liu et al. (2013) created an artificial superhydrophilic surface that mimicked fish scales. Their research chose smooth silicon surfaces, microstructured silicon surfaces, and micro/nano-hierarchical structured silicon surfaces as the modeling surfaces. Chemical etching was used to create silicon wafers with micro/nanostructures, then submerged in hydrofluoric acid and silver nitrate solutions. The artificial interfaces were made from polyacrylamide hydrogels produced using a casting process. Microstructured silicon surfaces and micro/non-hierarchical structured silicon surfaces reveal a hyper hydrophilic surface with WCA< 5^{o} compared to smooth silicon surfaces with WCA 52.5^{o} in their study [45].

2.4.3 Physic-Chemical Methods

Chemical vapor deposition: Chemical vapor deposition (CVD) is a method of producing solid deposits by causing chemical reactions on solids using gaseous gases. The advantages of this approach are ease of use, homogeneous coating, conformability, and excellent stability [44]. Plasma treatment, UV light irradiation, laser treatment, and microwave irradiation

can all be used to create a superhydrophilic surface by vapor deposition [55]. Lai et al. (2008) provided a novel two-step photocatalytic lithography method for fabricating superhydrophilic–superhydrophobic micropatterns on the TiO_2 nanotube structured film. The superhydrophobic TiO_2 nanotube film is created in the first step using electrochemical and self-assembled processes. The superhydrophobic film is then selectively subjected to UV light using a photomask in the second stage, which photocatalyzed the organic monolayer built locally on the TiO_2 nanotube surface. Due to the change in surface composition and higher wettability provided by the rough TiO_2 nanotube, the water droplet thoroughly wetted the film with a CA less than 5°[56].

Laser ablation: High precision, environmental friendliness, and non-contact manufacturing are all advantages of laser ablation. The most common types of laser ablation processing are point-by-point scanning and line-by-line scanning. The surface roughness structure is created by consuming the substrate itself, comparable to the chemical etching process [57]. Zupancic et al., in 2015 used a laser to treat a polydimethylsiloxane-coated silica fume, for example. Compared to the hydrophobic coating of 138, the hydrophobic coating after pulsed Nd: YAG thermal laser treatment becomes superhydrophilic with WCA$<1^{o}$ [58].

2.5 Methods to Characterize the Superhydrophilic and Superoleophobic Surfaces

2.5.1 Contact Angles and Contact Angle Hysteresis (or Sliding Angle)

Static contact angle measurement is the most common approach for quantifying the hydrophilicity or oleophobicity and using an optical-based contact angle measure of manufactured surfacesurement instrument [35,42,59]. The contact angle changes throughout the three-phase contact line for a liquid drop lying on a rough and/or heterogeneous solid surface. If

the system is in equilibrium, the actual contact angles are identical to Young's contact angles. Variations in the inclination of the rough surface and take in the chemistry of a heterogeneous surface produce local changes in angles (cause the three-phase contact line to contort). The local angles are not recorded since the contact angles usually are determined macroscopically for liquid droplets with a few millimeters diameter using low-magnification optical lenses [35,36,60].

Since the turn of the twentieth century, it has been generally accepted that both advancing and receding contact angles should be measured and reported. The advancing contact angle has been defined as the highest metastable contact angle observed for a liquid drop that progresses or recently advances across an unwetted solid surface under specific natural vibrations since the 1960s [11,61,62]. The minimal metastable contact angle recorded for the liquid retreating or recently retreated from the wetted material under natural vibrations is the receding contact angle . The advancing and receding contact angles are metastable equilibrium contact angles because they can release various values when mechanical stimuli are applied to the system. Experimental advancing and receding contact angles are the Gibbs energy curve's maximum and lowest contact angles. Figure 5 has a local minimum from which the liquid cannot escape via natural vibrations. The most stable contact angle for a given system corresponds to the lowest Gibbs energy [64–68].

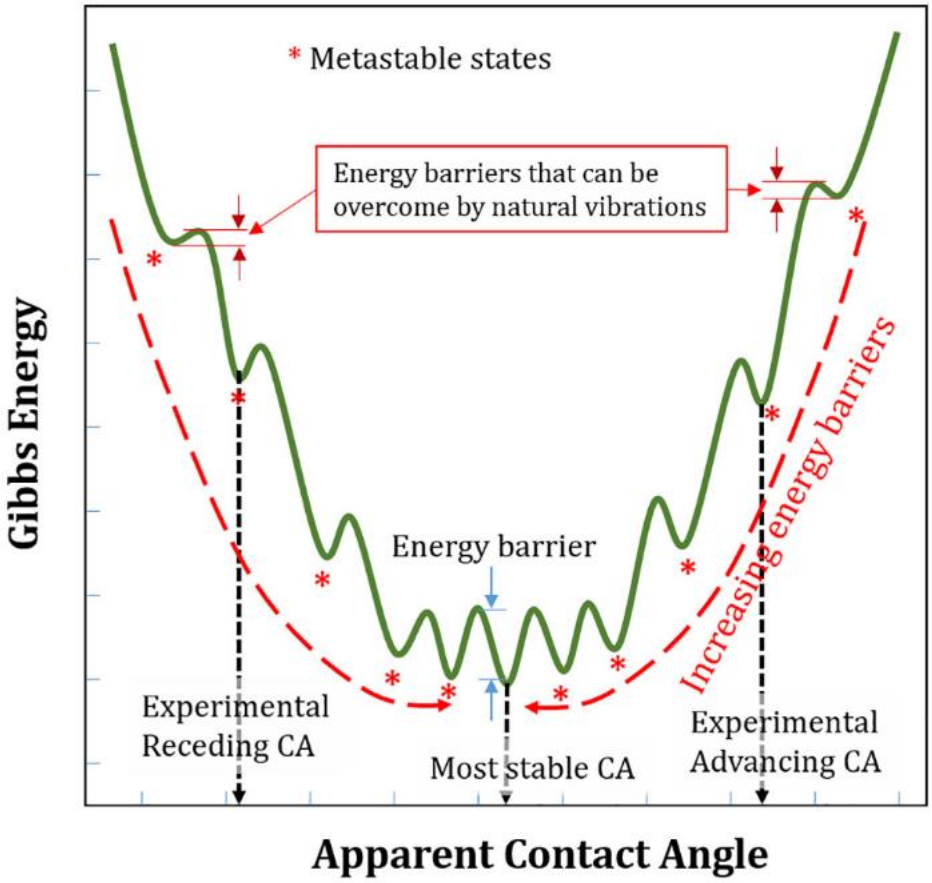

Figure 5: *The Gibbs energy for a liquid on a heterogeneous and/or rough solid surface about apparent contact angle.*[67]

The Gibbs energy, which considers surface geometry, topography, and local wettability characteristics, may be used to explain the occurrence of various liquid-solid metastable configurations. A link between Gibbs energy and apparent contact angle for a liquid on a heterogeneous solid surface is shown in Figure 5. A rough surface might be represented by similar graphs [67].

However, there are flaws in research on contact angle measurements for solid objects under vibrations. To begin with, there is no way to verify that vibrations result in liquid

spreading in its most stable condition. This uncertainty is not present in the microbalance technique given in the second half of this contribution [59,61,69].

The thermodynamic relationships of Wenzel, Cassie, and Cassie-Baxter are only valid when they are obtained from infinitely tiny displacements produced by a liquid across an area with no change in topography or heterogeneity pattern. Furthermore, any heterogeneity or asperity must be orders of magnitude more significant than the size of a liquid drop or contact line in general. Such surface properties are seldom fulfilled on actual surfaces. Therefore, the surface topography underneath the three-phase contact line, as well as the consequent form of the liquid perimeter, are more essential. The term "wetting contact line" does not fit into a one-dimensional mathematical definition of length. Surfaces and interfaces, and hence the contact line, have vertical dimensions in the actual world determined by the sizes of molecules and atoms. Interfacial forces act on a junction of three interfaces at the contact line, contributing to its structure and features [59,66,70].

Experimental advancing and retreating contact angles result from a mix of factors, including solid surface energy, sample shape, size, roughness and heterogeneity features. As a result, several recent efforts have focused on direct measurements of liquid-solid interactions, which began with developing two devices. During spreading, adhesion at its most stable stage, and separation, the system captures forces. Force barriers in transitions from spontaneous spreading to maximum adhesion and finally pull-off may be measured. Contact angles may be utilized to analyze advancing, retreating, and most stable contact angles, as well as contact angle hysteresis, because they are calculated from collected pictures (Figure 6). Using a microbalance to measure contact angles for droplets in their most stable shape has a considerable advantage over previous attempts to reinforce a liquid to relax to the most stable state or close to it using

mechanical or acoustic vibrations. The contact angle at the exact point of the most stable condition may be calculated using the microbalance–camera system at the same time [67].

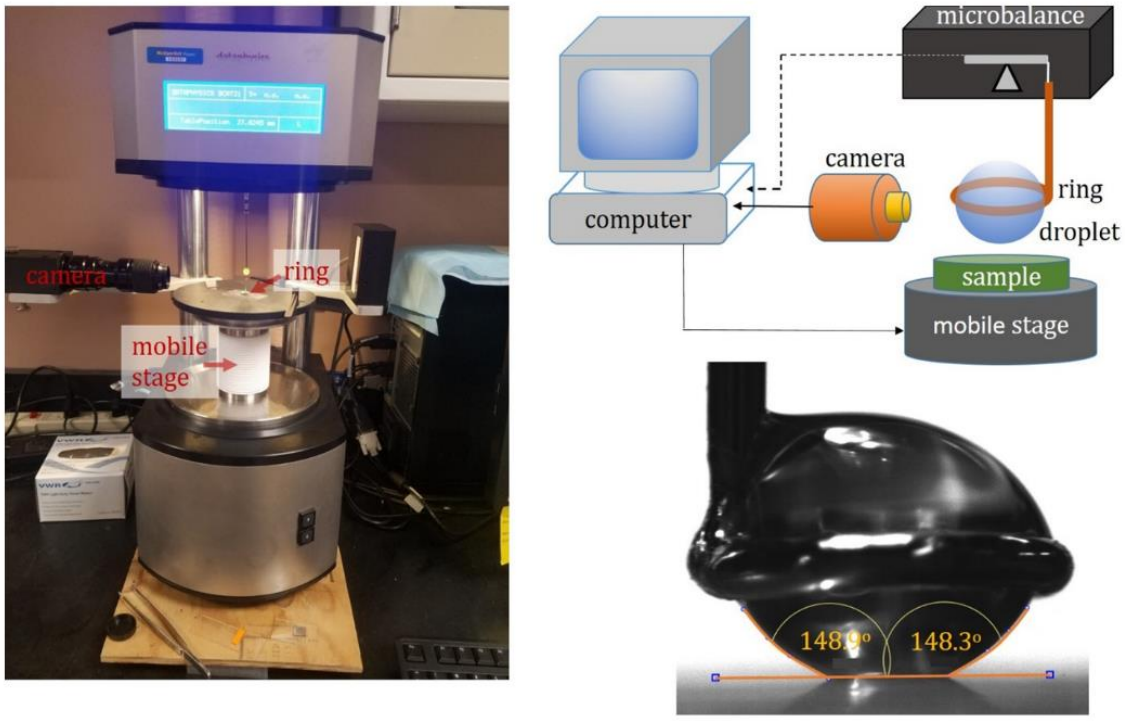

Figure 6: *Microbalance and experimental set-up used in adhesion force measurements between water droplets and solids. Optical image of a water droplet in contact with hydrophobic pattern with marked, measured contact angles*[67].

2.5.2 Scanning Electron Microscopy (SEM)

The scanning electron microscope (SEM) is one of the most versatile tools for examining and analyzing microstructure morphology and chemical composition characterizations. To comprehend the foundations of electron microscopy, we must first understand the basic concepts of light optics. The acquisition of signals produced by electron beam and specimen interactions

is required for image creation in the SEM. There are two types of interactions: elastic interactions and inelastic interactions [71].

The incoming electron is deflected by the specimen atomic nucleus or outer shell electrons of similar energy, resulting in inelastic scattering. A wide-angle directional shift of the dispersed electron and low energy loss during the collision define this type of interaction, as shown in Figure 7. Backscattered electrons (BSE) are incident electrons that are elastically dispersed at an angle greater than 90 degrees and produce a suitable signal for imaging the material [72].

When an incoming electron collides with a specimen atom, instead of being deflected off instantly, the intense electrons burrow into the sample for a bit of distance before colliding with an atom. The central electron beam creates a zone of primary excitation resulting from which various signals are generated. The size and form of this zone are substantially determined by the beam electron energy and the specimen's atomic number, hence density [71].

The secondary electron emission signal is the most extensively utilized signal produced by interacting the primary electron beam with the specimen. Secondary electrons are produced when the primary beam collides with the sample surface, causing the ionization of specimen atoms. They can only escape from a zone within a few nanometers of the material surface because of their low energy, generally about 3–5 eV. As a result, secondary electrons mark the beam’s position precisely and provide high-resolution topography data [71,73].

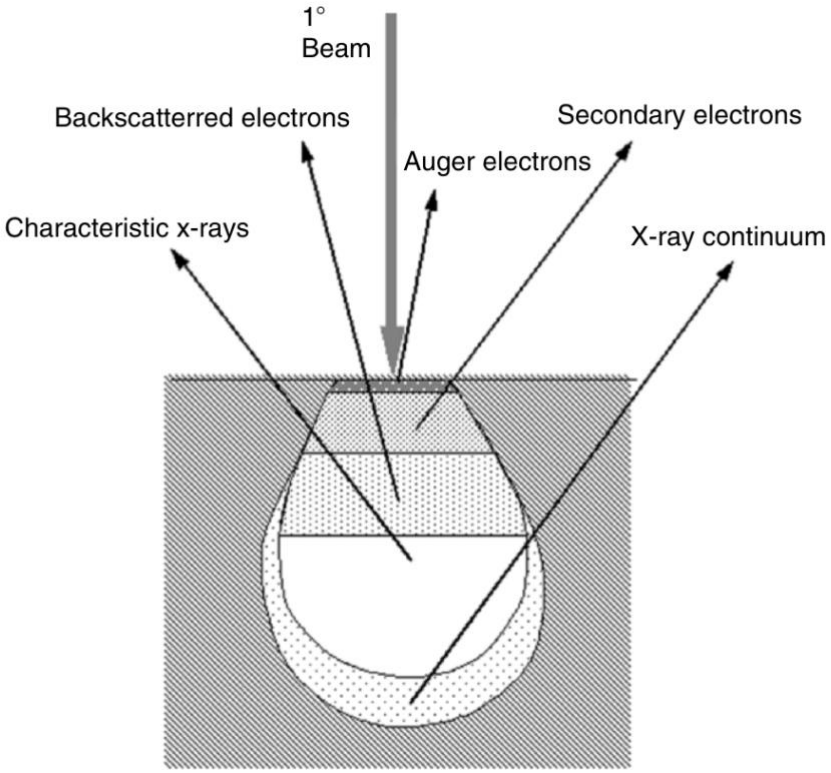

Figure 7: *Illustration of several signals generated by the electron beam–specimen interaction in the scanning electron microscope and the regions from which the signals can be detected* [71].

2.5.3 Energy Dispersive X-ray (EDX)

An energy-dispersive X-ray (EDX) system may count individual X-ray photons incident on the detector and distribute the counts into various histogram bins based on energy, allowing for "parallel detection" of a wide range of X-ray energies [74].

Good performance in the subject of elemental microanalysis should assist answer all or part of the following questions: Qualitative: What components are present in the sample at a specific location? Quantitative: At what point in the sample is each element's concentration highest? Spatial: Are there any compositional differences in the field of view field[74]?

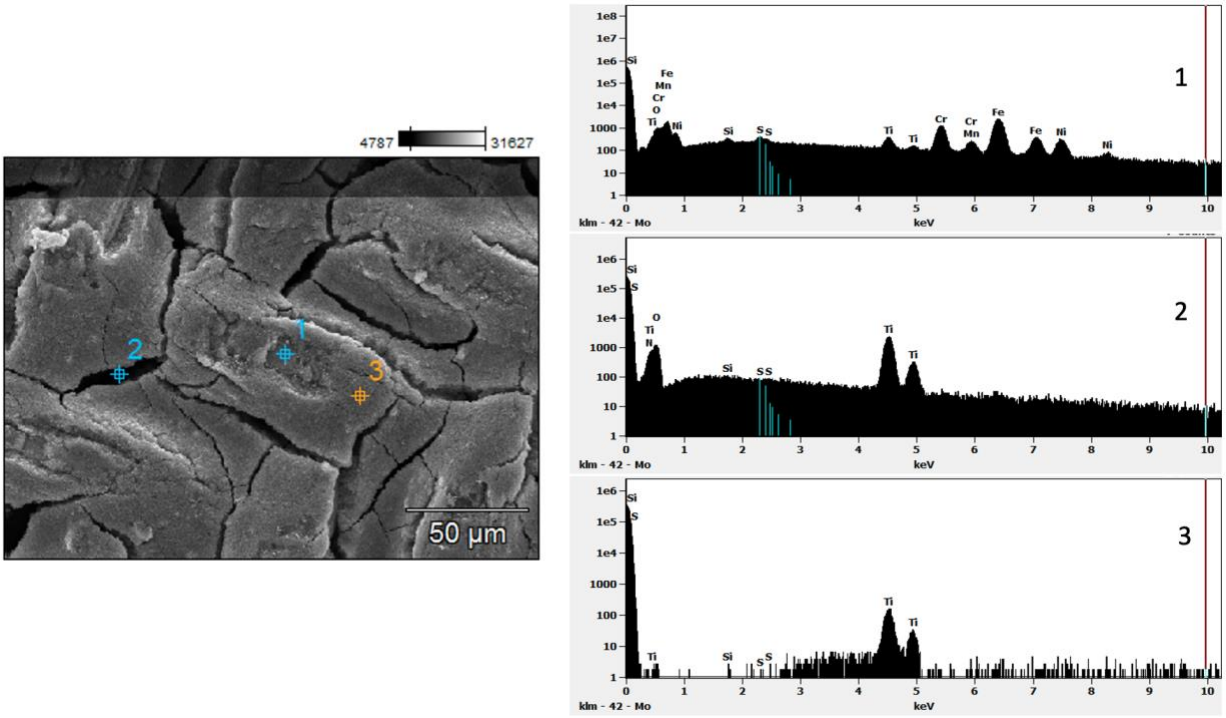

Figure 8: *Energy dispersive X-ray analysis of different points in the same scan area showing a different elemental composition of each point.*

EDX can identify elements with atomic numbers more than boron, which can be identified at concentrations of at least 0.1 percent. Material assessment and identification, contaminant identification, spot detection analysis of areas up to 10 cm in diameter, quality control screening, and other applications are all possible with EDX [75]. EDX analysis is commonly used to scientifically evaluate the content of corresponding elements in the scanning region when elemental detection in ceramic samples is required. EDX data may be shown in a variety of ways. First, by directing the electron beam to a specific place in the scan region, a localized elemental distribution of the sample may be created [75,76]. EDX measurements can also be shown by creating a plot of relative elemental distribution along a horizontal line in the

sample's scan region [75]. Figure 8 shows an example of EDX analysis of the elemental composition of different points in the same scanning area.

2.5.4 Fourier Transform Infrared Spectroscopy (FTIR)

Fourier transforms infrared spectroscopy is a frequently used vibrational spectroscopic method for chemical analysis of biological materials. Because most inorganic and organic components in the environment have dipole moments, they are active in infrared (IR) radiation. This spectroscopic approach involves absorbing energy from a photon, facilitating the transition from a lower-energy state to a higher-energy state [77]. Higher-energy conditions cause molecular bond vibrations (stretching, bending, twisting, rocking, wagging, and out-of-plane deformation) in the IR portion of the light spectrum at various wavenumbers (or frequencies). The inherent physicochemical features of the relevant molecule dictate the wavenumber of each IR absorbance peak. As a result, this is identified as a fingerprint of that functional group [77,78]. The absorbance is shown against wavelengths ranging from 700 nm to 400 000 nm, with wave numbers going from 14 000 cm1 to 25 cm1.

The molecule vibrates more as it absorbs energy, stretching and bending depending on its geometry. The absorption spectrum pattern is similar to a fingerprint that identifies the molecule and may be used for both quantitative and qualitative examination [77]. As shown in Figure 9, transmission FTIR (e.g., potassium bromide (KBr)-pellet FTIR), attenuated total reflection (ATR)-FTIR, and diffuse reflection infrared Fourier Transform (DRIFT) spectroscopy are the most often utilized FTIR methods for bulk material characterization. Transmission FTIR is a quick and low-cost technology that has been widely employed in chemistry, geology, and other

scientific domains [78]. Figure 10 is a sample of chemical maps for a microscopic field with distinct sporinite.

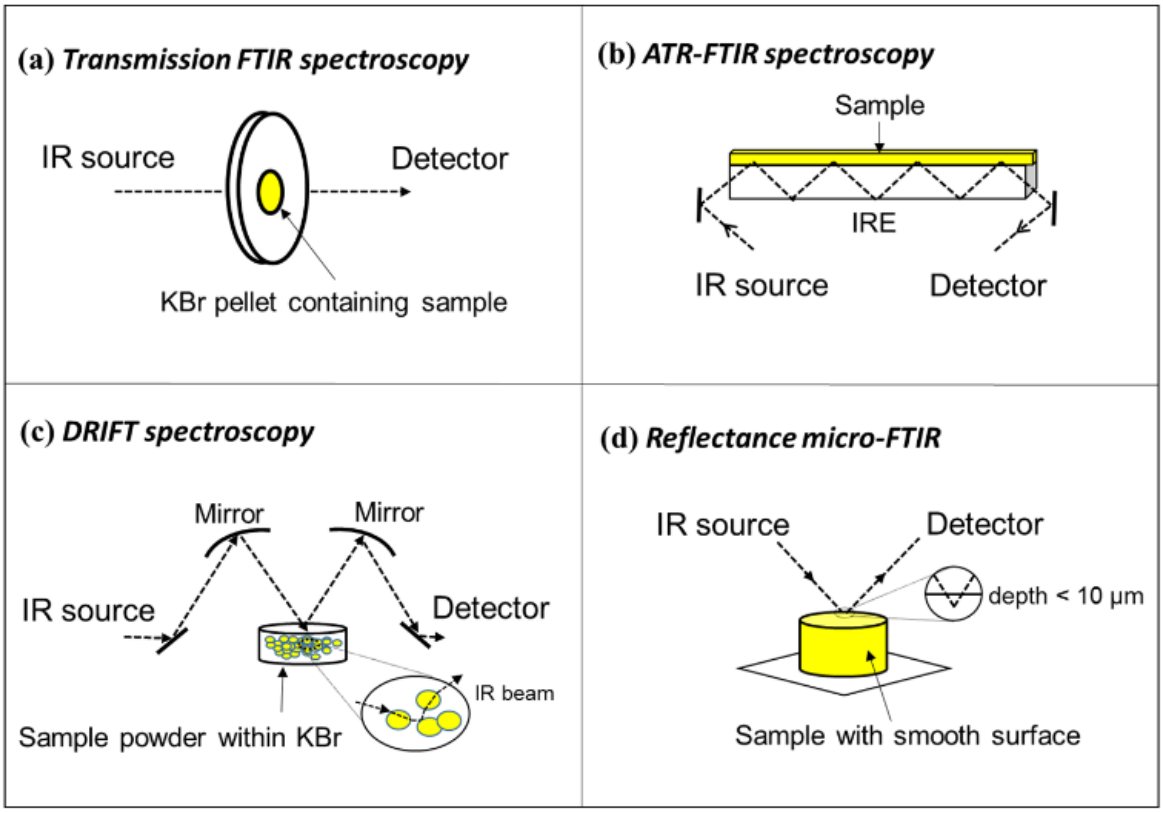

Figure 9: *Simplified schematics of standard Fourier transform infrared spectroscopy (FTIR) analysis modes [78].*

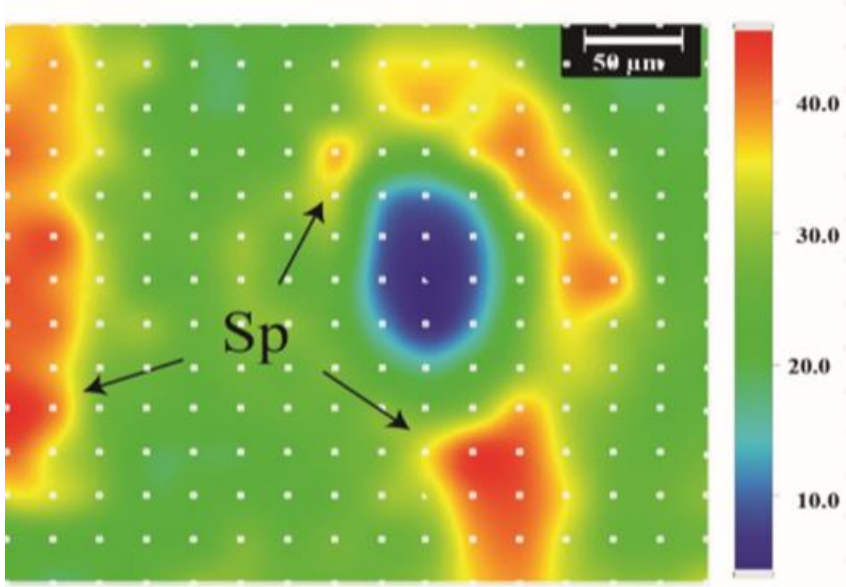

Figure 10: *Chemical maps of a microscopic field with distinct sporinite (Sp)* [78].

2.5.5 Transmission Electron Microscopy (TEM)

Since its introduction in the early 1940s, transmission electron microscopy (TEM) has been an essential tool in cell biology. The most common TEM use in cell biology is imaging dyed thin slices of plastic-embedded cells by passing an electron beam through the sample and absorbing and scattering the beam, resulting in contrast and a picture. The electron beam's tiny wavelength (100,000 times shorter than photons in visible light) allows TEM to attain struggle resolution, which is significantly less than that of even the highest-resolution light microscopes (20 nm) [79].

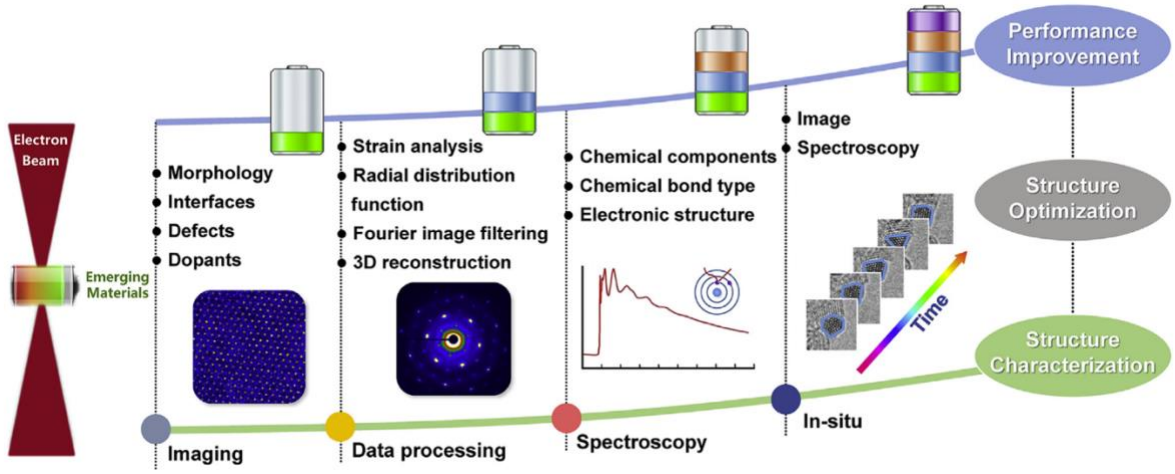

Figure 11: *Schematic illustration of the analytical TEM techniques for emerging advanced materials* [80].

The broad-beam approach, which employs a parallel incident beam and captures coherent data, has traditionally dominated high-resolution (HR) TEM. HRTEM has been widely used in microstructure characterization due to its quick signal collecting time and good picture resolution. The HRTEM picture, on the other hand, is strongly thickness- and defocus-dependent due to the crucial roles of specimen thickness and objective focus in the contrast transfer function [79,81] (Figure 11).

Three methods are widely used for TEM experiments, drying, staining, cryo-TEM or a combination of these methods [79,82,83].

The most accessible and extensively used approach for studying self-assembly and vesicles is drying (including freeze-drying). Before imaging, a 2–5 µl sample drop is put on a carbon or polymer-coated grid and allowed to dry for a few minutes to several hours. The approach is based on material sciences and is best suited for exceedingly stable materials [82].

Negative staining is preferable to drying for the soft stuff. Heavy metals can be used to stain a sample to preserve it and improve contrast. A potent scattering agent, such as iodine, ruthenium, or osmium tetra-oxide, is a positive stain that sticks to certain parts of the sample. A negative stain stains the surface and surrounds, hiding the item and any internal structural elements and giving it a footprint-like look [83].

Cryo-TEM photographs the material in its most natural condition instead of negative staining. By putting and then blotting a drop of sample on a lacy or holy carbon-covered grid, the sample is vitrified in a small layer of solvent and photographed at shallow temperatures, ensuring that the medium does not change phase evaporate in the high vacuum. Water is vitrified by rapidly chilling it, commonly by immersing it in liquid ethane cooled to its melting point[82,83].

2.5.6 X-ray Diffraction (XRD)

In solid-state and materials chemistry, X-ray diffraction (XRD) is critical since it may reveal the phase composition, chemical content, and crystal structure of the material under investigation. The complexity of the analysis varies greatly: at the most basic level, XRD is utilized for phase identification using the "fingerprinting approach [84]." Diffraction patterns develop when an x-ray beam impinges on a crystalline material, reflecting its structural and physicochemical properties. Every crystalline material makes a pattern; the same substance produces the same pattern every time; and in a combination of substances, each ingredient has its own pattern independently of the others." [85]. Quantitative X-ray powder diffraction analysis is widely used to determine the ratio of the various phases present in a multi-phase mixture, especially in the cement industry. The technique's foundation is understanding the X-ray scattering from each crystalline phase inside a material, which necessitates crystal structure data

for each phase. This can be complemented by inserting a known weight of standard material, allowing the fraction of any amorphous substance to be estimated by difference [84]. XRD has several advantages, including non-destructive nature, high sensitivity, reliability, depth profiling (glancing incident angle), easy sample preparation, user-friendly system, convenient operational procedure, fast speed, effective resolution, low maintenance cost, proper automation, and simple data interpretation that can be used for both qualitative and quantitative analysis in a variety of applications. Yet, it has a number of drawbacks, including the use of hazardous radiations, as well as the need for a standard reference to match for inference and a costly apparatus [86]. A diffraction pattern can also be used to determine the percentage purity of a sample by taking into account the amount and composition of contaminants present [86,87].

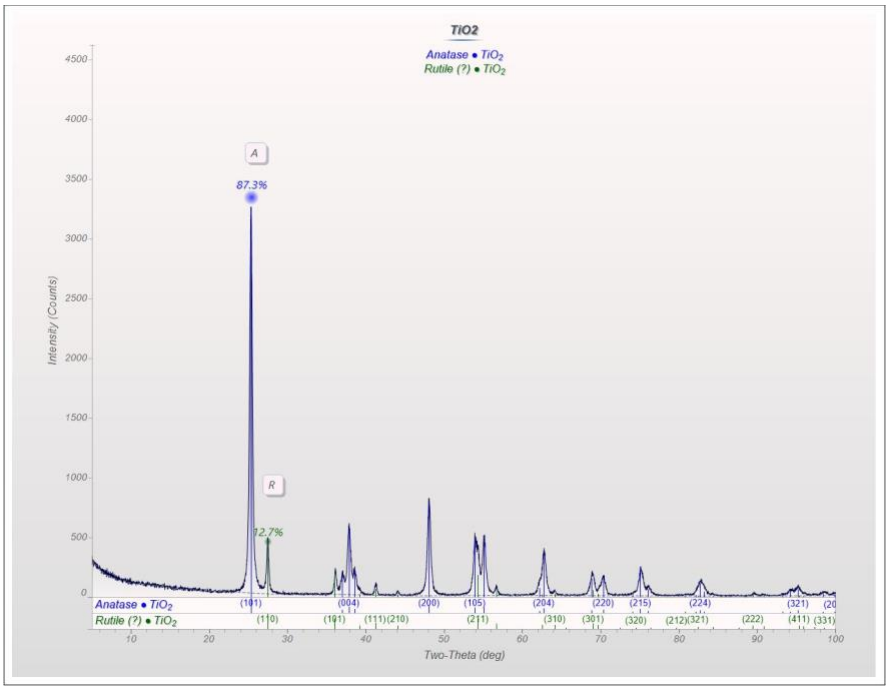

***Figure 12**: A typical XRD diffractogram showing a crystalline sample of TiO_2.*

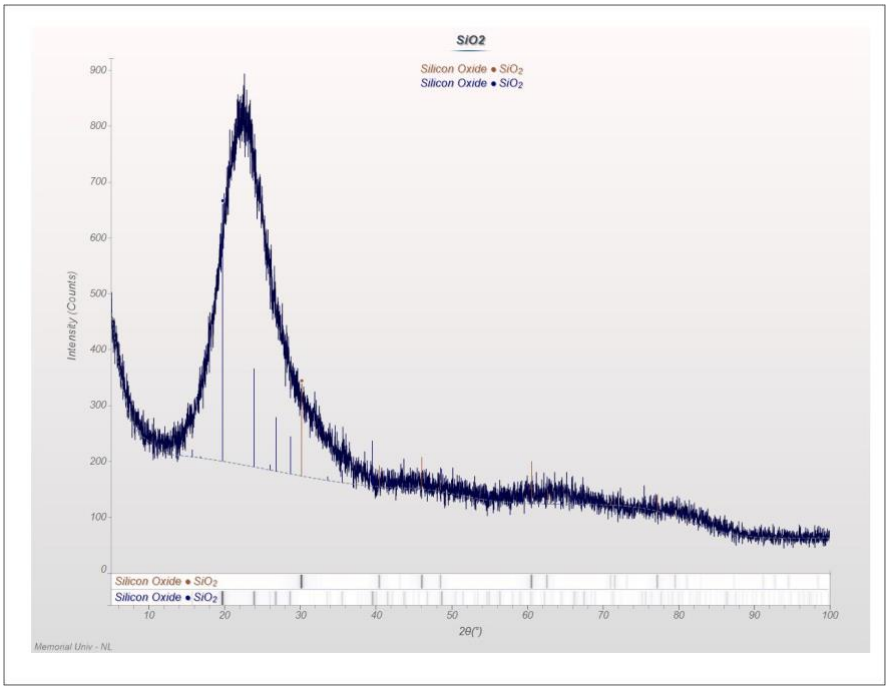

Figure 13: *A typical XRD diffractogram shows an amorphous sample of SiO_2.*

When crystalline substances are analyzed using XRD, they produce a diffraction pattern with a well-defined, narrow, sharp, and substantial peak, as shown in Figure 12, whereas amorphous in Figure 13, materials produce a pattern with noise signals, smeared peaks, or short order bumps like. Many polymers have semi-crystalline behavior, resulting in a halo pattern. By comparing the integrated intensity of the background pattern to that of the sharp peaks, powder XRD may be used to estimate crystallinity. The percentage crystallinity and crystallinity index have been calculated in various ways by various scientists[84,86,88].

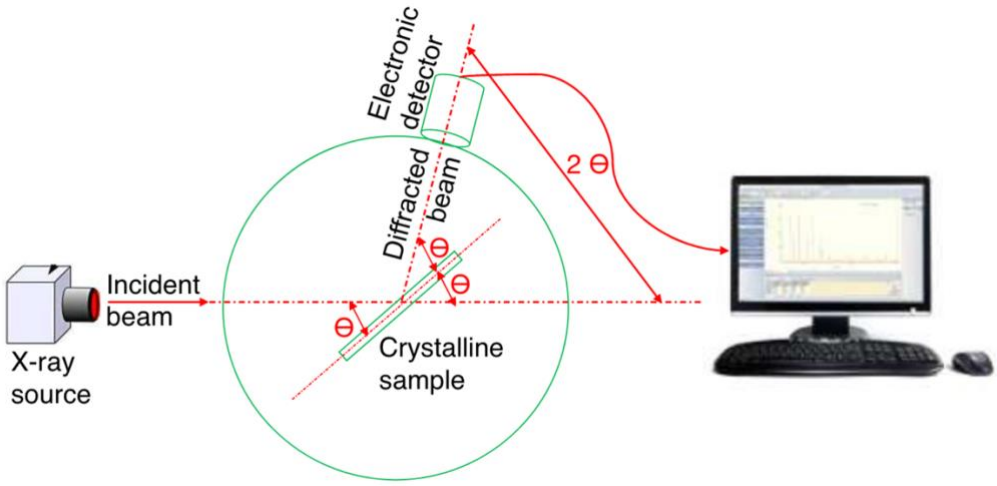

Figure 14: *XRD instrument schematic. An incident x-ray beam shines on the surface and a film or electronic detector captures the signal as it completes an arc* [85].

The x-ray wavelength is determined by the binding energies of the electrons participating in the electronic transition and the soler slits provide a small band of collimated x-ray wavelengths that is directed to the sample Figure 14. So, the radiation is diffracted by the sample at angles that follow Bragg's Law[85]:

$$n\lambda = 2d\ sin\,\theta \qquad (4)$$

Where n is an integer (1, 2, 3, 4,. . .), d_{hlk} marks the interplanar spacing generating the diffraction, and θ is the x-ray incident angle. This law describes the relationship between the wavelength of electromagnetic radiation and the crystalline sample's lattice spacing and diffraction angle. As the x-ray source completes an arc over the sample, the radiation diffracts in discrete directions in space, and an area detector or film records the reflections. The identity and location of the atoms in the unit cell are related to the position and intensity of the reflection[85].

By combining XRD with SEM/EDX/TGA/DSC/FTIR/Raman devices and micro reactors, it can now provide crystallographic data in situ, which may be used to solve problems in pharmaceuticals and other sectors.

2.5.7 X-ray Photoelectron Spectroscopy (XPS)

X-ray photoelectron spectroscopy (XPS) is widely considered an essential technology for the surface characterization and investigation of material after an applied treatment such as fracturing, cutting, or scraping [89,90]. For an XPS measurement, the typical depth of analysis is about 5 nm. Scanning the sample surface with a micro-focused X-ray beam allows spatial distribution data to be collected. Given the limited range of photoelectrons generated from the solid, the XPS method is quite surface specific. A concentric hemispherical analyzer is used to determine the energy of photoelectrons exiting the sample, resulting in a spectrum with a succession of photoelectron peaks. The peaks' binding energy (BE) differs depending on the element. The peak regions can be utilized to identify the material's surface composition. The chemical state of the emitting atom can somewhat modify the form of each peak and the BE. As a result, XPS can also offer chemical bonding information [90]. Because the analyzer is normally one meter distant from the X-ray irradiation surface in XPS surface investigation, a UHV system is required to acquire the highest electron count during the spectra acquisition. The ultra-high vacuum (UHV) surface analytical approach calculates the elemental composition of elements with an atomic number of lithium or above and determines the kinds of chemical bonds and oxidation state in the material surface in a qualitative and quantitative manner [91].

The element specificity of the binding energies and the relationship between the intensity of the photoelectron peaks and the element concentration provide quantitative information. The

energy location of a photoelectron peak compared to the energy position of the same level in a reference molecule provides qualitative information (chemical shift) [92]. In a single attempt, a survey scan (sometimes known as a wide scan) is undertaken with the BE spanning from 0 to 1200 eV. This will provide details on the components found in the sample, as shown in *Figure 15* [90].

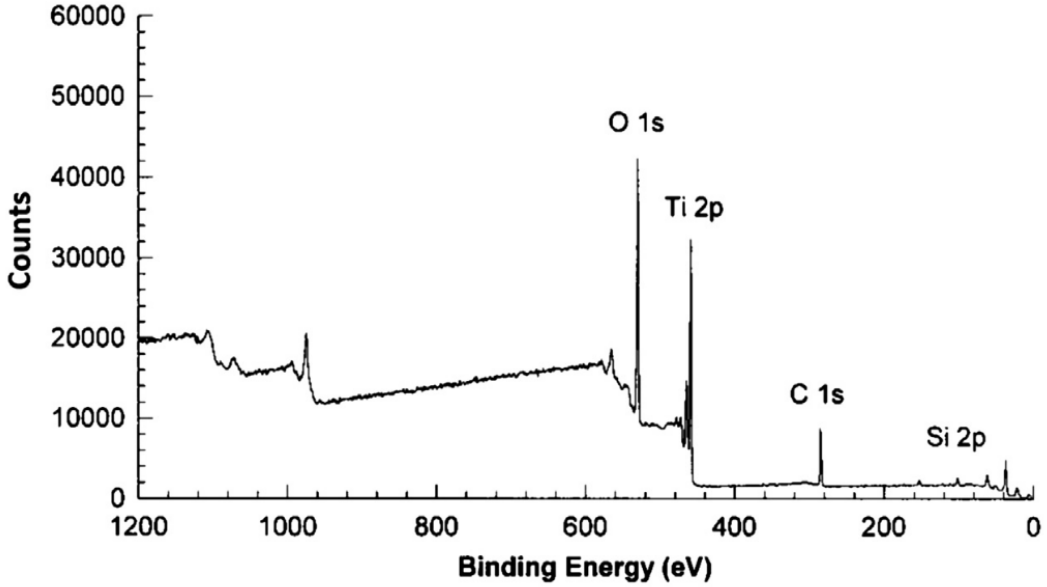

Figure 15: *Survey spectrum of titanium dioxide showing various titanium and oxygen peaks and a carbon peak* [90].

Apart from understanding the content, the atomic percentage composition of the components in the film can also be evaluated. The ratio of the suitable components can be used to assess the hydrophilicity and hydrophobicity of a film. It can also reveal the degree of cross-linking and linearity of a membrane's polymers [90,91,93].

2.5.8 Surface Energy Calculation

One of the fundamental concepts in surface physics is surface energy, which is defined as the surface excess free energy per unit area of a specific crystal facet. It controls the equilibrium form of mesoscopic crystals, is involved in faceting, roughening, and crystal development, and may be used to calculate surface segregation in binary alloys [94].

Since surface free energy cannot be directly measured, numerous models based on contact angle measurements have been presented. One of the most often cited surface-free energy theories is an estimation of surface energy through Neumann and Owen, Wendt, Rabel and Kaelble (OWRK) models. It distinguishes between polar and dispersive interfacial interactions. This model necessitates the measurement of the contact angle with two known liquids to calculate the surface free energy. All surface free energy theories are based on Young's equation. It refers to the force balance at the three-phase contact point where air, liquid, and solid collide ((1) [94–97].

The right side of the equation must be known or measured once the solid's surface free energy has been calculated. Surface tension and contact angle are simple to calculate, but interfacial tension between the liquid and solid phases is more challenging. Several attempts have been devoted to formulating the liquid-solid interactions. Young, as well as Antonow, suggested this idea.

$$\gamma_{sl} = \gamma_s - \gamma_l \tag{5}$$

This equation doesn't work if $\gamma_s > \gamma_l$. So, the equations were stated as follows by Good and Girifalco[98]:

$$\gamma_{sl} = \gamma_s + \gamma_l - 2f(\gamma_s \gamma_l)^{0.5} \tag{6}$$

where assumes ϕ =1. So, the OWRK equation is as follows:

$$\gamma_{sl} = \gamma_{sv} + \gamma_{lv} - 2\sqrt{(\gamma_{sv}^{D}.\gamma_{lv}^{D})} + \sqrt{(\gamma_{sv}^{P}.\gamma_{lv}^{P})} \quad (7)$$

where γ^D and γ^P are dispersive and polar components of surface tensions. From (1 and 7, we have:

$$\sqrt{\gamma_{sv}^{D}} + \sqrt{\gamma_{sv}^{P}}.\sqrt{(\gamma_{lv}^{P}/\gamma_{lv}^{D})} = 1/2\,[\gamma_{lv}(1+\cos\theta)]/\sqrt{\gamma_{lv}^{D}} \quad (8)$$

$$c + mx = y \quad (9)$$

where, c= $\sqrt{(\gamma_{sv}^{D})}$ and m = $\sqrt{(\gamma_{sv}^{P})}$ [98–100].

The OWRK model can determine the solid surface free energy with two or more known polar and dispersive liquids components. The OWRK approach divides interfacial surface tension into two categories: polar and dispersive interactions between molecules. As a result, the solid's total surface energy equals the sum of its polar and dispersive components. Permanent dipole-dipole interactions give rise to the polar component. In polar compounds, they are more powerful (having permanent dipole moment). When random variations in the electron density are brought together, the dispersive component emerges, resulting in an induced dipole-dipole interaction [98].

2.6 Summary

Superhydrophilic and superoleophobic surfaces are crucial in applications involving oil-water separation, such as the treatment of oily wastewater and the cleanup of oil spills. Despite significant attempts over the past decade, there hasn't been a thorough review report or work on the fabrication of superhydrophobic and superoleophilic surfaces. The manufacturing and characterization of the SS surfaces utilized in the oil-water separation procedures are reviewed in

this chapter. Additionally, it emphasizes the benefits and drawbacks of manufacturing and characterization methods, the state and future of SO membranes, and new research areas.

Most superhydrophilic and superoleophobic membranes have an oil contact angle (OCA)>150° and a will contact angle (OCA) < 5°, resulting in an high oil-water separation efficiency.

The performance of the meshes and membranes can be measured using methods like scanning electron microscopy (SEM), X-ray powder diffraction (XRD), Fourier transform infrared spectroscopy (FTIR), X-ray photoelectron spectroscopy (XPS), atomic force microscopy (AFM), and permeation tests. In contrast, only a few studies have used contact angle measurements to analyze short-term stability.

CHAPTER THREE

3 Experimental Setup, Methods and Procedure

3.1 Materials

The following mesh materials are purchased from YIKAI Store at Amazon: Woven Wire Stainless Steel 400 Mesh, 0.038mm aperture, 30µm wire diameter, Wire Filtration SS T316, Open Area 31%; Woven Wire Stainless Steel 200 Mesh 0.075mm aperture, 60µm wire diameter, Wire Filtration SS 304L, Open Area 34%; Woven Wire Stainless Steel 120 Mesh 0.125mm aperture, 80µm wire diameter, Wire Filtration SS 304L, Open Area 33%; Woven Wire Stainless Steel 80 Mesh 0.180mm aperture, 120µm wire diameter, Wire Filtration SS T304, Open Area 31%. These are the SS meshes that been used in our research.

Titanium (IV) Oxide ((TiO_2), MW: 79.88 gr/mol) Nanoparticles and Iodine (I_2) 99.999% are purchased from Fisher Scientific Canada, Silica ((SiO_2), MW:60.08 gr/mol) Nano-powder (10-20 nm), Acetylacetone 99+% are provided from Sigma Canada. These materials were used for preparing coating solutions.

Ethylene glycol and Dimethylformamide used for surface energy calculation tests, hexane and Terranova used as an oil in contact angle measurements and oil water separation tests, phenol red indicator was used to make the emulsion red, and dichloromethane (DCM) was applied for cleaning the meshes and distracting the oil. These materials were purchased from Sigma Aldrich (Winston Park Dr. Oakville, Ontario, Canada).

3.2 Fabrication of the SS Mesh

To prepare a superhydrophilic/superoleophobic stainless steel mesh, four main stages of (1) cleaning, (2) preparing coating solution, (3) coating and (4) characterizing must be included. Figure 16 shows the mesh fabrication procedure.

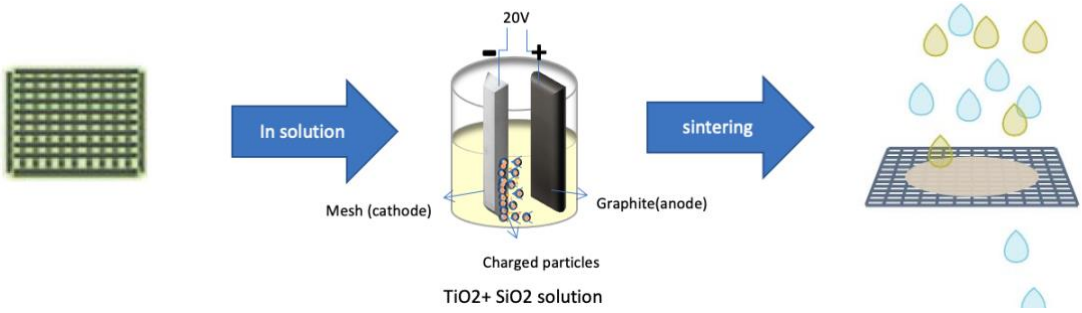

Figure 16: Mesh Fabrication procedure.

3.2.1 Cleaning

First, the SS mesh samples should be washed with soap or weak detergent and rinsed with warm water to eliminate dust and dirt. In the second step to remove the binder composition on the SS mesh surface, are first ultrasonically cleaned (for 1 hour) in Ethanol, rinsed with DI water, ultrasonically cleaned (for 1 hour) in Acetone, and rinsed with DI water again, then the mesh immersed in 10% Nitric Acid for 15 minutes with sonication to clean the rust on the mesh surface, and rinsed with DI water again. Finally, the cleaned mesh has been left at room temperature to dry. In the cleaning procedure, using ultrasonic is faster and more effective than other methods to remove the contaminants[14,51,101,102].

3.2.2 Coating Solution

To prepare TiO_2/SiO_2 SS mesh, with a trial-and-error approach, the optimal concentration of components in the solution was determined as: 0.5 g TiO_2, 0.004 g SiO_2, in 50 ml 2,4-

Pentandione (acetylacetone) 99+% as a solvent with addition of 0.04 g iodine 99.999% to generate TiO_2 positive charges in the solution. Then, the solution was sonically stirred for 1 hour to enhance its stability (Figure 17). After each electrophoretic deposition test, the solution was magnetically stirred for 5 min [23,24,103]. To check that we prepared the best mesh, these solutions without SiO_2 and with 0.008 g of SiO2 have been compared.

Figure 17: *Preparing the coating solution by sonication stirring.*

3.2.3 Electrodeposition Coating

Furthermore, electrodeposition is the most widely utilized additive-based strategy for fabricating the desired surface roughness. This technology is capable of altering the water repellent ability of the surface by manipulating the surface topography by establishing a homogeneous micron- or nanoscale structural roughness on the surface. [24,104,105].

TiO_2/SiO_2 coatings on SS mesh were produced by electrophoretic deposition (EPD). Electrodeposition was performed with a two-electrode electrochemical cell in the solution where the pre-cleaned SS mesh was used as a cathode and a piece of graphite as the anode. Both electrodes were held by a tweezed arm to enable them to be dipped into the prepared solution and the distance of 15mm between electrodes in the glass beaker (Figure 18). The best result found in electrodeposited time and applied voltages were 20 V and 2 min, respectively. Before sintering, the prepared meshes have been dried at room temperature for 24 h [23,24,106–108].

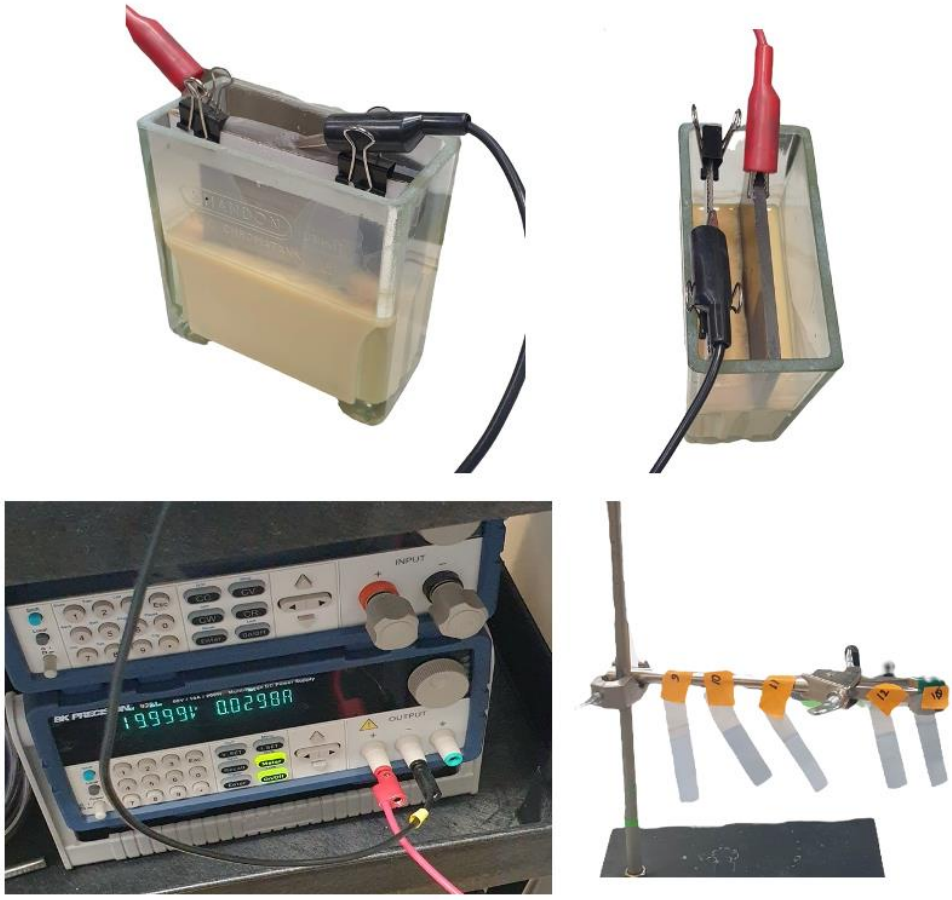

***Figure 18**: Electrodeposition procedure.*

3.2.4 Sintering

After coated meshes dried at room temperature the sintering was performed under a controlled Nitrogen atmosphere with a flow rate of 100 cc/min. Heating and cooling rates were 13 ˚C/min. Electric furnaces (Lindberg/Blue M™ Moldatherm™ Box Furnaces) were used for this purpose, and sintering was carried out at 800 ˚C for 1h dwelling time [23,107,109]. This process has been repeated at 500 and 650 ˚C to compare the results. Figure 19 shows the sintering instrument used in this study.

Figure 19: *Sintering procedure by Electric furnaces (Lindberg/Blue M™ Moldatherm™ Box Furnaces)*

3.3 Wettability Measurement

Contact angle measurement is the simplest and most widely used method for determining the hydrophilicity or underwater hydrophobicity of manufactured surfaces. To prevent contamination of the surfaces, the contact angle and surface energy measurements were performed by a video-based fully automated Data Physics drop shape analyzer device (krüss drop shape analyzer-DSA25) at room temperature (Figure 20).

To determine the hydrophilicity of the coated surface, contact angle (WCA/OCA) was measured by the sessile drop method. The measurements were carried out by placing the coated meshes in a cubic and transparent quartz container filled with seawater and the oil droplet was placed under the mesh through an inverted needle; an aliquot of 4 μL of x-hexane and Terranova were used as a solvent.

The surface energy of the surface is calculated by dispensing solvent droplets (4 μl/drop) of the known surface tension solvents, DI water (more polar), ethylene glycol, formamide (intermediate polar & dispersive). This technique allows for exact observation of any dynamic changes to the droplet on the surface. With the help of this technique, contact angles may be estimated with a 0.1° accuracy. OWRK model was used, to assess the contact angles with four distinct test liquids and surface free energies (polar and dispersive).

To check the stability of the coated mesh, samples are aged in seawater (PH=7.4), 0.1 M H2SO4 and 0.1 M NaOH solutions for one month. For tests after each week, 10 days, there are five replicated mesh samples in a sealed bottle containing a chemical (acid, base, and seawater).

To account for any topographic and chemical inhomogeneity on the surface, the contact angle measurement data were averaged over at least five separates randomly chosen places on each sample.

***Figure 20**: krüss drop shape analyzer-DSA25 for measuring the contact angles*

3.4 Microstructure Characterization

The morphology of the electrodeposited SiO_2-TiO_2 on SS mesh was characterized by a cold field emission scanning electron microscope (SEM, FEI MLA 650FEG) equipped with Bruker EDX. An SEM paired with Energy-Dispersive X-ray Spectroscopy (EDX) detectors allows for the compositional investigation of materials. Variations in the material composition may be traced across a millimeter to micrometer scale using the SEM's EDX detector (microns). Electrons are used to bombard a sample surface, and the resulting x-ray energy and intensities are then measured. The specimen's elemental makeup is evident in the x-ray energies, and the strength of the x-rays is precisely related to the weight proportion of each of those chemical

components. The coated meshes were attached to an aluminum stub with double-sided carbon tape to characterize the samples.

The crystalline structure of the coatings was determined by X-ray diffraction with a Rigaku Ultima IV x-ray diffractometer with a copper x-ray source and a scintillation counter detector. The samples were performed with a Cu source at 40 kV and 44 mA over a diffraction angle range of 5.000-90.000 with a sampling width of 0.020. An X-ray tube, a sample holder, and an X-ray detector are the three fundamental components of an X-ray diffractometer. In a cathode ray tube, X-rays are produced by burning a filament to produce electrons, accelerating the electrons with a voltage toward a target, and then hitting the target material with the accelerated electrons [85,88,110]. Characteristic X-ray spectra are created when electrons have enough energy to knock inner shell electrons out of the target material. The sample's surface will be exposed to concentrated, collimated, monochromatic radiation produced by a cathode ray tube[84].

3.5 Oil-Water Separation Test

One of the most significant environmental issues in the world today is water that has been polluted by oil. Particularly, it was still quite difficult to separate oil-water emulsions. The as-prepared mesh ability to separate oil from water evaluated by the oil-water separation tests. The filtering procedure for separating an oil-water mixture is represented in Figure 22, a and b.

The separation tests were done using the emulsion. to prepare the emulsion, 313 µl of crude oil (Terranova) and 250 mL of water were mixed with the high-speed homogenizer (15000 rpm) for 5 min (Figure 21).

The coated mesh was fixed between two glass tubes and sealed by Teflon flanges. The Terranova and water emulsion was poured onto the water pre-wetted mesh. Oil was retained above the coated mesh due to the remarkable underwater superoleophobic qualities of the TiO_2/SiO_2 coated mesh, whereas water with a greater density than oil readily passed through the coated mesh. Additionally, no detectable oil (be able to see by eye) was found in the water that was collected, demonstrating great purity and successful separation of the oil/water emulsion (Figure 22,c and Figure 23).

***Figure 21**: Emulsion preparation procedure*

The concentration of oil components was measured and calculated by UV-vis, Fluorescence Emission light tests before and after passing through the mesh. From these experiments the oil-water separation efficiency were evaluated.

Also, Water flux and water intrusion pressure were also analyzed to further assess the impact of the coated meshes with varying levels of water adhesion on the effectiveness of oil/water separation.

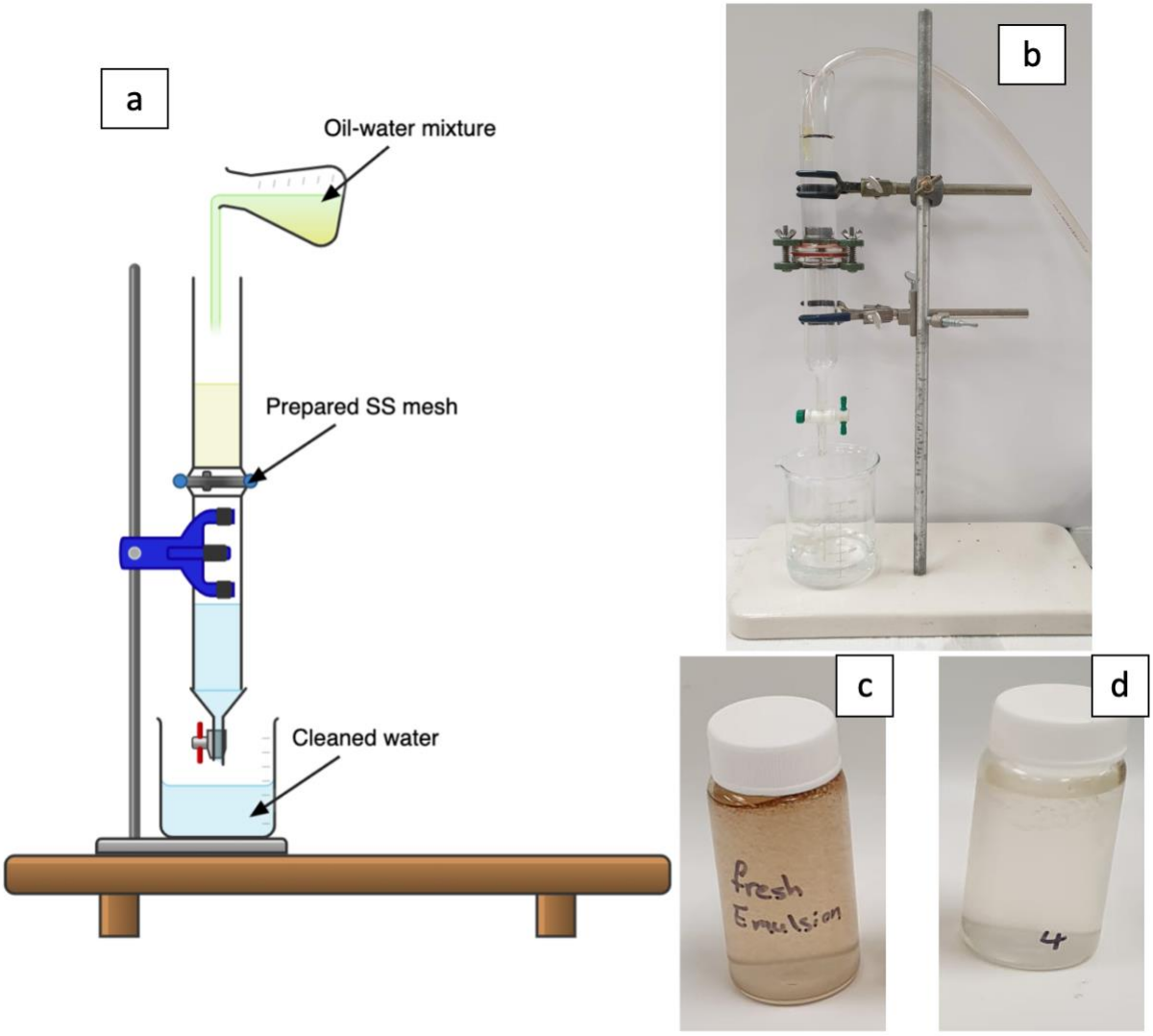

***Figure 22**: The oil-water separation system. a) and b) oil-water separation setup system, c) fresh emulsion, d) collected water after oil water separation test*

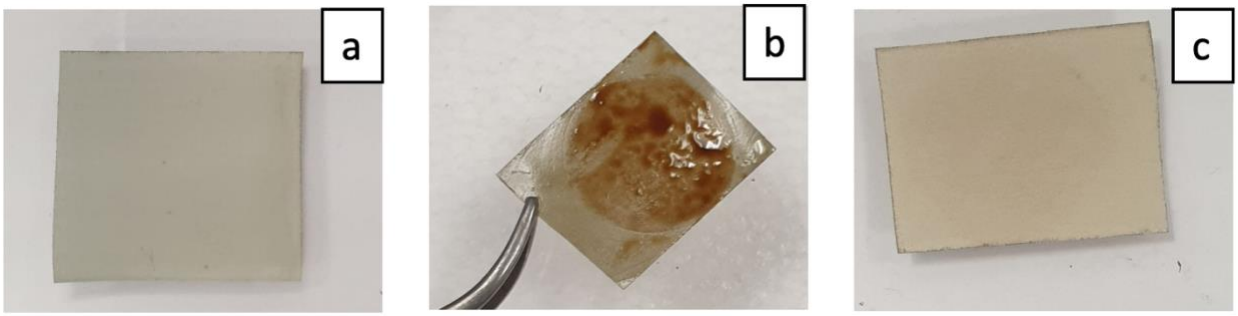

***Figure 23**: a) coated mesh before usage, b) coated mesh after oil water separation test, c) used mesh after rinsed by seawater*

3.5.1 UV-Vis and Fluorescence Tests

Oil Extraction and Analysis: All experimental and oil-water samples from the baffled trypsin zing flasks were extracted using the pesticide-quality solvent dichloromethane (DCM). The needed volumes of the oil and the dispersant were dispensed using a Brinkmann Eppendorf repeater pipettor by dispensing 2.0 ml to 20 ml. A Shimadzu Recording UV-VIS Spectrophotometer (Model UV-1800) that measures absorbance at 340, 370 and 400 nm was used to quantify the amount of dispersed oil [111]. The Concentration of oil is also calculated by the Cary 6000i UV-Vis-NIR spectrophotometer at mono-wavelength 260 nm. Fluorescence spectra were measured on a Photon Technology International (PTI) Quanta Master spectrofluorometer emission light excitation at 300 nm[111].

Our samples were prepared by mixing 2 ml of Terranova oil with 80 µl of dispersant, followed by 18 ml of DCM; a stock solution of the dispersant-oil combination was created, as shown in Figure 24. The mass measurements following each addition were used to calculate the concentrations of the stock solution. A precise amount of the stock standard solution was mixed with 30 ml of synthetic seawater in a 125 ml separatory funnel to create a nine-point calibration

curve Figure 44. The stock solution's volumes were changed to produce absorbance measurements within the spectrophotometer's linear dynamic range (LDR) [111]. The samples were then subjected to three liquid/liquid extractions, each employing 5 mL of DCM and the final extract being changed to 20 or 25 mL. (adjusted to maintain the LDR). When ready for analysis, the final extract was then put into 25 mL serum bottles sealed carefully and kept at 5 °C. the final extracted sample calls oil standard.

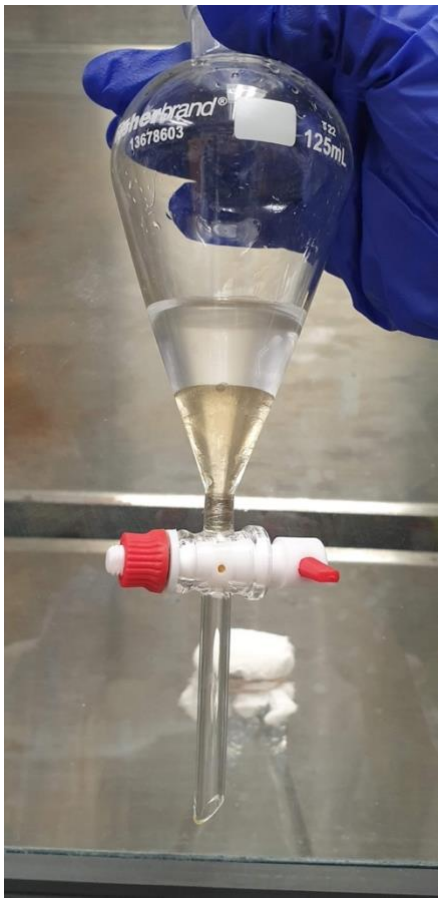

***Figure 24**: Oil distraction by DCM*

To analyze the extract, we recorded the absorbance at three distinct wavelengths of 340, 370, and 400 nm to measure absorbance at several wavelengths. Then, we computed the area

under the absorbance vs. wavelength curve using the trapezoidal method and the following equation: The lowest 95% confidence level of the 4 independent replicates is used to calculate the dispersion effectiveness value provided.

$$Area = \frac{(Abs_{340}+Abs_{370})\times 30}{2} + \frac{(Abs_{370}+Abs_{400})\times 30}{2} \quad (10)$$

where Abs_{340}, Abs_{370} and Abs_{400} are the absorbances at three discreet wavelengths of 340, 370, and 400 nm respectively[111].

Following an oil spill, an oil dispersant is a solution made of emulsifiers and solvents that aids in breaking up large drops of oil into smaller ones. Small droplets can more easily be dispersed over a water volume and may be more easily biodegraded by aquatic bacteria. When using dispersants, a trade-off must be made between exposing aquatic life to dispersed oil and exposing coastal life to surface oil. To calculate the Total Oil Dispersed and the percentage of oil dispersed (%OD), the area count is used based on the ratio of oil dispersed in the test system to the total oil added to the system, as follows:

$$Total\ Oil\ Dispersed(g) = \frac{Area}{Calibration\ Curve\ Slpoe} \times V_{DCM} \times \frac{V\ tw}{Vew} \quad (11)$$

where: V_{DCM} = volume of DCM extract, V_{tw} = total volume of seawater in the flask, V_{ew}= total volume of seawater extracted, and

$$\%OD = \frac{Total\ Oil\ Dispersed}{\rho oil \times Voil} \quad (12)$$

ρ_{oil} = density of the specific test oil, g/L, and V_{oil} = volume (L) of oil added to test flask[111].

After plotting the calibration curve and calculating OD, the oil concentration of extracted samples took before and after passing through the coated mesh were measured by UV-Vis at three distinct wavelengths of 340, 370, and 400 nm. From these experiments, the concentration of oil in the samples before (emulsion) and after passing through the mesh (treated water) was measured and the removal efficiency were calculated by the following equation

$$Removal\ Efficiency\% = (OC_{Emulsion} - OC_{Treated\ water}/OC_{Emulsion}) \times 100 \qquad (13)$$

where $OC_{Emulsion}$ is the measured oil concentration of emulsion and $OC_{Treated\ water}$ is the measured oil concentration of the treated water.

The samples extraction process was same for fluorescence and mono wavelength UV-Vis tests.

3.5.2 Water Permeating Flux and Oil Intrusion Pressure

Water flux and water intrusion pressure were also evaluated to further analyze the effects of the coated meshes with various levels of water adhesion on the efficiency of oil/water separation.

In a particular separation experiment, 400 ml of water was rapidly poured into the filter system. Water poured through the barrier and into the beaker below due to the force of gravity, as shown in Figure 25. The time it took to collect 400 ml of water passed through coated mesh

and non-coated mesh was noted, and the water permeating flow was calculated using the formula below.

$$F = \frac{\Delta V}{A\,\Delta t} \qquad (14)$$

where ΔV is the volume of filtrate collected in the beaker, Δt is the time taken to collect the filtrate, and A is the effective separation area of the mesh [112].

The oil/water pressure resistance of the coated mesh ΔP was evaluated by measuring the oil intrusion pressure equation as follows:

$$\Delta P = \rho g h \qquad (15)$$

where ρ is the density of the oil used for testing, g is the gravitational acceleration constant, and h is the maximum height of oil that the membrane can support without intrusion (the height of the oil was obtained from the average three individual experiments)[112,113].

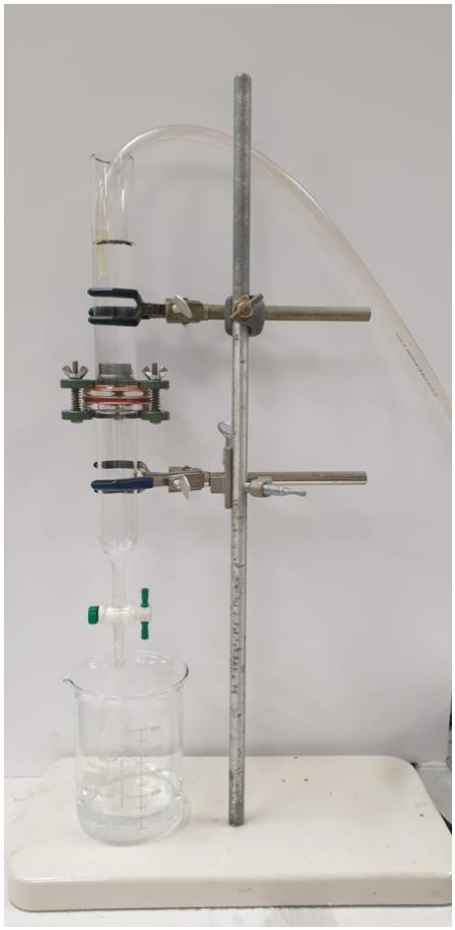

Figure 25: *The process of water permitting flux calculation*

3.6 Summary

In this chapter, each step of the fabrication process of the coating is explained in detail. Four different SS mesh sizes were used (80, 12, 200 and 400). All cleaned meshes were fabricated by the electrodeposition method by TiO_2 solutions with different SiO_2 concentrations. Prepared meshes dried at room temperature and sintered at three different temperatures (500, 650 and 800 ^oC).

The process and tools utilized for electrodeposition coating sample preparation and application are described. Following manufacturing, the samples' surface wettability and electrothermal characteristics are assessed. In this study, Terranova and hexane were used to measure the underwater CA.

The coating's micro-nanostructure was studied using scanning electron microscopy (SEM) and the crystalline structure of the coatings was determined by X-ray diffraction (XRD).

The setup structure and the process of preparation of emulation were discussed, followed by oil-water separation efficiency tests.

CHAPTER FOUR

4 Results and Discussions

This chapter presents the results to characterize the SS coated mesh. This analysis includes wettability tests, surface characterizing tests and oil-water separation tests.

4.1 Mesh Wettability Analysis

4.1.1 Contact Angle Measurements

The SS mesh count 400 samples are coated in our prepared solution with different concentrations of SiO_2 and sintered at 800°C. The relation between the concentration and the underwater contact angles with two solvents Hexane and Terranova have been shown in Table 1 and Figure 26.

Table 1: *relation between contact angle and concentration of SiO_2*

example	concentration of TiO_2 mol	concentration of SiO_2 mol	Ratio of SiO_2/TiO_2	CA of Hexane (±1°)	CA of Terranova (±1°)
1	0.15	0	0	157.7	154
2	0.15	0.001	0.005	165.3	162
3	0.15	0.002	0.01	173.2	170.8
4	0.15	0.003	0.02	171.0	167.5
5	0.15	0.004	0.03	168	164.1
6	0.15	0.008	0.05	158	156.2
7	0.15	0.012	0.09	151.1	148.3
8	0.15	0.016	0.11	146.3	143.2
9	0.15	0.033	0.22	142.2	139.2
10	0.15	0.05	0.33	136.4	133.5

From the figure it can be observed that we have the highest CA for both Hexane and Terranova in 1% (percentage of SiO_2/percentage of TiO_2=0.01) concentration of SiO_2 (it equals 0.004 gr SiO_2 in our solution). After three times measuring the CA, the average results for the highest CA for solvent hexane was 173.2° and for Terranova was 170.8°. This experiment showed us to find the right amount of Silica that gives the highest hydrophilicity.

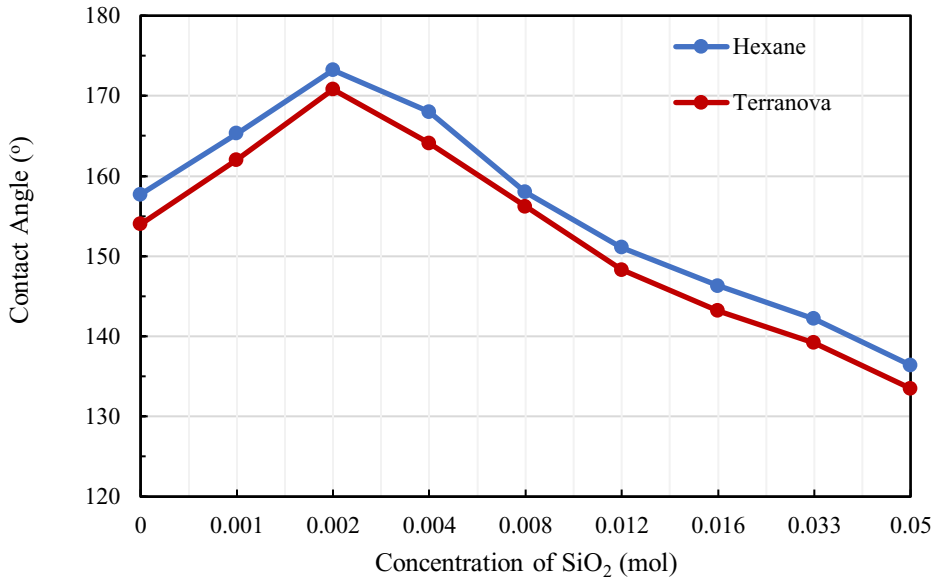

Figure 26: *relation between contact angle and concentration of SiO_2.*

To find the best mesh pure size and Sintering temperature, we measured the contact angle of mesh once, irrespective of the SiO_2 concentration and mesh pore size, then for different pore sizes. The results of these experiments are shown in Table 2, Figure 27 and Figure 28.

Table 2: *Relation between CA Vs. temperature and mesh size*

Mesh Size	Temperature 800°C		Temperature 650°C		Temperature 500°C	
	CA of Hexane	CA of Terranova	CA of Hexane	CA of Terranova	CA of Hexane	CA of Terranova
400	173.0	172.1	163.1	161.0	152.0	151.5
200	168.3	170.0	159.3	157.0	149.0	147.0
120	152.0	165.0	153.5	150.9	143.0	139.5
80	150.0	153.2	144.7	145.8	132.5	136.4

The best sintering conditions for producing relatively dense and homogeneous coatings were found to be sintering temperature of 800°C and dwelling time of 1 h. Figure 27 shows the amount of CA for mesh samples sintered in 500, 650 and 800 °C for 1hr dwelling time. We can observe from the graph that by increasing the temperature, the CA for both Hexane and Terranova will increase, that we have the highest amount at 800 ◦C. It needs to be mentioned that by increasing the temperature higher than 800 ◦C, our samples get burned, so the optimum best temperature is found at 800◦C. Keeping in mind that TiO2 has the crystalline structure that effects its hydrophilicty character. Rutile and Anatase are two main mineralogical types of titanium Oxide. The phase transition from anatase to rutile happens in a temperature range of 600-800 °C and that rutile bears the hydrophilicity phase of TiO2. In this work, amorphous TiO_2/SiO_2 coatings were converted into the crystalline phase by sintering at 800 °C. More descriptions at section 4.2.3.

Likewise, the CA has a direct relation with mesh pore size; in our experiment, we tried four different mesh counts (400, 200,120 and 80), and we found the best result with a mesh count 400 shows this relation in the graph. From these experiments, the highest contact angle achieved

was 173.2 and 170.8 for Hexane and Terranova (Figure 29), with 1% concentration of SiO_2 on mesh 400 and 800 ◦C sintering temperature, as shown in Figure 28. This proves that the TiO2-coated mesh's water-spreading rate rose as pore size decreased, making it possible to choose an appropriate pore size to accomplish superwetting (Figure 29). The mesh pore size of 45µm produced the largest spreading rate (superwetting) and the highest oil contact angle underwater because mesh hydrophilicity, underwater oleophobicity, and spreading rate all decreased with decreasing mesh pore size.

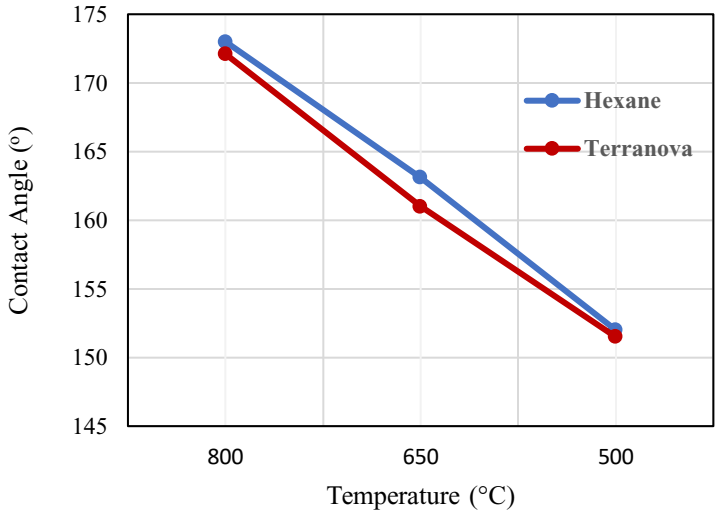

Figure 27: *The CA of mesh 400 sintered at different temperatures.*

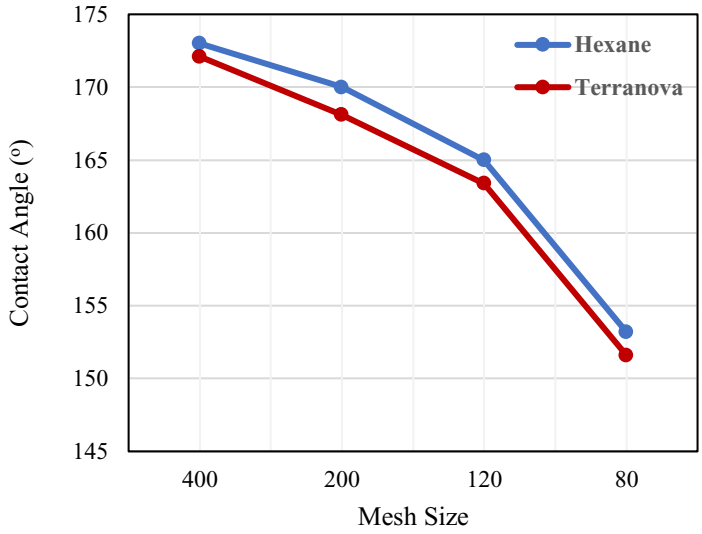

Figure 28: *The CA of different mesh size sintered in 800℃.*

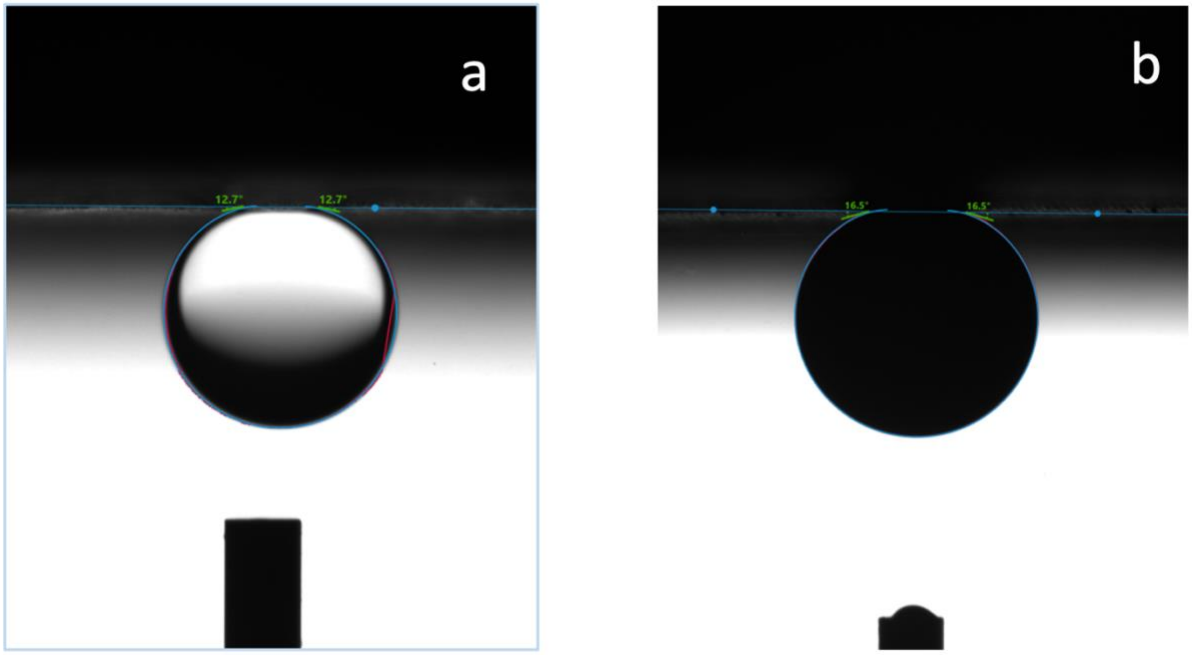

Figure 29: *a) The underwater contact angle of Hexane and b) the underwater contact angle of Terranova, on SS mesh 400, coated with TiO_2 and 1% SiO_2 concentration, sintered at 800℃ .*

4.1.2 Mesh Chemical Stability Test

After the coated mesh has been exposed to a harsh environment for an extended period, OCA measurements may be used to evaluate the stability of the coated SS mesh against chemicals. Table 3 shows the static contact angle findings for the SS mesh coated with solution after samples were aged for thirty days in seawater, 0.1 M acid (H_2SO_4) and 0.1 M alkaline (NaOH) solutions. The contact angle measurements shown in Table 3, are the mean of five mesh samples that were used as replicates; three drops were applied to each mesh sample. The $CA_{Hexzane}$ = 177.2 ° and $CA_{Terranova}$= 173.5 °, before ageing in the seawater, acid, and alkaline solutions.

Table 3: *Chemical stability test results for a period of 30 days.*

Solutions	10 days		20 days		30 days	
	CA of Hexane	**CA of Terranova**	**CA of Hexane**	**CA of Terranova**	**CA of Hexane**	**CA of Terranova**
NaOH 0.1 M	164.7	164.0	162.1	161.0	161.4	158.3
H2SO4 0.1 M	168.8	169.1	159.3	157.0	158.8	153.6
Seawater (PH=7.41)	163.6	162.8	158.5	154.9	154.4	151.2

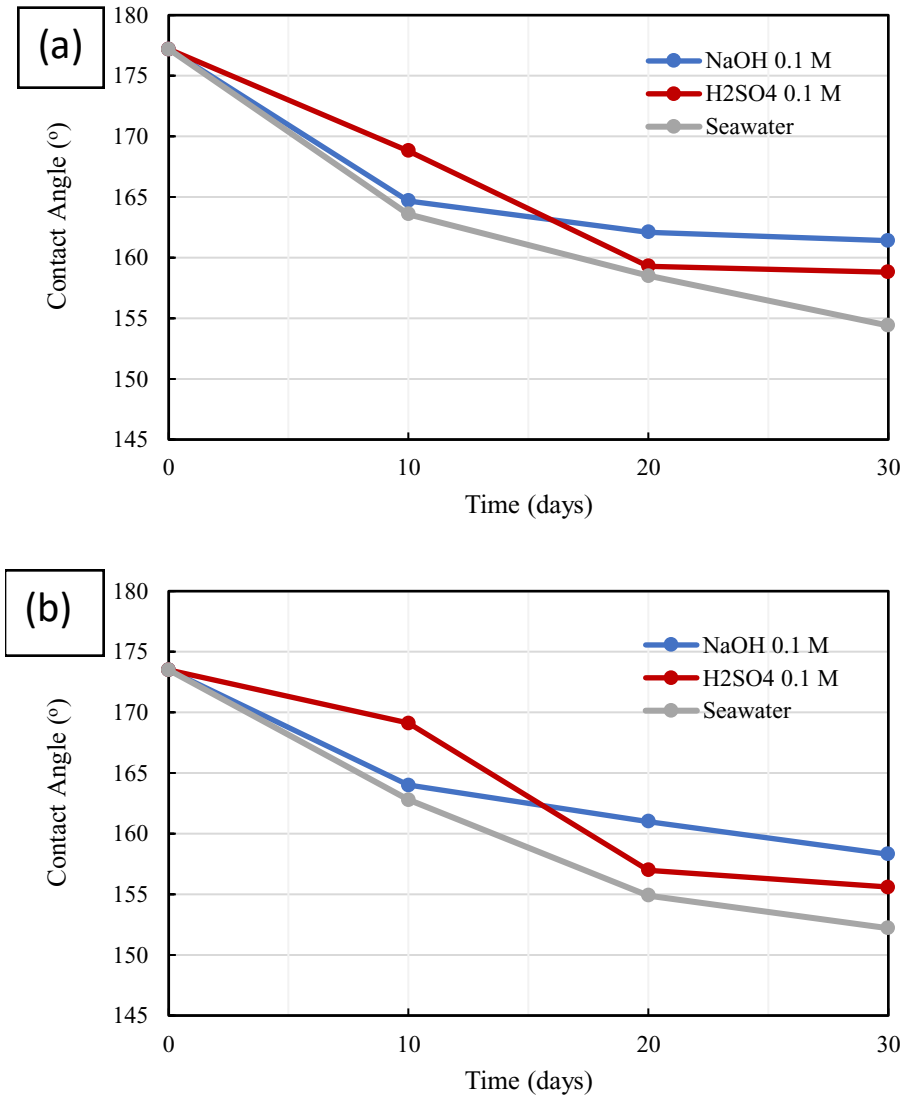

Figure 30: *Chemical stability analysis through CA measurements for a) Hexane and b) Terranova. The SS mesh samples are aged at room temperature in H2SO4 (0.1 M, shown in orange), NaOH (0.1 M, shown in blue), and seawater (1 M, shown in gray) solutions over thirty days.*

It can be observed from Figure 30, after 10 days the CA is still higher than 160 ° for all samples and the most significant drop was for the mesh aged in seawater (CA_{hexane} = 163.6° and

$CA_{Terranova}$ = 162.8°). The samples in the alkaline (0.1 NaOH) had their main drop in the first 10 days, and after that, the CA angles slightly changed. At the same time, the sudden CA changes for the samples in the Acid solutions happened between days 10-20. For the samples kept in the seawater, the CA declines with a constant slope during thirty days. Although it was the most significant drop between all the samples over a month.

4.1.3 Surface Energy

Surface energy is calculated by the OWRK method (equations 8 and 9). For this approach, the surface energy is measured using at least two liquids with known polar and dispersive surface tension components. Here, three liquids are selected: water, formamide, and ethylene glycol.

The various liquids employed for the surface energy study are displayed in Table 4.

Table 4: *The surface energy of the liquids employed in the study*

Liquids	Chemical Formula	Surface Tension (Dispersive) γ_{dS} (mN/m)	Surface Tension (Polar) γ_{pS} (mN/m)	Total Surface Tension γ_S (mN/m)	References for Values
Water	H2O	29.10	43.70	72.80	[99,114]
Ethylene Glycol	(CH 2OH) 2	26.40	21.30	47.70	[99,114]
Dimethylformamide	C3H7NO	25.21	11.29	36.5	[115]

The contact angle of Dimethylformamide and Ethylene Glycol are shown in the Figure 31, respectively. The Contact angle of water is zero.

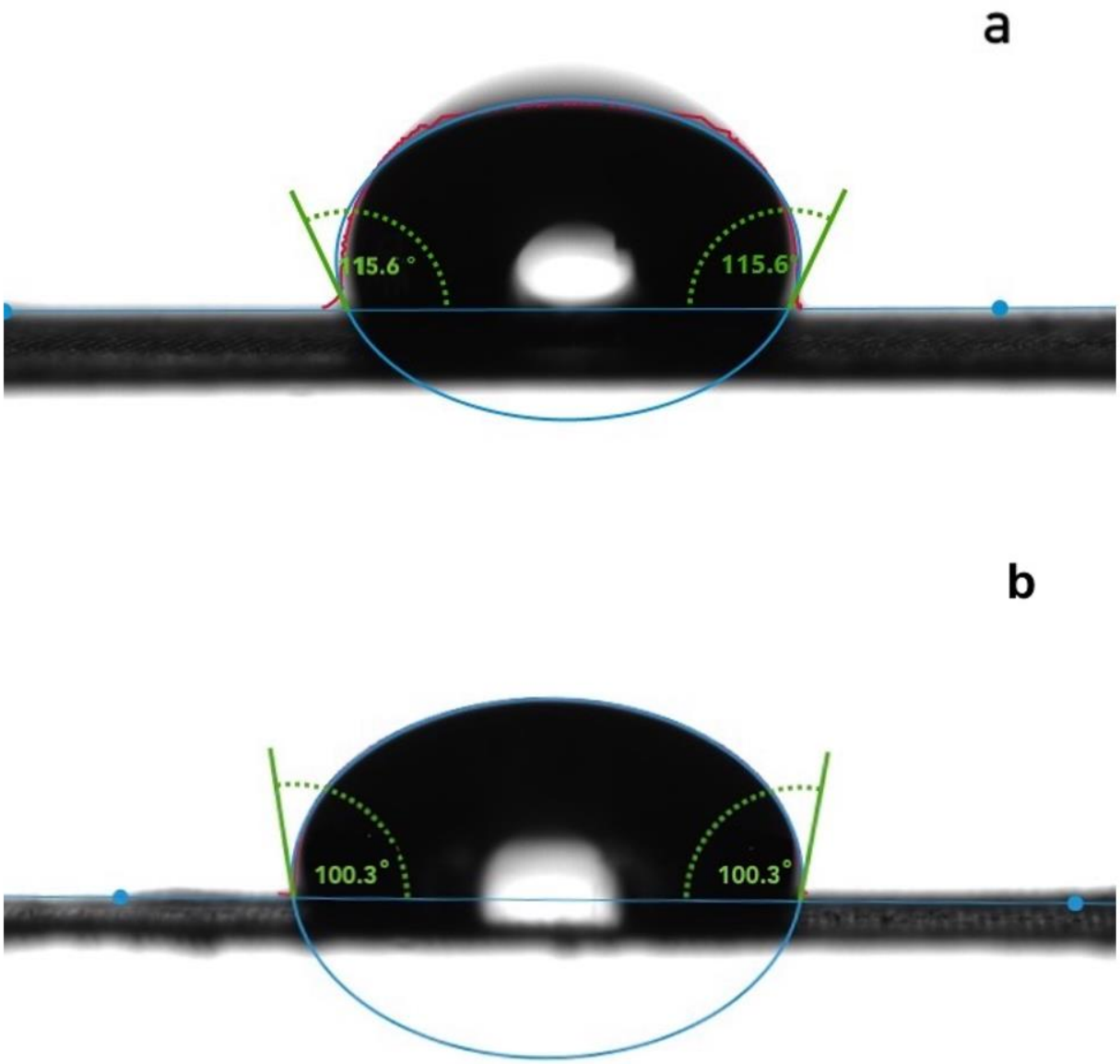

Figure 31: *a) Contact angle of Dimethylformamide, b) Contact angle of Ethylene Glycol.*

The surface energy plots of all the manufactured samples fitted with the OWRK model are presented in Figure 21.

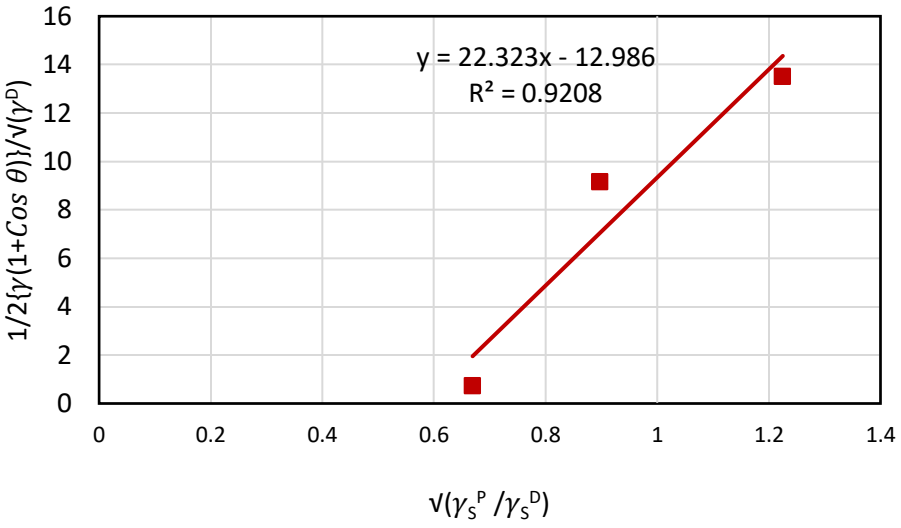

***Figure 32**: Surface energy calculation graph using OWRK method for the hybrid coating.*

The calculated surface energy values, base on equation 9, are displayed in Table 5.

***Table 5:** Surface energy results for the nanoscale hybrid coatings.*

Water Contact Angle (°)	Ethylene Glycol Contact Angle (°)	Dimethylformamide Contact Angle (°)	Surface Tension (Polar) (mN/m)	Surface Tension (Dispersive) (mN/m)	Surface Energy (mN/m)	Convergence
0	100.3±1	115.6±1	22.323	12.986	35.31	0.9208

The coating's surface energy is determined to be 35.31 mN/m. The wetness of the surface affects surface energy. When the solid surface's total surface energy is reduced, wettability decreases.

4.2 Surface Characterization Analysis

4.2.1 Scanning Electron Microscopy (SEM)

SEM images have been used to visualize the SS mesh morphology. Figure 33(a), (b) and (c) are taken for characteristics of mesh 400 before and after coating in TiO_2 and 1% SiO_2 coating solutions on mesh 400 with a sintering temperature of 800°C at three 70X,500X and 22000x magnification, respectively.

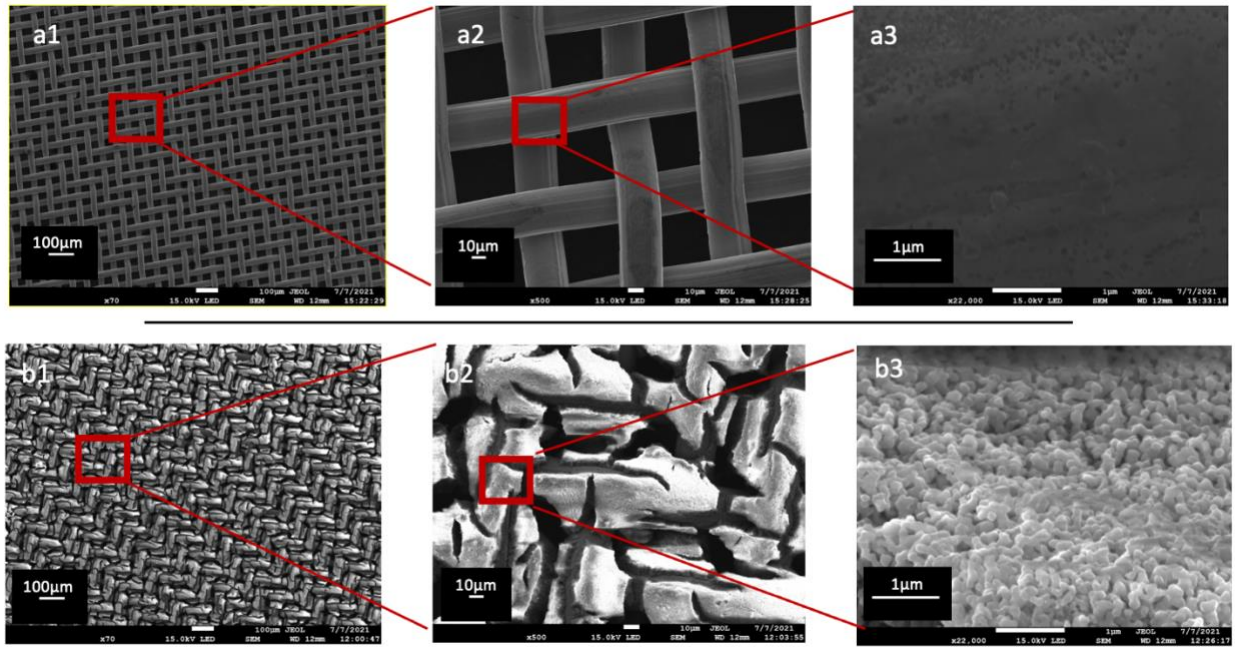

Figure 33: *SEM images of mesh 400 cleaned without coating at a1) 70x magnification (bar scale 200µm), a2) 500x magnification (bar scale 10µm) and a3) 22,000x magnification (bar scale 1µm) and mesh 400 after coating with TiO_2 and 1% SiO_2 solutions and sintering temperature of 800°C at b1) 70x magnification (bar scale 200µm), b2) 500x magnification (bar scale 10µm) and b3) 22,000x magnification (bar scale 1µm)*

From pictures taken in 70x and 500x magnification, we understand that even though the mesh pores have been filled with the coating solution, the arrangement of the ss mesh wires can still be noticed. Comparing two images that were taken on 500x magnification shows that mesh pores have been filled with the coating solution. However, there are some cracks and open areas which they are big enough to absorb the water and let the water droplets pass the mesh. Because of the superoleophobicity characteristics of the coating surfaces, the oil droplets are not passing through these pores. The images in 22,000x magnification show that the surface roughness will be increased after coating, and it helps the hydrophilicity and oleophobicity of the prepared meshes. These findings suggest that, like the self-cleaning lotus leaf, the produced coated mesh film has a rough surface with both micro- and nanoscale features.

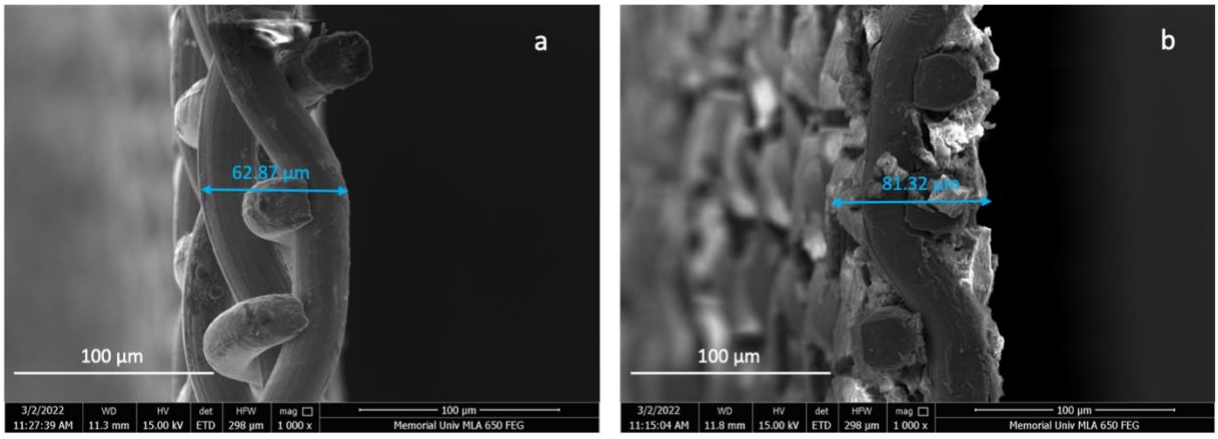

Figure 34: *SEM images from the side of mesh 400 a) before and b) after coating with TiO_2 and 1% SiO_2, both meshes are sintered at 800° C.*

Figure 34 shows the thickness of SS mesh 400 before and after coating. In this case, the SEM images are taken from the side of meshes. The thickness of sintered non-coated mesh is 62.87 µm (Figure 34, a); this amount is acquired by averaging the 5 points and the thickness of

the coated mesh reaches 81.32 μm (Figure 34, b). Accordingly, the coating thickness is 18.45 μm for the solution TiO_2 + 1% SiO_2.

Figure 35 shows the SEM images taken at 500x magnification (bar scale 200μm) from mesh 400, 200,120 and 80 before and after coating with the TiO_2 and 1% SiO_2 solution, sintered at 800^o C. It can be observed from Figure 35 that by increasing the mesh count, the size of the opening will decrease. Both for meshes before coating and after coating, it has a direct relation with the OCA. As observed in Figure 28, the coating shown in Figure 35 (e) gives the maximum OCA (mesh 400). So, by decreasing the opening size, we have a bigger CA. The approximate opening size for mesh 400 before coating is 1.38 e3 μm^2 decreasing to 2.02 e^2 μm^2 after coating. No coating materials exist in the pores of the mesh, which helps free air passage through the prepared coating mesh film.

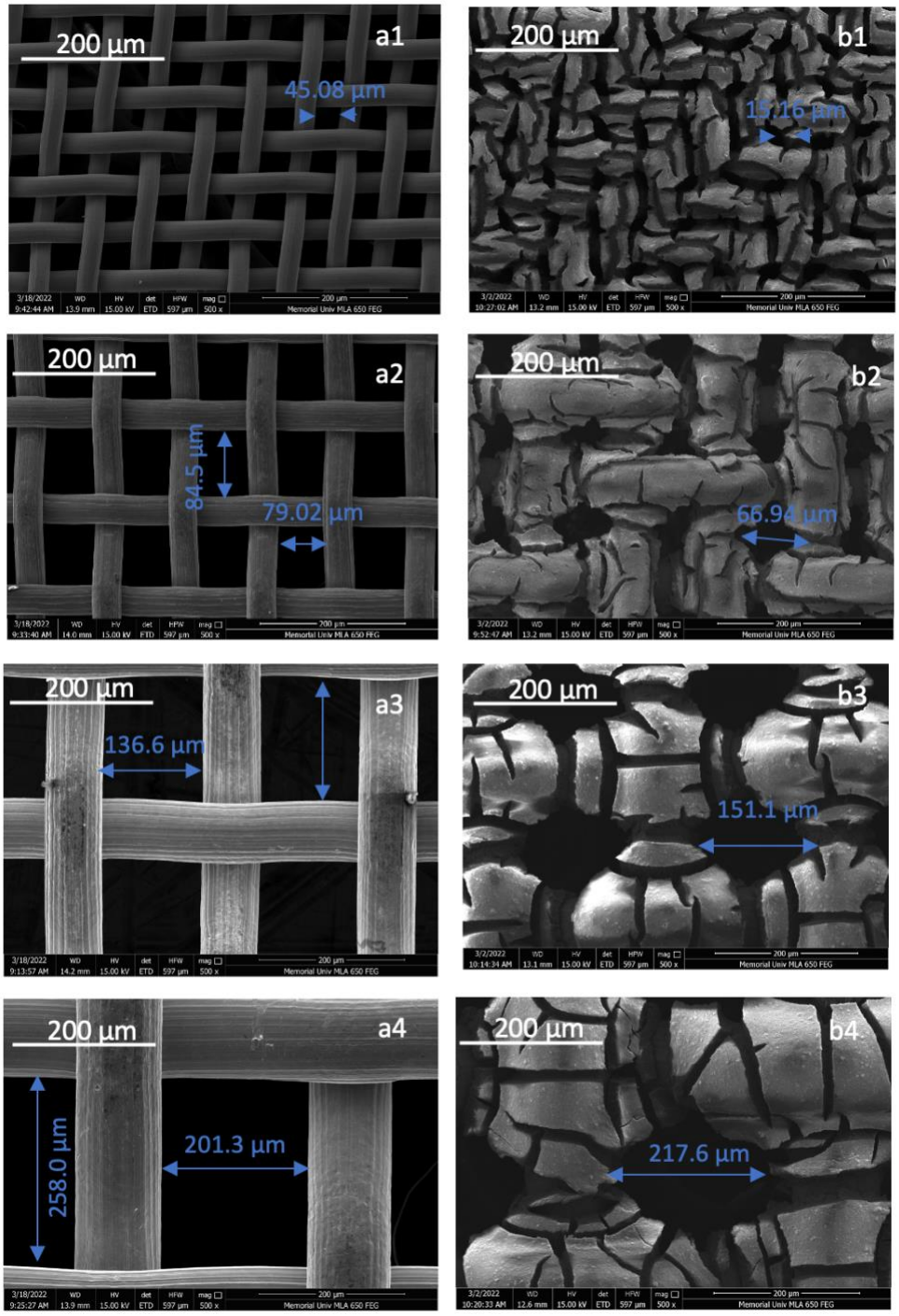

Figure 35: *SEM images at 500X magnification; bar scale 200µm of a1)mesh 400, a2)mesh 200, a3)mesh 120 and a4)mesh 80 before coating and b1)mesh 400, b2)mesh 200, b3)mesh 120 and b4)mesh 80 after coating with* TiO_2 *and 1%* SiO_2 *and sintered at 800°C.*

Figure 36 shows the SEM images of mesh 400 coated with TiO_2 and SiO_2 solution at 500X magnification taken at different sintering temperatures (Room temperature, 500, 650 and 800^o C) to show the effects of temperature on the sintered mesh. Based on Table 2, the highest CA was for mesh sintered at 800^o C (*Figure 36*, d), and by decreasing the temperature, the CA will fall, too. From Figure 36, by increasing the temperature, the liquid part of the solution is vaporing (Acetylacetone), and the shape and structure of the SS mesh appear. As a result, the material cannot be washed by water, and the coating will be more stable and durable during the oil-water separation test [116].

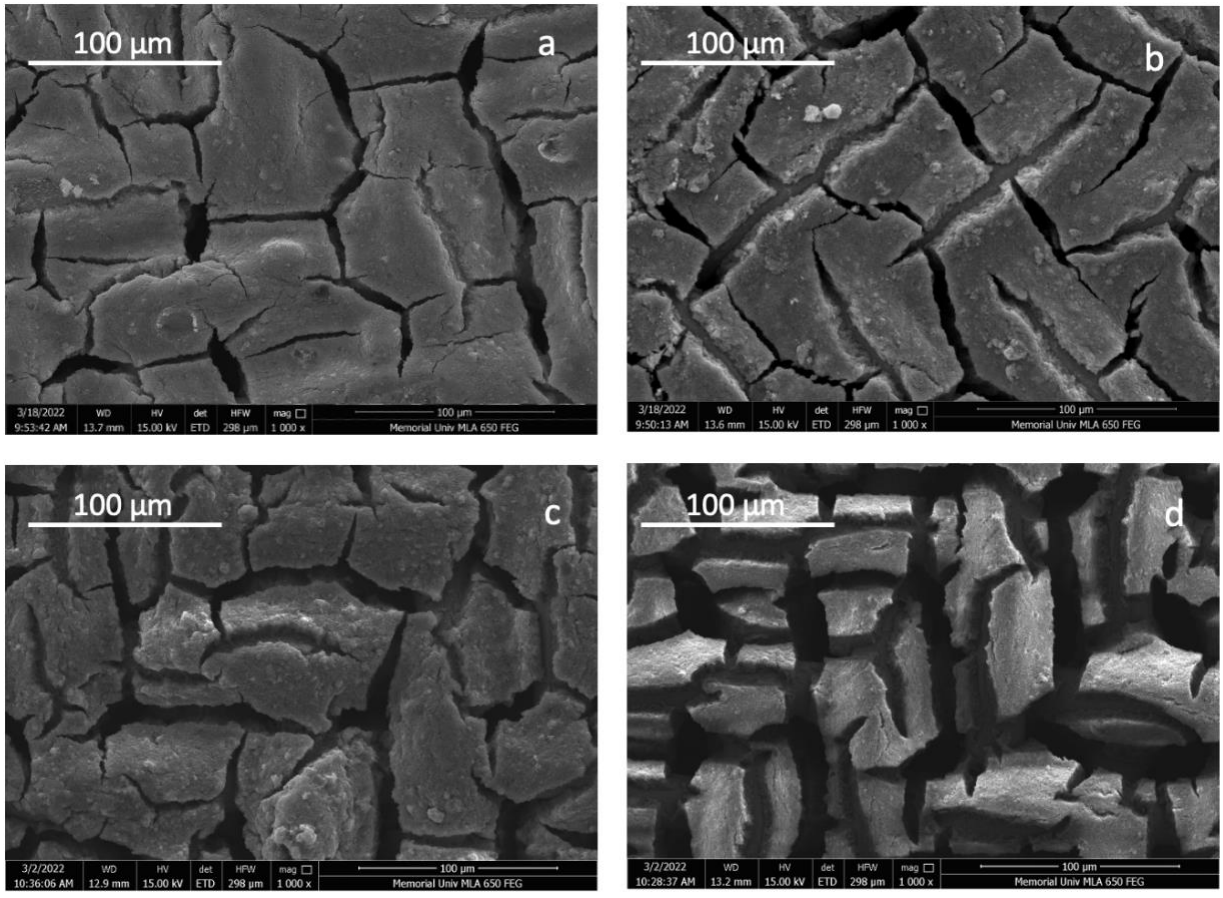

Figure 36: *SEM images at 500X magnification; bar scale 200µm of mesh 400 coated with TiO_2 and 1% SiO_2 and sintered at a) room temperature b) 500^{o}C c)650^{o}C and d) 800^{o}C.*

The effects of SiO_2 nano-powders in a coating solution shown with SEM images (Figure 37, a,b and c) following three solutions: TiO_2, TiO_2 + 1% SiO_2 and TiO_2 + 2% SiO_2 respectively. All samples are coated on mesh 400 and sintered at 800 ^oC.

In Figure 37, we can observe that the pure spaces between mesh wires are filled to a reasonable extent by increasing the concentration of SiO_2. The differences of the mesh prepared with 1% and 2% SiO_2 are insignificant as the CA results for these two types of mesh are very close (≈3^o differences). Likewise, the structure of the SS mesh is recognizable by increasing the concentration of the SiO_2.

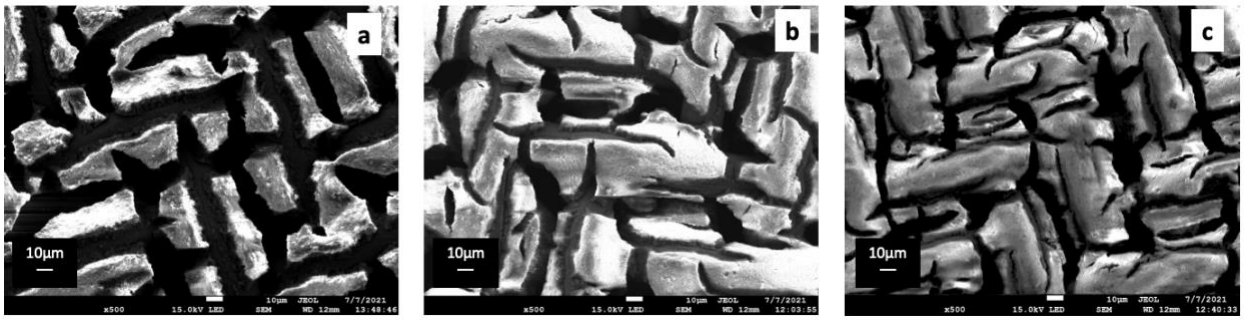

Figure 37: *SEM results of mesh 400 coated at a) TiO_2, b) TiO_2 + 1% SiO_2 and c) TiO_2 + 2% SiO_2 solutions sintered at 800 ^oC.*

4.2.2 Energy Dispersive X-Ray (EDX):

In Figure 38, we show the EDX analysis of the mesh coated with TiO_2 and 1% SiO_2 formulation. The weight percent of the elements and atom percentage are also reported in Table 6; the highest detected element counts, and X-ray energy belongs to Ti, with 53.01 wt% of the detected sample area at an energy level of 4.5 keV. For the EDX analysis, we choose an area of interest on the coated mesh wires and dismiss the empty mesh area with no coating. It is clear that the TiO_2 deposition was successful and achieved self-cleaning ability by the presence of

extra signals of the Ti element on the EDX spectra of the TiO_2/SiO_2 SS coated meshes, allowing the oily contamination to be photodegraded to restore super wetting surfaces [25].

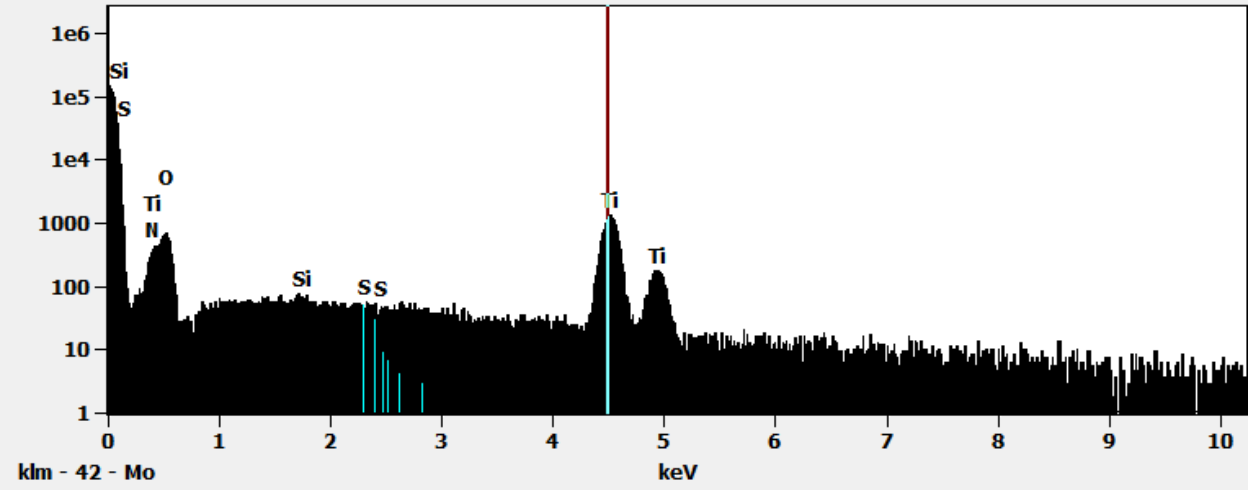

Figure 38: *EDX analysis of the SS mesh coated with TiO_2 and 1% SiO_2 Sintered at 800°C*

Table 6: *EDX analysis of Figure 38*

Atom	wt%	Atom %
O	53.02	77.10
Si	0.21	0.17
S	0.01	0.00
Ti	46.78	22.72

4.2.3 X-Ray Diffraction (XRD):

The anatase- and rutile-crystal structures are the most prevalent types of the prototypical photocatalyst TiO2 [25]. Considering that the phase transition from anatase to rutile occurs in a temperature range of 600–800 °C and that rutile carries the hydrophilicity phase of TiO_2,

amorphous TiO_2/SiO_2 coatings were transformed into the crystalline phase by sintering at 800 °C in this study.

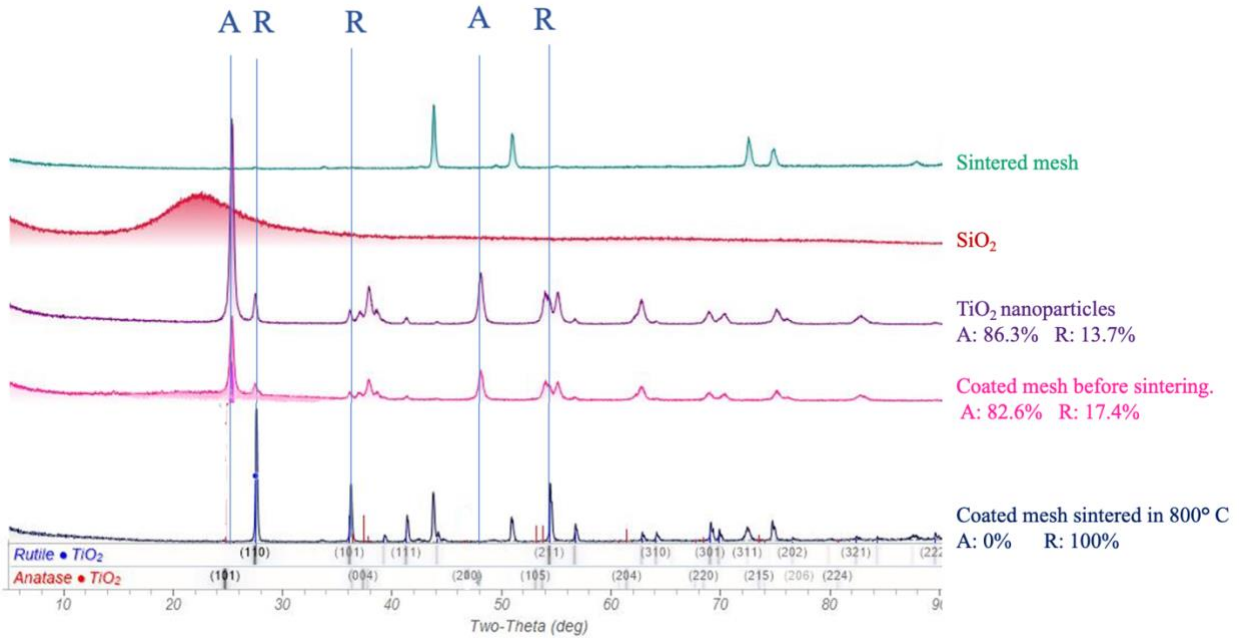

Figure 39: *XRD result for sintered mesh (green diagram), SiO_2 nano-powders (red diagram), TiO_2 nano particles (purple diagram), coated mesh with TiO_2 and 1% SiO_2 before sintering (pink diagram), and mesh 400 coated with TiO_2 and 1% SiO_2 sintered at 800 ^oC (blue diagram).*

Figure 39 shows the respective XRD pattern of the sintered mesh, SiO_2 powders, TiO_2 powders, coated mesh with TiO_2 and 1% SiO_2 before sintering and coated mesh with TiO_2 and 1% SiO_2 sintered in 800 ^oC. SiO_2 powders have an amorphous structure, so the calculated pattern was composed of a disordered single dominant X-ray amorphous halo (the red one) at about 23°2θ. This amorphous halo can still be recognized on coated mesh before the sintering graph (the pink one). But after sintering, all the amorphous structures transformed into the crystalline phase.

As mentioned before, to have a hydrophilic characteristic, the anatase phase of the TiO_2 should be transformed into the rutile phase. In this study, the anatase was marked by two strong diffraction peaks at 25.5° (101) and 48.0° (200), with a total amount of 86.3% for TiO_2 nanoparticles. This amount decreased to 82.6% on a mesh before sintering. While after sintering the coated mesh at 800 °C, all the anatase have been transformed into the main tree peak of the rutile at 27.8° (110), 36.1° (101) and 54.2° (211), indicative of the successful phase transformation.

To check why the 800 °C have decided as a sintering temperature for current research, the measured XRD results for mesh before sintering and sintered at 500 °C, 650 °C and 800 °C on mesh 400 are shown in Figure 40.

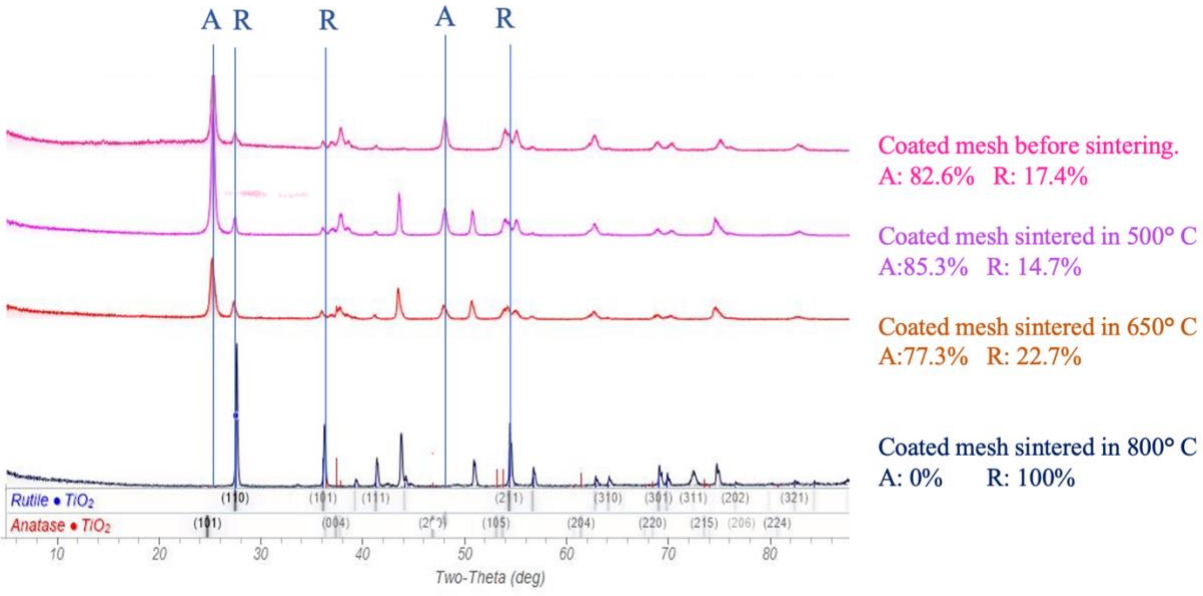

Figure 40: *results for mesh 400 coated with TiO2 and 1%. SiO2 before Sintering (pink diagram), sintered at 500 °C (purple diagram), 650 °C (orange diagram), and 800 °C (blue diagram).*

From Figure 40, it can be observed that only at 800 °C all the anatase have converted to the rutile phase. In contrast, the rutile amount is only 22.7 % at 650 °C and 14.7 % at 500 °C. The rutile diffraction peaks are shown at 27.8° (110), 36.1° (101) and 54.2° (211).

The effects of SiO_2 concentration in the coating solution are investigated with the XRD test and are shown in Figure 41. For this test, three samples were prepared on mesh 400 and coated in three samples with different concentrations of SiO_2 (1%, 2% and without SiO_2); all samples were prepared at a sintering temperature of 800 ºC.

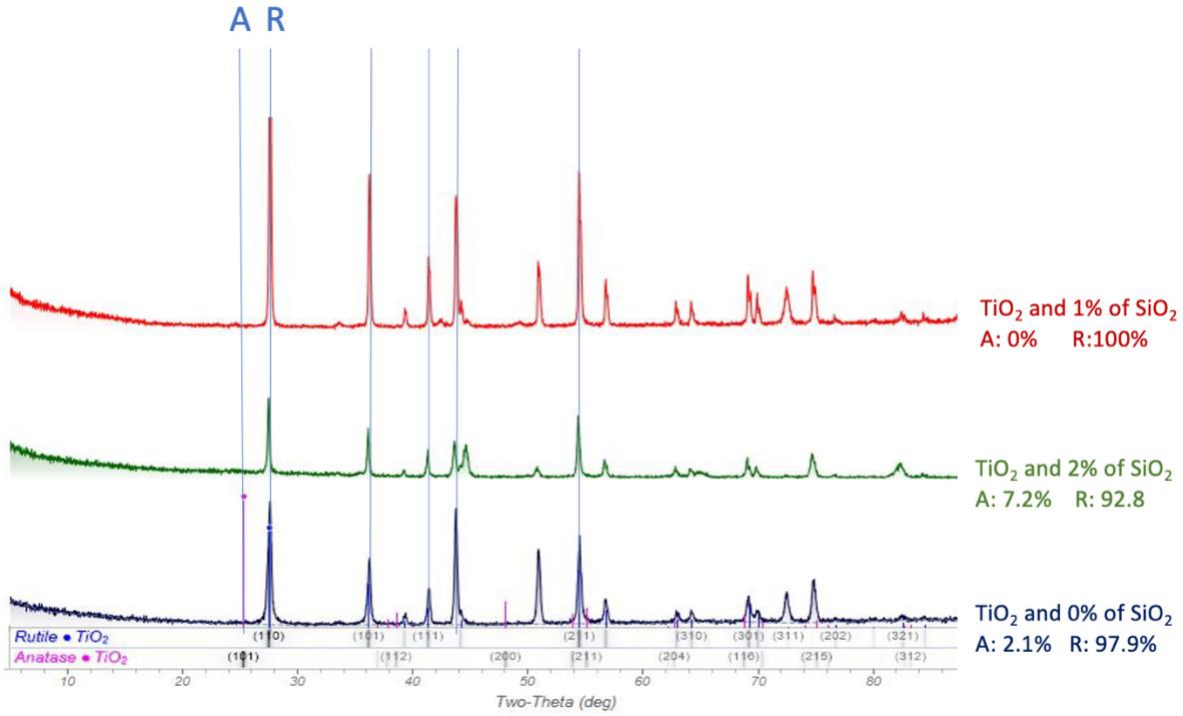

Figure 41: *XRD results of mesh 400, sintered at 800 ^{0}C and coated in a solution without SiO_2 (blue diagram), 1% SiO_2 (green diagram).*

From Figure 41, it identified that only with a 1% concentration of SiO_2, we have the highest amount of rutile (red diagram, rutile=100%). These data also prove the CA results we deliberated in section 4.1.1.

4.3 Oil-Water Separation Test

The oil-water separation is conducted according to the process flow diagram shown in Figure 22. The following experiments identified the efficiency of the process. All the experiments were done by mesh 400, coated in TiO_2 and 1% SiO_2 solution and sintered in 800 ^oC. Figure 42 shows oil-water samples before and after passing through the prepared mesh.

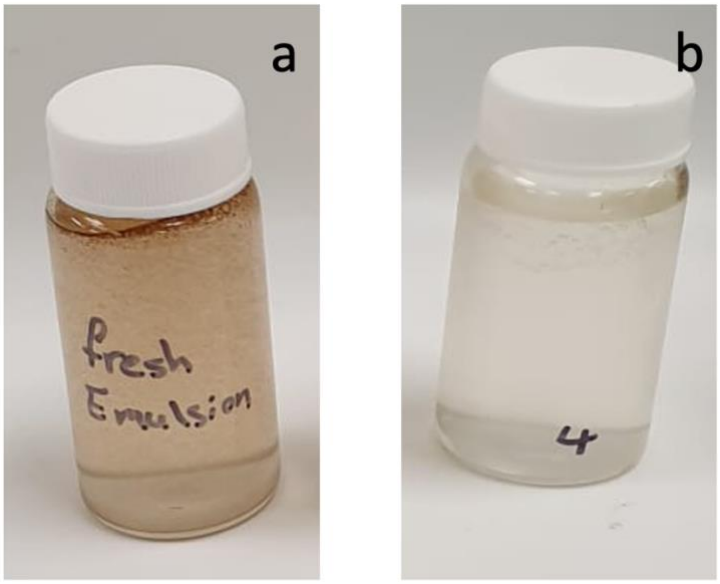

Figure 42: *optical photos of the a) oil-water mixture (Fresh emulsion) and b) collected water after passing through the coated mesh.*

4.3.1 Water Permeating Flux Rate and Intrusion Pressure

Water flux is an evaluation of the oil/water separation ability of the mesh. The water flux (F) was measured under a fixed column of water and the data resulted from five times repeated experiments. The values were calculated using equation (14). In this experiment, we fixed V to 0.4 L. The area of the mesh that water passes through is 2.54×10^{-4}. The average required time for the permeation of 0.4 L water after five times for non-coated and coated mesh is 62 S and 79 S, respectively. So, the flux rate for non-coated mesh is 25.40 $L.m^{-2}.S^{-1}$ and for coated mesh is 19.94 $L.m^{-2}.S^{-1}$.

Oil intrusion pressure (P) is determined from equation (15) by the maximum height (h_{max}) of the water column that the coated meshes can bear. The maximum bearable height achieved for SS coated mesh was 39.0 cm Figure 43. Thus, the water intrusion pressure for the coated meshes was 3.12 kPa. It is worth mentioning that 39.0 cm is not the maximum height; this is the maximum amount we could examine with our facilities.

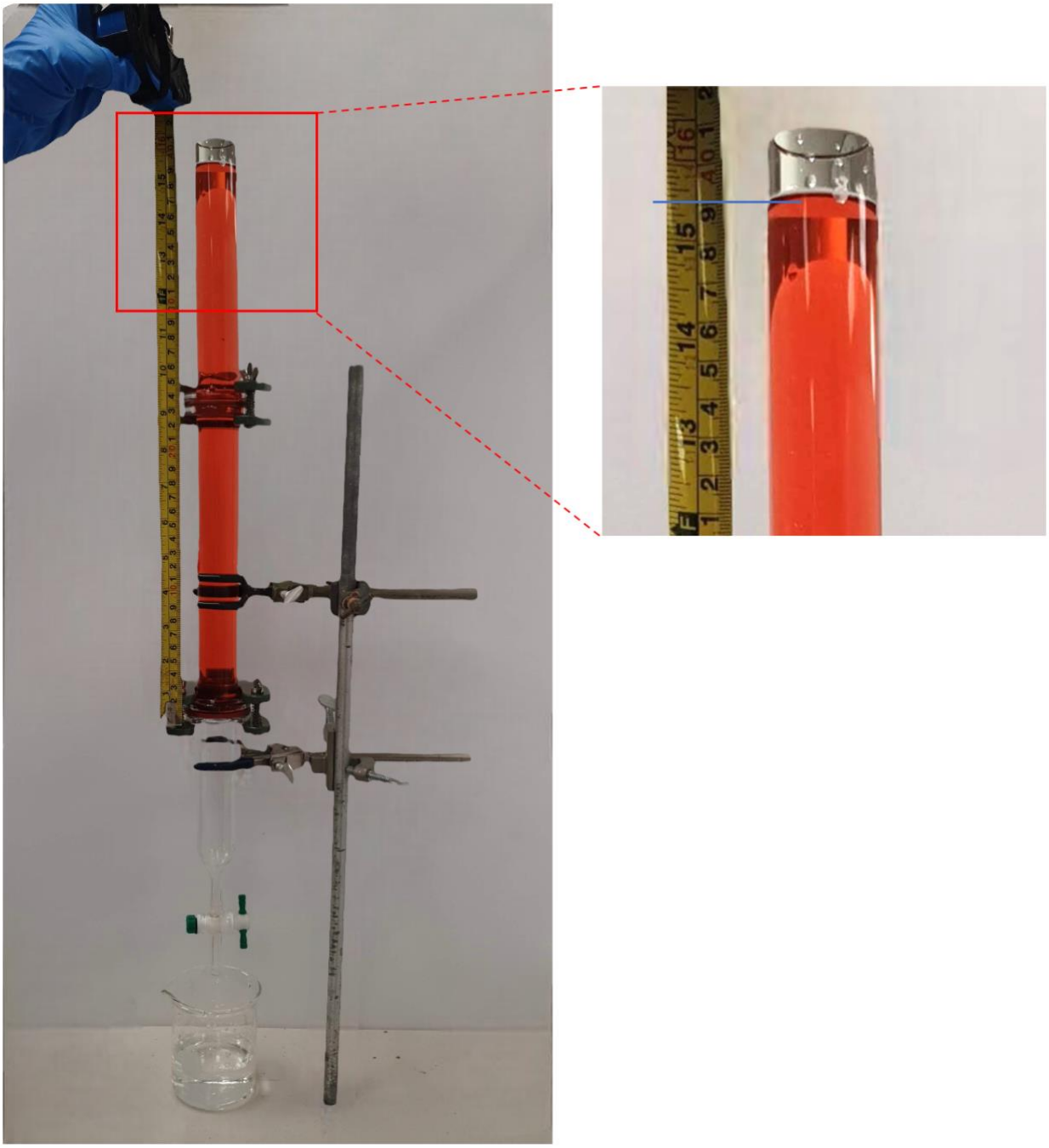

Figure 43: *Water intrusion pressure of the TiO_2+1% SiO_2 coated meshes (oil mixture is dyed with phenol red)*

4.3.2 Filtration Performance by UV-Vis and Fluoresces Tests

We recorded the absorbance at three distinct wavelengths of 340, 370, and 400 nm using a recording spectrophotometer that can detect absorbance at multiple wavelengths. Then we used the trapezoidal method to determine the area under the absorbance vs. wavelength curve using the equation (10). These results are gathered in Table 7, and the calibration curve by multi-wavelength 340, 370 and 400 nm is shown in Figure 44.

Table 7: *Calculated area by the absorbances at three discreet wavelengths of 340, 370, and 400 nm.*

Oil concentration (ppm)	Wavelengths (nm)			Area
	340	370	400	
960	0.447	0.233	0.145	15.87
720	0.326	0.169	0.105	11.535
480	0.226	0.116	0.072	7.95
336	0.151	0.078	0.049	5.34
240	0.111	0.057	0.036	3.915
144	0.076	0.039	0.025	2.685
96	0.052	0.026	0.017	1.815
48	0.03	0.014	0.009	1.005
24	0.019	0.008	0.005	0.6

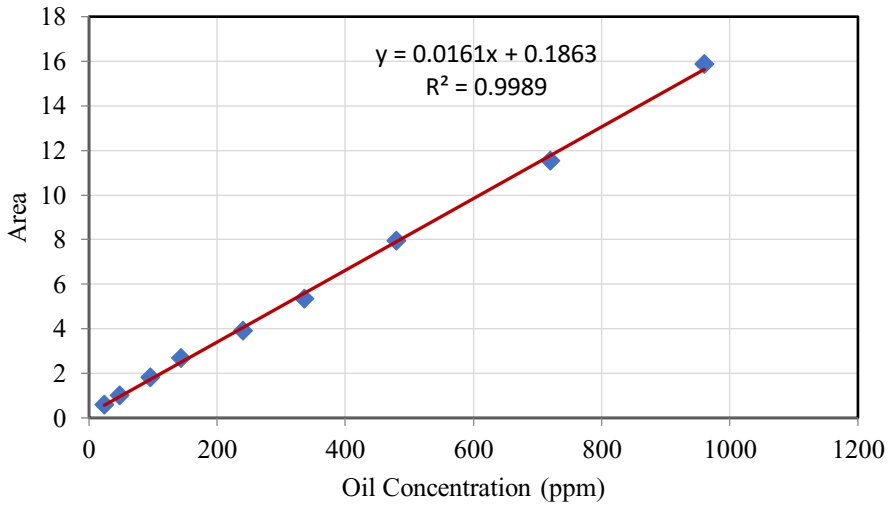

Figure 44: *Terranova calibration curve by multi-wavelength 340, 370, and 400 nm UV-Vis.*

Then the concentration of oil components was measured and calculated by UV-Vis before and after passing through the mesh (Table 8). The oil concentration in the emulsion (before departing the mesh) is 1011.75 ppm and the oil concentration after passing the coated mesh is 86.53 ppm. Therefore, the removal efficiency of multiwavelength (340,370,400 nm) UV-Vis calculated by equation 13, is 91.4%.

Table 8: *Concentration of oil before and after passing through the mesh by multi-wavelength 340,370 and 400 nm uv-vis test*

sample	Concentration of oil (ppm)
Emulsion	1011.757
Treated water	86.539

The Concentration of oil is also calculated by the UV-Vis mono-wavelength 260 nm. The data of this experiment are shown in Table 9 and Figure 45.

Table 9: *Calculated area by the absorbances at discreet mono wavelengths of 260nm.*

Oil concentration (ppm)	Wavelength (nm) 260	Area
280	2.75	2.58
252	2.51	2.34
224	2.28	2.11
196	2.03	1.86
168	1.79	1.62
140	1.48	1.31
112	1.245	1.075
84	0.98	0.81
56	0.709	0.539
28	0.444	0.274
14	0.31	0.14
7	0.24	0.07
0	0.17	0

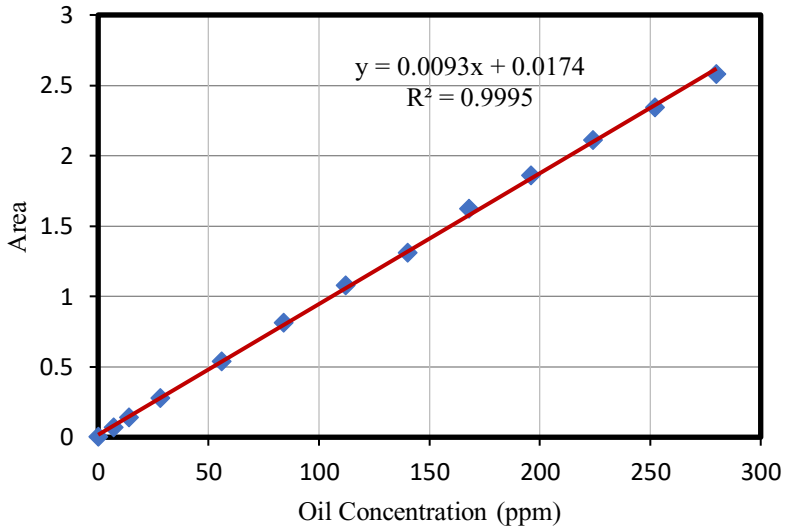

Figure 45: *Terranova calibration curve by monoi-wavelength 260 nm UV-Vis.*

The Concentration of oil in the samples before and after passing through the mesh were measured from mono-wavelength UV-Vis and shown in Table 10. The removal efficiency from equation 13, is 91.81%, almost the same as the results from the multi-wavelength test.

Table 10: *Concentration of oil before and after passing through the mesh by UV-Vis mono-wavelength 260 nm*

Sample	Concentration of oil (ppm)
Emulsion	1052.545
Treated water	86.20311

The separation efficiency of the TiO_2+1% SiO_2 mesh is also distinguished by the fluorescence emission light at 300 nm excitation wavelength (Figure 46). The Concentration of oil before and after passing the mesh are 1034.91 ppm and 91.89 ppm, respectively. So the oil-water separation efficiency is about 91.12% (Table 11).

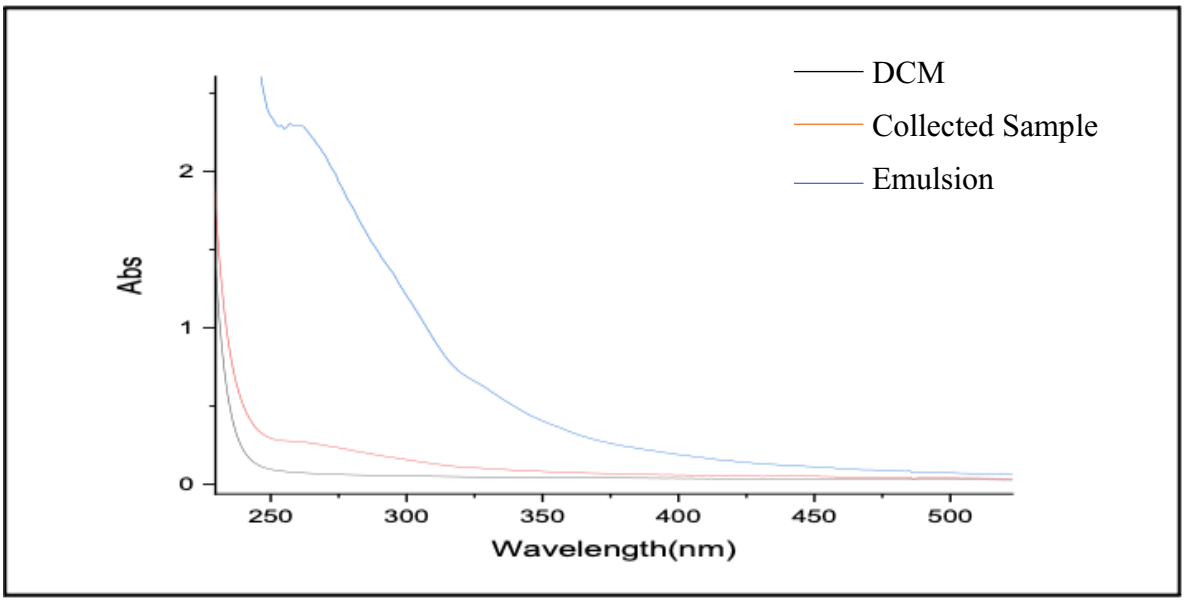

Figure 46: *Fluorescence intensity at 300 nm excitation wavelength as a function of oil concentration for DCM (DCM, purple), water mixture before (Emulsion, blue) and after passing through mesh (mesh, red)*

Table 11: *Concentration of oil before and after passing through the mesh by fluorescence intensity at 300 nm excitation wavelengths, the oil-water separation efficiency is 91% based on these three tests.*

Sample	Concentration of oil (ppm)
Emulsion	1034.91
Treated water	91.89

4.4 Summary

The superhydrophilicity and superoleophobicity character of the coated meshes is carried out in this chapter. First off, mesh wettability characterization was investigated. Contact angles,

mesh chemical durability, and surface energy was examined in this regard. Results of the contact angel tests reveal that the best mesh was prepared with the SS mesh 400, coated with TiO_2 and 1% SiO_2 and sintered in 800^oC with the underwater contact angel results of 173.0 and 172.0 for Hexane and Terranova, respectively.

In the second part, the surface characterization tests such as SEM, EDX and XRD have been studied. SEM micrographs and EDX tests confirmed the presence of the TiO_2 nanoparticles and showed the effects of SiO_2 on surface structure and roughness. XRD results approve that the best temperature for sintering would be 800^oC. Mesh size 400 showed better results than other meshes tested in this study.

The flow flux rate and oil permeating pressure were determined in Oil-water separation tests. The oil-water separation efficiency was assessed by single and multi-wavelength UV-vis and fluorescence tests. From all experiments, the effectiveness of the mesh after coating was 91%.

CHAPTER FIVE

5 Conclusions and Recommendations for Future Work

5.1 Conclusions

This study focuses on the fabrication of SS mesh and its application for oil-water separation purposes. The potential of the SS mesh tube as-fabricated for the separation of oil/water from an oil-water mixture is assessed using a cross-flow dynamic setup under various oil concentrations and total flow rate parameters. In addition, Characterization studies are also carried out to demonstrate how the surface evolves after coating. The three main chapters of this thesis include a review of the literature (2), the manufacture and preparation of SS mesh (Chapter 3), characterization and dynamic oil-water separation using a SS mesh tube (Chapter 4).

A superhydrophilic-superoleophobic stainless steel mesh-based membrane is fabricated to evaluate how well the membrane surface modification affects the efficiency of static oil-water separation. To create a membrane that is both superhydrophilic and superoleophobic, the clean meshes are activated by the electrodeposition method with three solution mixtures, first TiO_2, second TiO_2+ 1% SiO_2 and third TiO_2+ 2% SiO_2 solution to study the effect of silica. All these solutions are coated on SS meshes with four different opening sizes 80, 120, 200 and 400. Then prepared meshes are sintered at temperatures 500 ^oC, 650 ^oC and 800 ^oC.

Under this coating process, the surface energy and morphology of the membranes are modified simultaneously. The fabricated mesh is characterized by SEM, EDX, XRD, equilibrium

underwater OCA of Hexane and Terranova measurements, stability tests, and static oil-water separation analysis. The primary outcomes of this experimental research are as follows:

- Maximum OCA for hexane (173.2) and Terranova (170.8) was achieved for the mesh 400, coated with TiO_2+ 1% SiO_2 and sintered at 800 ^oC.
- The results from SEM and XRD tests confirm the superhydrophilicity and superoleophobicity of the coated mesh.
- According to the SEM images, the nano roughness offers an increased surface area with a useful oil repellent property. The apparent cracks on the extended surface also form areas with strong capillary pressure that positively pass through the water phase.
- Based on the XRD tests, by increasing the temperature, the superhydrophilicity character of the coated mesh is increasing. Only at 800 ^oC is the Anatase phase of the TiO_2 converted to the Rutile, which gives us the superhydrophilicity feature. Also, the results show that the highest amount of Rutile was achieved for the solution by a 1% concentration of SiO_2.
- The manufactured membranes exhibit remarkable stability after being immersed in seawater,0.1 M NaOH and 0.1 M H_2SO_4 solutions for 30 days.

All the experiments prove that the SS mesh 400 coated with TiO_2+ 1% SiO_2 and at 800^oC sintering temperature has the highest hydrophilicity and oleophobicity features.

The efficiency of fabricated stainless-steel mesh in continuous mode is examined in the last stage of this study for the varying total flow rates.

- Data from five times repeated tests were used to determine the water flow (F) beneath a fixed column of water. As a result, the flux rate for coated and non-coated mesh is 19.94 $L.m^{-2}.S^{-1}$ and 25.40 $L.m^{-2}.S^{-1,}$ respectively.
- Oil intrusion pressure (P) is determined as 3.12 kPa for the maximum height of 39.0 cm.
- The efficiency of the oil-water separation was calculated by the Uv-vis and fluorescence tests for the prepared emulsion. From these experiments, we have similar results in all experiments and the separation efficiency achieved after the mesh is 91%.
- Based on the durability tests, these meshes are reusable for at least five cycles and reusing these coated meshes also lowers the cost of treating oily effluent.

The membrane as-prepared shows a potential path for dealing with stratified oil/water mixes and emulsions, and this work offers an easy and universal method to create TiO2-decorated materials.

5.2 Recommendations for Future Work

The following suggestions for further work are made using the crossflow gravity-based setup for the dynamic oil-water separation using SS mesh tubes:

- Our experiments are based on lab-scale results tests. Doing the oil-water separation tests on a pool-scale are recommended.
- Further research can examine the impact of vacuum and oil droplet size on the dynamic oil-water separation process. As a result, a static mixer introduced into

the tube side and attached to a regulated vacuum can produce an oil-water combination.

- The impact of fouling on the functionality of the SS membranes is one of the elements that was not addressed in this study, but it can be in further studies.
- Using mathematics and modeling techniques like computational flow dynamics (CFD) and artificial neural networks, our system's momentum and mass transfer may be represented later. With efficient modeling/simulation techniques, a systematic parametric sensitivity analysis would be able to better design and operate the membrane toward optimal conditions.
- It is advised to evaluate the effects of various coating materials, particularly those with minimal environmental impact.

References

(1) Xue, Z.; Cao, Y.; Liu, N.; Feng, L.; Jiang, L. Special Wettable Materials for Oil/Water Separation. *J. Mater. Chem. A* **2014**, *2* (8), 2445–2460.

(2) Chu, Z.; Feng, Y.; Seeger, S. Oil/Water Separation with Selective Superantiwetting/Superwetting Surface Materials. *Angew. Chem. Int. Ed.* **2015**, *54* (8), 2328–2338.

(3) Li, P.; Cai, Q.; Lin, W.; Chen, B.; Zhang, B. Offshore Oil Spill Response Practices and Emerging Challenges. *Mar. Pollut. Bull.* **2016**, *110* (1), 6–27. https://doi.org/10.1016/j.marpolbul.2016.06.020.

(4) Gao, C.; Sun, Z.; Li, K.; Chen, Y.; Cao, Y.; Zhang, S.; Feng, L. Integrated Oil Separation and Water Purification by a Double-Layer TiO2-Based Mesh. *Energy Environ. Sci.* **2013**, *6* (4), 1147. https://doi.org/10.1039/c3ee23769a.

(5) Li, F.; Kong, W.; Zhao, X.; Pan, Y. Multifunctional TiO_2-Based Superoleophobic/Superhydrophilic Coating for Oil–Water Separation and Oil Purification. *ACS Appl. Mater. Interfaces* **2020**, *12* (15), 18074–18083. https://doi.org/10.1021/acsami.9b22625.

(6) You, Q.; Ran, G.; Wang, C.; Zhao, Y.; Song, Q. Facile Fabrication of Superhydrophilic and Underwater Superoleophobic Chitosan–Polyvinyl Alcohol-TiO2 Coated Copper Mesh for Efficient Oil/Water Separation. *J. Coat. Technol. Res.* **2018**, *15* (5), 1013–1023. https://doi.org/10.1007/s11998-017-0036-1.

(7) Ma, Q.; Cheng, H.; Fane, A. G.; Wang, R.; Zhang, H. Recent Development of Advanced Materials with Special Wettability for Selective Oil/Water Separation. *Small* **2016**, *12* (16), 2186–2202. https://doi.org/10.1002/smll.201503685.

(8) Gong, Z.; Yang, N.; Chen, Z.; Jiang, B.; Sun, Y.; Yang, X.; Zhang, L. Fabrication of Meshes with Inverse Wettability Based on the TiO2 Nanowires for Continuous Oil/Water Separation. *Chem. Eng. J.* **2020**, *380*, 122524. https://doi.org/10.1016/j.cej.2019.122524.

(9) Gunatilake, U. B.; Bandara, J. Efficient Removal of Oil from Oil Contaminated Water by Superhydrophilic and Underwater Superoleophobic Nano/Micro Structured TiO2 Nanofibers Coated Mesh. *Chemosphere* **2017**, *171*, 134–141. https://doi.org/10.1016/j.chemosphere.2016.12.031.

(10) Deng, W.; Li, C.; Pan, F.; Li, Y. Efficient Oil/Water Separation by a Durable Underwater Superoleophobic Mesh Membrane with TiO2 Coating via Biomineralization. *Sep. Purif. Technol.* **2019**, *222*, 35–44. https://doi.org/10.1016/j.seppur.2019.04.019.

(11) Drelich, J.; Chibowski, E.; Meng, D. D.; Terpilowski, K. Hydrophilic and Superhydrophilic Surfaces and Materials. *Soft Matter* **2011**, *7* (21), 9804–9828.

(12) Jo, S.; Kim, Y. Superhydrophilic–Underwater Superoleophobic TiO2-Coated Mesh for Separation of Oil from Oily Seawater/Wastewater. *Korean J. Chem. Eng.* **2016**, *33* (11), 3203–3206. https://doi.org/10.1007/s11814-016-0184-5.

(13) Zhou, X.; Yu, S.; Wang, J.; Zang, J.; Lv, Z. Superhydrophilic Anti-Corrosive and Superhydrophobic Durable TiO2/Ti Mesh for Oil/Water Separation. *J. Taiwan Inst. Chem. Eng.* **2019**, *105*, 124–133. https://doi.org/10.1016/j.jtice.2019.10.011.

(14) Yuan, S.; Chen, C.; Raza, A.; Song, R.; Zhang, T.-J.; Pehkonen, S. O.; Liang, B. Nanostructured TiO2/CuO Dual-Coated Copper Meshes with Superhydrophilic, Underwater Superoleophobic and Self-Cleaning Properties for Highly Efficient Oil/Water Separation. *Chem. Eng. J.* **2017**, *328*, 497–510. https://doi.org/10.1016/j.cej.2017.07.075.

(15) Yang, H.-C.; Liao, K.-J.; Huang, H.; Wu, Q.-Y.; Wan, L.-S.; Xu, Z.-K. Mussel-Inspired Modification of a Polymer Membrane for Ultra-High Water Permeability and Oil-in-Water Emulsion Separation. *J Mater Chem A* **2014**, *2* (26), 10225–10230. https://doi.org/10.1039/C4TA00143E.

(16) Jiang, Y.; Shi, K.; Tang, H.; Wang, Y. Enhanced Wettability and Wear Resistance on TiO2/PDA Thin Films Prepared by Sol-Gel Dip Coating. *Surf. Coat. Technol.* **2019**, *375*, 334–340. https://doi.org/10.1016/j.surfcoat.2019.07.051.

(17) Zuo, X.; Chang, K.; Zhao, J.; Xie, Z.; Tang, H.; Li, B.; Chang, Z. Bubble-Template-Assisted Synthesis of Hollow Fullerene-like MoS $_2$ Nanocages as a Lithium Ion Battery Anode Material. *J. Mater. Chem. A* **2016**, *4* (1), 51–58. https://doi.org/10.1039/C5TA06869J.

(18) You, Q.; Ran, G.; Wang, C.; Zhao, Y.; Song, Q. A Novel Superhydrophilic–Underwater Superoleophobic Zn-ZnO Electrodeposited Copper Mesh for Efficient Oil/Water Separation. *Sep. Purif. Technol.* **2018**, *193*, 21–28. https://doi.org/10.1016/j.seppur.2017.10.055.

(19) Huang, A.; Chen, L.-H.; Kan, C.-C.; Hsu, T.-Y.; Wu, S.-E.; Jana, K. K.; Tung, K.-L. Fabrication of Zinc Oxide Nanostructure Coated Membranes for Efficient Oil/Water

Separation. *J. Membr. Sci.* **2018**, *566*, 249–257. https://doi.org/10.1016/j.memsci.2018.09.007.

(20) Xiong, W.; Li, L.; Qiao, F.; Chen, J.; Chen, Z.; Zhou, X.; Hu, K.; Zhao, X.; Xie, Y. Air Superhydrophilic-Superoleophobic SiO2-Based Coatings for Recoverable Oil/Water Separation Mesh with High Flux and Mechanical Stability. *J. Colloid Interface Sci.* **2021**, *600*, 118–126. https://doi.org/10.1016/j.jcis.2021.05.004.

(21) Huang, T.; Zhang, L.; Chen, H.; Gao, C. Sol–Gel Fabrication of a Non-Laminated Graphene Oxide Membrane for Oil/Water Separation. *J. Mater. Chem. A* **2015**, *3* (38), 19517–19524. https://doi.org/10.1039/C5TA04471E.

(22) Topçu Kaya, A. S.; Cengiz, U. Fabrication and Application of Superhydrophilic Antifog Surface by Sol-Gel Method. *Prog. Org. Coat.* **2019**, *126*, 75–82. https://doi.org/10.1016/j.porgcoat.2018.10.021.

(23) Cordero-Arias, L.; Cabanas-Polo, S.; Gao, H.; Gilabert, J.; Sanchez, E.; Roether, J. A.; Schubert, D. W.; Virtanen, S.; Boccaccini, A. R. Electrophoretic Deposition of Nanostructured-TiO2/Chitosan Composite Coatings on Stainless Steel. *RSC Adv.* **2013**, *3* (28), 11247. https://doi.org/10.1039/c3ra40535d.

(24) Boccaccini, A. R.; Karapappas, P.; Marijuan, J. M.; Kaya, C. TiO $_2$ Coatings on Silicon Carbide and Carbon Fibre Substrates by Electrophoretic Deposition. *J. Mater. Sci.* **2004**, *39* (3), 851–859. https://doi.org/10.1023/B:JMSC.0000012914.47793.3e.

(25) Yuan, S.; Chen, C.; Raza, A.; Song, R.; Zhang, T.-J.; Pehkonen, S. O.; Liang, B. Nanostructured TiO2/CuO Dual-Coated Copper Meshes with Superhydrophilic,

Underwater Superoleophobic and Self-Cleaning Properties for Highly Efficient Oil/Water Separation. *Chem. Eng. J.* **2017**, *328*, 497–510. https://doi.org/10.1016/j.cej.2017.07.075.

(26) Li, Y.; Ishigaki, T. Thermodynamic Analysis of Nucleation of Anatase and Rutile from TiO2 Melt. *J. Cryst. Growth* **2002**, *242* (3–4), 511–516. https://doi.org/10.1016/S0022-0248(02)01438-0.

(27) Gupta, R. K.; Dunderdale, G. J.; England, M. W.; Hozumi, A. Oil/Water Separation Techniques: A Review of Recent Progresses and Future Directions. *J. Mater. Chem. A* **2017**, *5* (31), 16025–16058.

(28) Sun, F.; Li, T.-T.; Zhang, X.; Shiu, B.-C.; Zhang, Y.; Ren, H.-T.; Peng, H.-K.; Lin, J.-H.; Lou, C.-W. Facile Fabrication of Hydrophilic-Underwater Superoleophobic Poly(N-Isopropylacrylamide) Coated PP/LPET Nonwoven Fabrics for Highly Efficient Oil/Water Separation. *Prog. Org. Coat.* **2020**, *148*, 105780. https://doi.org/10.1016/j.porgcoat.2020.105780.

(29) Ragesh, P.; Anand Ganesh, V.; Nair, S. V.; Nair, A. S. A Review on 'Self-Cleaning and Multifunctional Materials.' *J Mater Chem A* **2014**, *2* (36), 14773–14797. https://doi.org/10.1039/C4TA02542C.

(30) Ali, N.; Bilal, M.; Khan, A.; Ali, F.; Iqbal, H. M. N. Design, Engineering and Analytical Perspectives of Membrane Materials with Smart Surfaces for Efficient Oil/Water Separation. *TrAC Trends Anal. Chem.* **2020**, *127*, 115902. https://doi.org/10.1016/j.trac.2020.115902.

(31) Butt, H.-J.; Graf, K.; Kappl, M. *Physics and Chemistry of Interfaces*; Die Deutsche Bibliothek, 2003; Vol. 1.

(32) *Surface and Colloid Science: Volume 11: Experimental Methods*; Good, R. J., Stromberg, R. R., Eds.; Springer US: Boston, MA, 1979. https://doi.org/10.1007/978-1-4615-7969-4.

(33) Rosario, R.; Gust, D.; Garcia, A. A.; Hayes, M.; Taraci, J. L.; Clement, T.; Dailey, J. W.; Picraux, S. T. Lotus Effect Amplifies Light-Induced Contact Angle Switching. *J. Phys. Chem. B* **2004**, *108* (34), 12640–12642.

(34) Bhushan, B. *Bioinspired Water Harvesting, Purification, and Oil-Water Separation*; Springer Series in Materials Science; Springer International Publishing: Cham, 2020; Vol. 299. https://doi.org/10.1007/978-3-030-42132-8.

(35) Marmur, A. Soft Contact: Measurement and Interpretation of Contact Angles. *Soft Matter* **2006**, *2* (1), 12–17.

(36) Marmur, A.; Della Volpe, C.; Siboni, S.; Amirfazli, A.; Drelich, J. W. Contact Angles and Wettability: Towards Common and Accurate Terminology. *Surf. Innov.* **2017**, *5* (1), 3–8.

(37) Ahmad, D.; van den Boogaert, I.; Miller, J.; Presswell, R.; Jouhara, H. Hydrophilic and Hydrophobic Materials and Their Applications. *Energy Sources Part Recovery Util. Environ. Eff.* **2018**, *40* (22), 2686–2725. https://doi.org/10.1080/15567036.2018.1511642.

(38) Faghri, A.; Zhang, Y. *Transport Phenomena in Multiphase Systems*; Elsevier Academic Press: Burlington, Mass, 2006.

(39) Kanduč, M.; Schlaich, A.; Schneck, E.; Netz, R. R. Water-Mediated Interactions between Hydrophilic and Hydrophobic Surfaces. *Langmuir* **2016**, *32* (35), 8767–8782. https://doi.org/10.1021/acs.langmuir.6b01727.

(40) Monroe, J.; Barry, M.; DeStefano, A.; Aydogan Gokturk, P.; Jiao, S.; Robinson-Brown, D.; Webber, T.; Crumlin, E. J.; Han, S.; Shell, M. S. Water Structure and Properties at Hydrophilic and Hydrophobic Surfaces. *Annu. Rev. Chem. Biomol. Eng.* **2020**, *11* (1), 523–557. https://doi.org/10.1146/annurev-chembioeng-120919-114657.

(41) Wang, Y.; Gong, X. Special Oleophobic and Hydrophilic Surfaces: Approaches, Mechanisms, and Applications. *J. Mater. Chem. A* **2017**, *5* (8), 3759–3773. https://doi.org/10.1039/C6TA10474F.

(42) Cassie, A. B. D. Contact Angles. *Discuss. Faraday Soc.* **1948**, *3*, 11–16.

(43) Milne, A. J. B.; Amirfazli, A. The Cassie Equation: How It Is Meant to Be Used. *Adv. Colloid Interface Sci.* **2012**, *170* (1–2), 48–55. https://doi.org/10.1016/j.cis.2011.12.001.

(44) Zhu, M.; Liu, Y.; Chen, M.; Xu, Z.; Li, L.; Zhou, Y. Metal Mesh-Based Special Wettability Materials for Oil-Water Separation: A Review of the Recent Development. *J. Pet. Sci. Eng.* **2021**, *205*, 108889. https://doi.org/10.1016/j.petrol.2021.108889.

(45) Liu, K.; Tian, Y.; Jiang, L. Bio-Inspired Superoleophobic and Smart Materials: Design, Fabrication, and Application. *Prog. Mater. Sci.* **2013**, *58* (4), 503–564. https://doi.org/10.1016/j.pmatsci.2012.11.001.

(46) Milionis, A.; Bayer, I. S.; Loth, E. Recent Advances in Oil-Repellent Surfaces. *Int. Mater. Rev.* **2016**, *61* (2), 101–126. https://doi.org/10.1080/09506608.2015.1116492.

(47) Vinogradova, O. I. Slippage of Water over Hydrophobic Surfaces. *Int. J. Miner. Process.* **1999**, *56* (1–4), 31–60. https://doi.org/10.1016/S0301-7516(98)00041-6.

(48) Drelich, J. W.; Boinovich, L.; Chibowski, E.; Della Volpe, C.; Hołysz, L.; Marmur, A.; Siboni, S. Contact Angles: History of over 200 Years of Open Questions. *Surf. Innov.* **2019**, *8* (1–2), 3–27.

(49) Drelich, J.; Chibowski, E.; Meng, D. D.; Terpilowski, K. Hydrophilic and Superhydrophilic Surfaces and Materials. *Soft Matter* **2011**, *7* (21), 9804. https://doi.org/10.1039/c1sm05849e.

(50) Zhang, S.; Wu, L.; Deng, F.; Zhao, D.; Zhang, C.; Zhang, C. Hydrophilic Modification of PVDF Porous Membrane via a Simple Dip-Coating Method in Plant Tannin Solution. *RSC Adv.* **2016**, *6* (75), 71287–71294. https://doi.org/10.1039/C6RA13634F.

(51) Li, J.; Yan, L.; Hu, W.; Li, D.; Zha, F.; Lei, Z. Facile Fabrication of Underwater Superoleophobic TiO 2 Coated Mesh for Highly Efficient Oil/Water Separation. *Colloids Surf. Physicochem. Eng. Asp.* **2016**, *489*, 441–446. https://doi.org/10.1016/j.colsurfa.2015.11.008.

(52) Zhu, J.; Zhang, Y.; Tian, M.; Liu, J. Fabrication of a Mixed Matrix Membrane with in Situ Synthesized Quaternized Polyethylenimine Nanoparticles for Dye Purification and Reuse. **2015**, 12.

(53) You, Q.; Ran, G.; Wang, C.; Zhao, Y.; Song, Q. A Novel Superhydrophilic–Underwater Superoleophobic Zn-ZnO Electrodeposited Copper Mesh for Efficient Oil/Water Separation. *Sep. Purif. Technol.* **2018**, *193*, 21–28. https://doi.org/10.1016/j.seppur.2017.10.055.

(54) Jiang, T. Biomimetic Superoleophobic Surfaces: Focusing on Their Fabrication and Applications. *J Mater Chem A* **2014**, 17.

(55) Otitoju, T. A.; Ahmad, A. L.; Ooi, B. S. Superhydrophilic (Superwetting) Surfaces: A Review on Fabrication and Application. *J. Ind. Eng. Chem.* **2017**, *47*, 19–40. https://doi.org/10.1016/j.jiec.2016.12.016.

(56) Lai, Y.; Lin, C.; Wang, H.; Huang, J.; Zhuang, H.; Sun, L. Superhydrophilic–Superhydrophobic Micropattern on TiO2 Nanotube Films by Photocatalytic Lithography. *Electrochem. Commun.* **2008**, *10* (3), 387–391. https://doi.org/10.1016/j.elecom.2007.12.020.

(57) Yong, J.; Yang, Q.; Guo, C.; Chen, F.; Hou, X. A Review of Femtosecond Laser-Structured Superhydrophobic or Underwater Superoleophobic Porous Surfaces/Materials for Efficient Oil/Water Separation. *RSC Adv.* **2019**, *9* (22), 12470–12495. https://doi.org/10.1039/C8RA10673H.

(58) Zupančič, M.; Steinbücher, M.; Gregorčič, P.; Golobič, I. Enhanced Pool-Boiling Heat Transfer on Laser-Made Hydrophobic/Superhydrophilic Polydimethylsiloxane-Silica Patterned Surfaces. *Appl. Therm. Eng.* **2015**, *91*, 288–297. https://doi.org/10.1016/j.applthermaleng.2015.08.026.

(59) Wolansky, G.; Marmur, A. Apparent Contact Angles on Rough Surfaces: The Wenzel Equation Revisited. *Colloids Surf. Physicochem. Eng. Asp.* **1999**, *156* (1–3), 381–388. https://doi.org/10.1016/S0927-7757(99)00098-9.

(60) Neumann, A. W.; Good, R. J. Techniques of Measuring Contact Angles. In *Surface and colloid science*; Springer, 1979; pp 31–91.

(61) Drelich, J. Guidelines to Measurements of Reproducible Contact Angles Using a Sessile-Drop Technique. *Surf. Innov.* **2013**, *1* (4), 248–254. https://doi.org/10.1680/si.13.00010.

(62) Drelich, J.; Marmur, A. Physics and Applications of Superhydrophobic and Superhydrophilic Surfaces and Coatings. *Surf. Innov.* **2014**, *2* (4), 211–227. https://doi.org/10.1680/si.13.00017.

(63) Butt, H.-J.; Graf, K.; Kappl, M. Physics and Chemistry of Interfaces. 30.

(64) Eick, J. D.; Good, R. J.; Neumann, A. W. Thermodynamics of Contact Angles. II. Rough Solid Surfaces. *J. Colloid Interface Sci.* **1975**, *53* (2), 235–248. https://doi.org/10.1016/0021-9797(75)90010-7.

(65) Seo, K.; Kim, M.; Kim, D. H. Re-Derivation of Young's Equation, Wenzel Equation, and Cassie-Baxter Equation Based on Energy Minimization. In *Surface Energy*; Aliofkhazraei, M., Ed.; InTech, 2015. https://doi.org/10.5772/61066.

(66) Drelich, J.; Chibowski, E.; Meng, D. D.; Terpilowski, K. Hydrophilic and Superhydrophilic Surfaces and Materials. *Soft Matter* **2011**, *7* (21), 9804. https://doi.org/10.1039/c1sm05849e.

(67) Drelich, J. W. Contact Angles: From Past Mistakes to New Developments through Liquid-Solid Adhesion Measurements. *Adv. Colloid Interface Sci.* **2019**, *267*, 1–14.

(68) Pierce, E.; Carmona, F. J.; Amirfazli, A. Understanding of Sliding and Contact Angle Results in Tilted Plate Experiments. *Colloids Surf. Physicochem. Eng. Asp.* **2008**, *323* (1–3), 73–82.

(69) Gao, L.; McCarthy, T. J. Contact Angle Hysteresis Explained. *Langmuir* **2006**, *22* (14), 6234–6237.

(70) Drelich, J. W.; Boinovich, L.; Chibowski, E.; Della Volpe, C.; Hołysz, L.; Marmur, A.; Siboni, S. Contact Angles: History of over 200 Years of Open Questions. *Surf. Innov.* **2019**, *8* (1–2), 3–27.

(71) Zhou, W.; Apkarian, R.; Wang, Z. L.; Joy, D. Fundamentals of Scanning Electron Microscopy (SEM). In *Scanning microscopy for nanotechnology*; Springer, 2006; pp 1–40.

(72) Mohammed, A.; Abdullah, A. Scanning Electron Microscopy (SEM): A Review. In *Proceedings of the 2018 International Conference on Hydraulics and Pneumatics—HERVEX, Băile Govora, Romania*; 2018; pp 7–9.

(73) Orsini, F.; Du Pasquier, A.; Beaudoin, B.; Tarascon, J. M.; Trentin, M.; Langenhuizen, N.; De Beer, E.; Notten, P. In Situ Scanning Electron Microscopy (SEM) Observation of Interfaces within Plastic Lithium Batteries. *J. Power Sources* **1998**, *76* (1), 19–29.

(74) Statham, P. J. Measuring Performance of Energy-Dispersive X-Ray Systems. *Microsc. Microanal.* **1998**, *4* (6), 605–615. https://doi.org/10.1017/S1431927698980588.

(75) Abd Mutalib, M.; Rahman, M. A.; Othman, M. H. D.; Ismail, A. F.; Jaafar, J. Scanning Electron Microscopy (SEM) and Energy-Dispersive X-Ray (EDX) Spectroscopy. In *Membrane Characterization*; Elsevier, 2017; pp 161–179. https://doi.org/10.1016/B978-0-444-63776-5.00009-7.

(76) Schreiner, M.; Melcher, M.; Uhlir, K. Scanning Electron Microscopy and Energy Dispersive Analysis: Applications in the Field of Cultural Heritage. *Anal. Bioanal. Chem.* **2007**, *387* (3), 737–747. https://doi.org/10.1007/s00216-006-0718-5.

(77) Guerrero-Pérez, M. O.; Patience, G. S. Experimental Methods in Chemical Engineering: Fourier Transform Infrared Spectroscopy—FTIR. *Can. J. Chem. Eng.* **2020**, *98* (1), 25–33. https://doi.org/10.1002/cjce.23664.

(78) Chen, Y.; Zou, C.; Mastalerz, M.; Hu, S.; Gasaway, C.; Tao, X. Applications of Micro-Fourier Transform Infrared Spectroscopy (FTIR) in the Geological Sciences—A Review. *Int. J. Mol. Sci.* **2015**, *16* (12), 30223–30250. https://doi.org/10.3390/ijms161226227.

(79) Winey, M.; Meehl, J. B.; O'Toole, E. T.; Giddings, T. H. Conventional Transmission Electron Microscopy. *Mol. Biol. Cell* **2014**, *25* (3), 319–323. https://doi.org/10.1091/mbc.e12-12-0863.

(80) Lin, Y.; Zhou, M.; Tai, X.; Li, H.; Han, X.; Yu, J. Analytical Transmission Electron Microscopy for Emerging Advanced Materials. *Matter* **2021**, *4* (7), 2309–2339. https://doi.org/10.1016/j.matt.2021.05.005.

(81) Browning, N. D.; Bonds, M. A.; Campbell, G. H.; Evans, J. E.; LaGrange, T.; Jungjohann, K. L.; Masiel, D. J.; McKeown, J.; Mehraeen, S.; Reed, B. W.; Santala, M. Recent Developments in Dynamic Transmission Electron Microscopy. *Curr. Opin. Solid State Mater. Sci.* **2012**, *16* (1), 23–30. https://doi.org/10.1016/j.cossms.2011.07.001.

(82) Franken, L. E.; Boekema, E. J.; Stuart, M. C. A. Transmission Electron Microscopy as a Tool for the Characterization of Soft Materials: Application and Interpretation. *Adv. Sci.* **2017**, *4* (5), 1600476. https://doi.org/10.1002/advs.201600476.

(83) Talmon, Y. Transmission Electron Microscopy of Complex Fluids: The State of the Art. *Berichte Bunsenges. Für Phys. Chem.* **1996**, *100* (3), 364–372. https://doi.org/10.1002/bbpc.19961000322.

(84) Skakle, J. Applications of X-Ray Powder Diffraction in Materials Chemistry. *Chem. Rec.* **2005**, *5* (5), 252–262. https://doi.org/10.1002/tcr.20050.

(85) Khan, H.; Yerramilli, A. S.; D'Oliveira, A.; Alford, T. L.; Boffito, D. C.; Patience, G. S. Experimental Methods in Chemical Engineering: X-ray Diffraction Spectroscopy— XRD. *Can. J. Chem. Eng.* **2020**, *98* (6), 1255–1266. https://doi.org/10.1002/cjce.23747.

(86) Chauhan, A. Powder XRD Technique and Its Applications in Science and Technology. *J. Anal. Bioanal. Tech.* **2014**, *5* (6). https://doi.org/10.4172/2155-9872.1000212.

(87) Thamaphat, K.; Limsuwan, P.; Ngotawornchai, B. Phase Characterization of TiO2 Powder by XRD and TEM. 5.

(88) Yu, J.; Zhao, X.; Zhao, Q.; Wang, G. Preparation and Characterization of Super-Hydrophilic Porous TiO2 Coating Films. *Mater. Chem. Phys.* **2001**, *68* (1–3), 253–259. https://doi.org/10.1016/S0254-0584(00)00364-3.

(89) Andrade, J. D. X-Ray Photoelectron Spectroscopy (XPS). 91.

(90) Aziz, M.; Ismail, A. F. X-Ray Photoelectron Spectroscopy (XPS). In *Membrane Characterization*; Elsevier, 2017; pp 81–93. https://doi.org/10.1016/B978-0-444-63776-5.00005-X.

(91) Korin, E.; Froumin, N.; Cohen, S. Surface Analysis of Nanocomplexes by X-Ray Photoelectron Spectroscopy (XPS). *ACS Biomater. Sci. Eng.* **2017**, *3* (6), 882–889. https://doi.org/10.1021/acsbiomaterials.7b00040.

(92) Venezia, A. M. X-Ray Photoelectron Spectroscopy (XPS) for Catalysts Characterization. *Catal. Today* **2003**, *77* (4), 359–370. https://doi.org/10.1016/S0920-5861(02)00380-2.

(93) Jolm F. Moulder; William F. Stickle; Peter E.'Sobol; Kennetlf D. Bomben. *Handbook of X-Ray Photoelectron Spectroscopy*; Perkin-Elmer Corporation Physical Electronics Division 6509 Flying Cloud Drive Eden Prairie, MinnCSOla 55344 United Stales of America, 1992.

(94) Vitos, L.; Ruban, A. V.; Skriver, H. L.; Kollár, J. The Surface Energy of Metals. *Surf. Sci.* **1998**, *411* (1–2), 186–202. https://doi.org/10.1016/S0039-6028(98)00363-X.

(95) Good, R. J.; Girifalco, L. A. A THEORY FOR ESTIMATION OF SURFACE AND INTERFACIAL ENERGIES. III. ESTIMATION OF SURFACE ENERGIES OF SOLIDS FROM CONTACT ANGLE DATA. *J. Phys. Chem.* **1960**, *64* (5), 561–565. https://doi.org/10.1021/j100834a012.

(96) Janssen, D.; De Palma, R.; Verlaak, S.; Heremans, P.; Dehaen, W. Static Solvent Contact Angle Measurements, Surface Free Energy and Wettability Determination of Various Self-Assembled Monolayers on Silicon Dioxide. *Thin Solid Films* **2006**, *515* (4), 1433–1438. https://doi.org/10.1016/j.tsf.2006.04.006.

(97) Cappelletti, G.; Ardizzone, S.; Meroni, D.; Soliveri, G.; Ceotto, M.; Biaggi, C.; Benaglia, M.; Raimondi, L. Wettability of Bare and Fluorinated Silanes: A Combined Approach Based on Surface Free Energy Evaluations and Dipole Moment Calculations. *J. Colloid Interface Sci.* **2013**, *389* (1), 284–291. https://doi.org/10.1016/j.jcis.2012.09.008.

(98) Kozbial, A.; Li, Z.; Conaway, C.; McGinley, R.; Dhingra, S.; Vahdat, V.; Zhou, F.; D'Urso, B.; Liu, H.; Li, L. Study on the Surface Energy of Graphene by Contact Angle Measurements. *Langmuir* **2014**, *30* (28), 8598–8606. https://doi.org/10.1021/la5018328.

(99) Shervani, S.; Ling, J.; Liu, J.; Husain, T. Self-Cleaning Nanoscale Coating for the Separation of Oil–Water Mixture. *Coatings* **2019**, *9* (12), 860.

(100) Annamalai, M.; Gopinadhan, K.; Han, S. A.; Saha, S.; Park, H. J.; Cho, E. B.; Kumar, B.; Patra, A.; Kim, S.-W.; Venkatesan, T. Surface Energy and Wettability of van Der Waals Structures. *Nanoscale* **2016**, *8* (10), 5764–5770. https://doi.org/10.1039/C5NR06705G.

(101) Chen, C.; Chen, L.; Chen, S.; Yu, Y.; Weng, D.; Mahmood, A.; Wang, G.; Wang, J. Preparation of Underwater Superoleophobic Membranes via TiO2 Electrostatic Self-Assembly for Separation of Stratified Oil/Water Mixtures and Emulsions. *J. Membr. Sci.* **2020**, *602*, 117976. https://doi.org/10.1016/j.memsci.2020.117976.

(102) Rasouli, S.; Rezaei, N.; Hamedi, H.; Zendehboudi, S.; Duan, X. Design, Fabrication, and Characterization of a Facile Superhydrophobic and Superoleophilic Mesh-Based Membrane for Selective Oil-Water Separation. *Chem. Eng. Sci.* **2021**, *236*, 116354.

(103) Gong, Z.; Yang, N.; Chen, Z.; Jiang, B.; Sun, Y.; Yang, X.; Zhang, L. Fabrication of Meshes with Inverse Wettability Based on the TiO2 Nanowires for Continuous Oil/Water Separation. *Chem. Eng. J.* **2020**, *380*, 122524. https://doi.org/10.1016/j.cej.2019.122524.

(104) Liu, Y.; Zhang, K.; Yao, W.; Zhang, C.; Han, Z.; Ren, L. A Facile Electrodeposition Process for the Fabrication of Superhydrophobic and Superoleophilic Copper Mesh for Efficient Oil–Water Separation. *Ind. Eng. Chem. Res.* **2016**, *55* (10), 2704–2712. https://doi.org/10.1021/acs.iecr.5b03503.

(105) Liu, P.; Cao, L.; Zhao, W.; Xia, Y.; Huang, W.; Li, Z. Insights into the Superhydrophobicity of Metallic Surfaces Prepared by Electrodeposition Involving

Spontaneous Adsorption of Airborne Hydrocarbons. *Appl. Surf. Sci.* **2015**, *324*, 576–583. https://doi.org/10.1016/j.apsusc.2014.10.170.

(106) Chen, D.; Kang, Z.; Li, W. One-Step Electrodeposition to Fabricate Superhydrophobic Coating and Its Reversible Wettability Transformation. *Mater. Res. Express* **2020**, *7* (1), 016404. https://doi.org/10.1088/2053-1591/ab5bf3.

(107) Fox, K. E.; Tran, N. L.; Nguyen, T. A.; Nguyen, T. T.; Tran, P. A. Surface Modification of Medical Devices at Nanoscale—Recent Development and Translational Perspectives. In *Biomaterials in Translational Medicine*; Elsevier, 2019; pp 163–189. https://doi.org/10.1016/B978-0-12-813477-1.00008-6.

(108) Karuppuchamy, S.; Jeong, J. M. Super-Hydrophilic Amorphous Titanium Dioxide Thin Film Deposited by Cathodic Electrodeposition. *Mater. Chem. Phys.* **2005**, *93* (2–3), 251–254. https://doi.org/10.1016/j.matchemphys.2005.04.015.

(109) Boccaccini, A. R.; Karapappas, P.; Marijuan, J. M.; Kaya, C. TiO $_2$ Coatings on Silicon Carbide and Carbon Fibre Substrates by Electrophoretic Deposition. *J. Mater. Sci.* **2004**, *39* (3), 851–859. https://doi.org/10.1023/B:JMSC.0000012914.47793.3e.

(110) Tanner, B. K. BASIC DYNAMICAL X-RAY DIFFRACTION THEORY. In *X-ray Diffraction Topography*; Elsevier, 1976; pp 1–23. https://doi.org/10.1016/B978-0-08-019692-3.50008-7.

(111) Holder, E. Laboratory-Scale Testing of Dispersant Effectiveness of 20 Oils Using the Baffled Flask Test. 10.

(112) Zhang, J.; Fang, W.; Zhang, F.; Gao, S.; Guo, Y.; Li, J.; Zhu, Y.; Zhang, Y.; Jin, J. Ultrathin Microporous Membrane with High Oil Intrusion Pressure for Effective Oil/Water Separation. *J. Membr. Sci.* **2020**, *608*, 118201. https://doi.org/10.1016/j.memsci.2020.118201.

(113) Li, J.; Kang, R.; Zhang, Y.; Li, M.; She, H.; Zha, F.; Lei, Z. Facile Fabrication of Superhydrophobic Meshes with Different Water Adhesion and Their Influence on Oil/Water Separation. *RSC Adv.* **2016**, *6* (93), 90824–90830. https://doi.org/10.1039/C6RA17153B.

(114) Annamalai, M.; Gopinadhan, K.; Han, S. A.; Saha, S.; Park, H. J.; Cho, E. B.; Kumar, B.; Patra, A.; Kim, S.-W.; Venkatesan, T. Surface Energy and Wettability of van Der Waals Structures. *Nanoscale* **2016**, *8* (10), 5764–5770. https://doi.org/10.1039/C5NR06705G.

(115) *Polar and Dispersive Components of Solid Surface Tensions*. https://www.jikangroup.com/2021/10/17/polar-and-dispersive-solid-surface-tensions/.

(116) Inkson, B. J. Scanning Electron Microscopy (SEM) and Transmission Electron Microscopy (TEM) for Materials Characterization. In *Materials characterization using nondestructive evaluation (NDE) methods*; Elsevier, 2016; pp 17–43.